Imperial College
London

Royal School of Mines

Department of Earth Science and Engineering

Faculty of Engineering

# Mechanical Wellbore Stability in Anisotropic Rock Formations

---

I Gusti Ngurah Beni SETIAWAN

*Supervisor*: Professor Robert W. ZIMMERMAN

*A thesis submitted in fulfilment of the requirements*

*for the degree of Doctor of Philosophy of Imperial College London*

London 2020

*to Rayner, Reiki and Tania.*

*And, my lovely parents I Gusti Ngurah Sandjaja & I Gusti Ayu Warniti*

*It is the time you have wasted for your rose that makes your rose so important.*

—Antoine de Saint-Exupéry, *The Little Prince*.

# Declaration of Originality

I hereby declare that this thesis, entitled “Mechanical Wellbore Stability in Anisotropic Rock Formations”, is entirely my own work. All materials created by others that are used in the thesis have been given full acknowledgement.

I Gusti Ngurah Beni Setiawan

# Copyright Declaration

# *Abstract*

## Mechanical Wellbore Stability in Anisotropic Rock Formations

I Gusti Ngurah Beni Setiawan, Department of Earth Science and Engineering
Imperial College London

Wellbore instability in petroleum operations remains a major concern among operators, due to its significant safety-related issues and economic consequences. This thesis investigates issues related to the mechanical stability of drilling through the types of anisotropic rocks that are commonly encountered in petroleum operations. The contribution of this thesis is two-fold: (1) to present a unified approach through which the influence of the elastic and strength anisotropy on wellbore stability can be thoroughly examined, and (2) to propose a new unified semi-analytical solution based on graphical conformal mapping and complex potential methods to compute the in-plane stress around an arbitrarily-shaped hole in isotropic or anisotropic materials.

A unified approach to investigate the influence of the elastic and strength anisotropy on wellbore stability has been developed, that utilises the Lekhnitskii-Amadei anisotropic elasticity formalism to compute the stresses around an arbitrarily-oriented circular borehole. Failure is modelled by coupling the Jaeger plane of weakness model to the fully-triaxial Mogi-Coulomb failure criterion. The model is used to study the safe drilling mud pressure window, and considerable differences are found between the predictions of the new model, and predictions that ignore elastic anisotropy when calculating the stresses. The results underscore the importance of fully accounting for rock anisotropy and fully-triaxial failure criteria when doing wellbore stability analysis.

A new semi-analytical approach has been proposed to study the stresses around non-circular holes in isotropic or anisotropic materials. The method requires only the outline coordinates of the hole, the elastic moduli of the material, and the magnitudes and directions of the far-field stresses. The proposed method has been applied for two purposes. Firstly, to model episodic borehole breakout development to track the stress evolution around the breakout, and to investigate the possibility of estimating the *in situ* stress state based on observations of breakout geometry. The method has also been used to compute the near-wellbore stress around a damaged wellbore whose geometry is obtained from ultrasonic data.

# Acknowledgement

Completing a PhD is a unique experience of a lifetime. The work produced in this document is a reflection of 15 years of learning, including my extensive ten years with Schlumberger—a "community" where I started my professional career. I would not have been able to complete this journey without the support of a range of sources. I would like to thank Professor Robert W. Zimmerman for having faith in me and for being a great teacher. His generosity, understanding and patience have been invaluable for me and my family. I am immensely fortunate to have been supervised by Robert whose knowledge and open-mindedness have taken me to another level of understanding. It was not easy for our family adapting to a so-called 'PhD journey', but Robert always reminds me to put family as my priority. Thank you.

I thank the Earth Science and Engineering Department at Imperial College London for the support especially during the unprecedented time of coronavirus pandemic that has forced almost everyone to embrace a 'new normal'. The support from the department has been so enormous that I can set up my home-based office to carry on my research with ease. I also thank the Indonesian Endowment Fund for Education (LPDP) of the Republic of Indonesia for supporting this research.

I'd like to thank my friend Dr. Fernando Sitorus, Dr. Harya Nugraha, Dr. Adhipa Herlambang, Qi Adlan and Aurio Erdi. Thank you for the friendship that has enriched this unique experience in London. And also, my former teachers at Institute Technology Bandung (ITB), Professor Sri Widiyantoro, Professor Tutuka Ariadji, Dr. Sonny Winardhi, whose support has never faded away ever since I graduated from ITB more than a decade ago.

I am so grateful to have had the opportunity to closely work with Dr. Tan Chee Phuat (currently with PETRONAS Research Group) and Somessh Bahuguna, from whom I learned about geomechanics through intensive discussion, interaction and, sometimes, debate and argumentation, during my time with Schlumberger. My technical experience and professional character have been shaped and polished by intensive interactions with them. Not only that I learned about geomechanics, but to become a consultant that always put integrity, commitment and technical excellence, as a priority.

I also thank the geomechanics team of Schlumberger Gatwick and Abingdon Technology Center: Saad Kisra, Adrian Rodriguez-Herrera, Dr. Juliane Heiland, Dr. Assef Hussein and Dr.

Kwang-Ho Lee, for their interest in my research and the discussion. Their feedbacks have helped me aligning this research with the industry challenges. I am grateful to have contacted Dr Jasmine Ambrose (ICL PhD & former Schlumberger Malaysia) in 2016 who convinced me to approach Professor Robert Zimmerman and to conduct my doctoral research at Imperial College. And, I'd like to thank Sonny Wiyoga of Schlumberger Jakarta who helped me with the ultrasonic data that has expanded the potential applicability of the semi-analytical method proposed in this research.

I want to dedicate this work for the late (*Alm.*) Leo Anis, my former manager at Schlumberger. Without him, I would never have had a chance to grow so rapidly in Schlumberger. During his life, Leo was an open-minded manager, a strong leader, a great supporter and, most importantly, a good friend. Leo is an example of a classic solid geoscientist that I have ever known.

I am so fortunate to have known Ahmad Yuniarto (AY), a brilliant lifelong learner and a strong T-shaped person from whom I learn a lot about reframing our life. Our friendship started long ago in a rather 'unique and repetitive' way but turned out to be so inspiring. Thank you for the trust and the generosity that I have always felt every time I share my story to you. I can only hope to repay this by doing the same to other people.

And, I could not forget how crucial is Yoga Prawita's family for us in the first thirty days since we landed in London. Yoga, Wulan, Kaiva and Valkya, thank you for being so warm-hearted and kind to our family. Our journey in London was started at 6 Cecile Avenue—a warm place where all doubts turned into optimism. And also for all the Havering family: Mas Ery's family, Mas Arfan's family, Mas Kollin's family, Mas Bayu's family and Mas Rasyid's family.

To my lovely parents and teachers: I Gusti Ngurah Sandjaja and I Gusti Ayu Warniti, for allowing me to pursue my dream(s). I realise that I have stolen so much of our family time, but thank you for your unconditional love and endless support. I also dedicate this work to (*Alm.*) I Gusti Made Santosa—an uncle, the glue in the family, a solid engineer and an inspiration. For *Tunini* for her persistence since I was still a fifth-grader, to keep reminding me to become an engineer just like my uncle, and I Gusti Ngurah Santika from whom I learned about dedication. Also, I am so grateful to have I Nyoman Supriyatna, Ni Made Widiari and Made Ian Maheswara for always bringing a new atmosphere in our family.

I must thank those closest to my heart. Tania Sari. For your understanding, patience and endless support. I don't know where the next destination will be, but I assure you it will be much better than before. Thank you for teaching me that life requires teamwork. And, to our future scientists and heroes: I Gusti Ngurah Rayner Bhisma Setiawan and I Gusti Ngurah Reiki Airlangga Setiawan. This work is a symbol of someone's dream and perseverance and epitomises the many sacrifices that your mother has given to always supporting me. You should *not* read what is written, but the unwritten. You must achieve something more than whatever we have (and will) achieved. Thank you for being such a good teacher in so many ways in my life. If I can do it, then you can do it too—even better. •

# List of publications

The work presented in this thesis has been published in the following scientific journals and presented at several international conferences. These are:

- Setiawan, N. B. and Zimmerman, R. W., A unified methodology for computing the stresses around an arbitrarily-shaped hole in isotropic or anisotropic materials, *International Journal of Solids and Structures*, 2020, 199, 131-143.
- Setiawan, N. B., Mechanical Wellbore Stability in Overpressured Shales, Book chapter in Memoir ISPG: Overpressured Sedimentary Basin, Petroleum Geology & Hazards, the *Indonesian Society of Petroleum Geologist*, 2020.
- Setiawan, N. B. and Zimmerman, R. W., Wellbore breakout prediction in transversely isotropic rocks using true-triaxial failure criteria. *International Journal of Rock Mechanics and Mining Sciences*, 2018, 112, 313-322.
- Setiawan, N. B. and Zimmerman, R. W., Semi-analytical Method for Tracking the Evolution of Borehole Breakouts, *54th U.S. Rock Mechanics Symposium*, 2020, Golden, Colorado, USA.
- Setiawan, N. B. and Zimmerman, R. W., Semi-analytical Method for Tracking the Evolution of Borehole Breakouts, *Engineering Mechanics Institute Conference*, 2019, California Institute of Technology, USA.

- Setiawan, N. B. and Zimmerman, R. W., The Implications of using Anisotropic Elasticity and Fully-Triaxial Failure Criteria for Borehole Stability Analysis in Shales, *53rd U.S. Rock Mechanics Symposium*, 2019, New York, USA.
- Setiawan, N. B. and Zimmerman, R. W., Drilling Risk Identification through Anisotropic Geomechanical Modelling, *International Conference on Oil & Gas Engineering and Technology (ICOGET)*, 2018, Kuala Lumpur, Malaysia.
- Zimmerman, R.W., Ambrose, J., and Setiawan, N.B., Failure of Anisotropic Rocks such as Shales, and Implications for Borehole Stability, $10^{th}$ Asian Rock Mechanics Symposium, The *ISRM International Symposium*, 2018, Singapore.

The following publications are in preparation for journal submission:

- Setiawan, N. B. and Zimmerman, R. W., A semi-analytical method for modelling wellbore breakout development.
- Setiawan, N. B., Zimmerman, R. W., and Wiyoga, S. A., The near-wellbore stress profiling using downhole ultrasonic borehole imager.

# Contents

# List of Figures

# List of Tables

# Chapter 1 Introduction

## 1.1. Wellbore stability analysis to minimise drilling non-productive time

The success of hydrocarbon extraction in the last two decades is partially attributed to the successful implementation of directional drilling technology. The primary objective of a directional wellbore is to achieve greater exposure to the reservoir rocks, targeting sweet spots that are unreachable with vertical wellbores, or to produce hydrocarbon located at a considerable distance from the main offshore platform utilising *extended reach drilling* (ERD) technology. These advances have also allowed the utilisation of a single drilling pad for several deviated wellbores to reach oil pockets in the subsurface which, in the case of offshore drilling, can significantly reduce operational costs. In other situations, deviated wellbores are needed in well-control operation to intersect the problematic wellbore from a safe distance, to provide sufficient hydrostatic pressure by pumping high-density fluid into the annulus. However, drilling inclined wellbores poses a greater risk associated with the instability of the wellbore, as compared to drilling vertical wells.

Wellbore instability can cause a significant amount of operational expenditure to operators. It has been estimated that at least 10% of wellbore budgets were spent to deal with unplanned operations due to wellbore instability. This estimate may reach around one billion dollars annually (Aadnoy & Ong, 2003). An analysis from the Gulf of Mexico also shows that more than 31% and 41% of *non–productive time* (NPT) is related to wellbore stability in non-subsalt and subsalt wells, respectively (Hoyer, 2009). In a wellbore of 20,000 ft measured depth, these statistics are equivalent to about USD 2.6 million to USD 7.66 million worth of investment (Gala *et al*., 2010). In shale rocks, the lost-time and trouble costs for drilling had been estimated to be approximately USD 500 million annually (Van Oort *et al*., 1996). Thus, the demand for conducting fit-for-purpose geomechanical modelling has been increasing in recent decades. This mainly stems from the fact that oil operators must deal with even more complex and challenging drilling environments such as complex geological settings, tectonically active areas, much deeper reservoir targets, high pressure-high temperature formations, fractured rocks and a more sophisticated wellbore design. Therefore, one of the goals for many operators in drilling optimisation is to minimise the NPT related to wellbore instability by constructing a robust model to mitigate the potential problems.

The role of geomechanics in minimising excessive drilling costs has been acknowledged by many researchers. Several authors, such as Caicedo *et al*. (2010), Hamid *et al*. (2016), Moazzeni *et al*. (2010), Naidu *et al*. (2016), Ong *et al*. (2015), Xi *et al*. (2015), Zadvornov *et al*. (2016), reported the benefit of having a pre-drilling geomechanical model. Their respective drilling challenges have been addressed by means of, but not limited to, the construction of a robust stress profile, the estimation of the rock elastic and strength properties, drilling trajectory evaluation, drilling fluid properties optimization, and casing seat design. For instance, Hamid *et al*. (2016) used a geomechanical approach to aid their horizontal well drilling and hydraulic fracturing in a tight carbonate reservoir. They reported that the NPT, associated with high pore pressure, hole cleaning and stuck pipe, could be significantly reduced by implementing pre-drill geomechanical modelling and real-time drilling surveillance. Caicedo *et al*. (2010) also reported that the stuck pipe incidents could be eliminated after introducing a geomechanical approach into their drilling campaign. Their statistic reflects evidence that NPT was primarily associated with a series of mud loss and pack-offs; however, the root cause of these incidents was initially unidentified. Through detailed analyses of drilling performance, combined with integrated geoscience data, they were able to reveal the factors triggering the incidents, and improved their drilling performance in the subsequent drilling campaign. By optimising their mud weight design, Naidu *et al*. (2016) were not just able to drill a horizontal well safely in the highly stresses depleted tight gas sandstone, but also successfully obtained a good production rate due to minimum skin effect in the reservoir. Zadvornov *et al*. (2016) reported that adjustments to the mud weight design in their initial drilling program helped them to avoid potential drilling issues associated with a narrow drilling window, which, if not identified, could have led to severe problems such as wellbore collapse, blowout, stuck pipe, or even loss of the *bottom-hole assembly* (BHA) and the wellbore. Moreover, a 40% NPT reduction was achieved, and the well was completed twenty days ahead of schedule.

## 1.2. Literature review of mechanical wellbore stability

McLellan (1996) summarised that the root causes of wellbore instability based on its origin can be categorised into those associated with controllable or uncontrollable (natural) factors, as shown in Table 1. Wellbore stability, in principle, requires a proper balance between these uncontrollable and controllable factors (Cheatham, 1984), which include wellbore trajectory design and mud weight optimisation to achieve an optimum outcome (Aslannezhad *et al*., 2016). In general, factors causing wellbore instability can be classified into mechanical, chemical, and thermal effects. One of the most common chemically-induced instability problems is caused by water molecules activity due to a salinity imbalance between the drilling mud and the formation fluid, *i.e.* with water flowing from low-salinity fluid to high-salinity fluid. Water adsorption in shales leads to swelling and can cause a significant reduction of the rock strength. In impermeable rocks such as shales, water adsorption can also cause a significant increase in pore pressure near the wellbore wall and gradually lead to unstable wellbore conditions and failure that worsen over time (Bol *et al.*, 1994). In thermally-induced instability, the heating or cooling of the rocks, due to a temperature difference between the circulated mud and the *in situ* condition, will also affect the stability of the wellbore. Cooling of the rocks would reduce the tangential stress and thus improve the stability of the rocks. The reverse effect is observed while heating the rocks; for instance, when the circulated mud, having been heated at the bottom of the well, travels up. The present study is focussed only on the mechanical aspect of wellbore stability.

Table 1. Primary causes of wellbore collapse (McLellan, 1996).

| Uncontrollable factors | Controllable factors |
|---|---|
| Naturally fractured or faulted zones<br>High pore pressures<br>Weak, low strength rocks<br>High *in situ* stresses<br>High *in situ* stress difference* | Well inclination and azimuth<br>Bottom-hole pressure (mud density)<br>Transient pore pressure<br>Physico-chemical rock-fluid interaction<br>Drillstring vibrations<br>Erosion<br>Temperature |

*Added in this research.

Mechanically-induced wellbore instabilities are related to the drilling process, which perturbs the local stress equilibrium. During the drilling process, the pre-existing stress will be redistributed around the wellbore, through which the stresses become concentrated in the rock adjacent to the wellbore wall. In cases where the stress concentration is too large for the rock to withstand, the rock around the wellbore will fail. To overcome this, drilling fluid must be designed to provide sufficient hydrostatic pressure to carry some of the load previously carried by the excavated rock. Thus, the stress concentration around the wellbore could be reduced, depending on the amount of hydrostatic pressure exerted by the drilling fluid in the wellbore. Therefore, it is possible to optimise the minimum hydrostatic pressure required to minimise, if not to avoid, the risk of wellbore collapse. This can be achieved by computing the stresses acting around the wellbore and examining their stability using appropriate failure criteria for a given type of rock and a given *in situ* stress state.

Bradley (1979) summarised that, apart from the cost and operational efficiency, the benefit of having a proper wellbore stability analysis from production and reservoir quality perspectives are improvement in cement quality and, therefore, sand control performance, reduced perforation problems due to thick cement sheaths, and better quality of well-log data. Bradley (1979) grouped mechanically-induced wellbore instability into the following three categories: (1) hole size reduction due to plastic flow of the rock into the borehole (flowing shale and salt); (2) hole enlargement due to rock failing in a brittle manner and falling into the borehole (sloughing shale); and (3) fracturing due to tensile splitting of the rock from excessive wellbore pressure (Figure 1).

Among other categories, hole enlargement due to borehole collapse is considered as the most contributing factor in NPT in oil and gas drilling. Thus, managing wellbore stability requires an integrated knowledge of the mechanism of rock failure, as well as a comprehensive understanding of the surrounding stress field and near-wellbore stresses with respect to the configuration of the regional stress field.

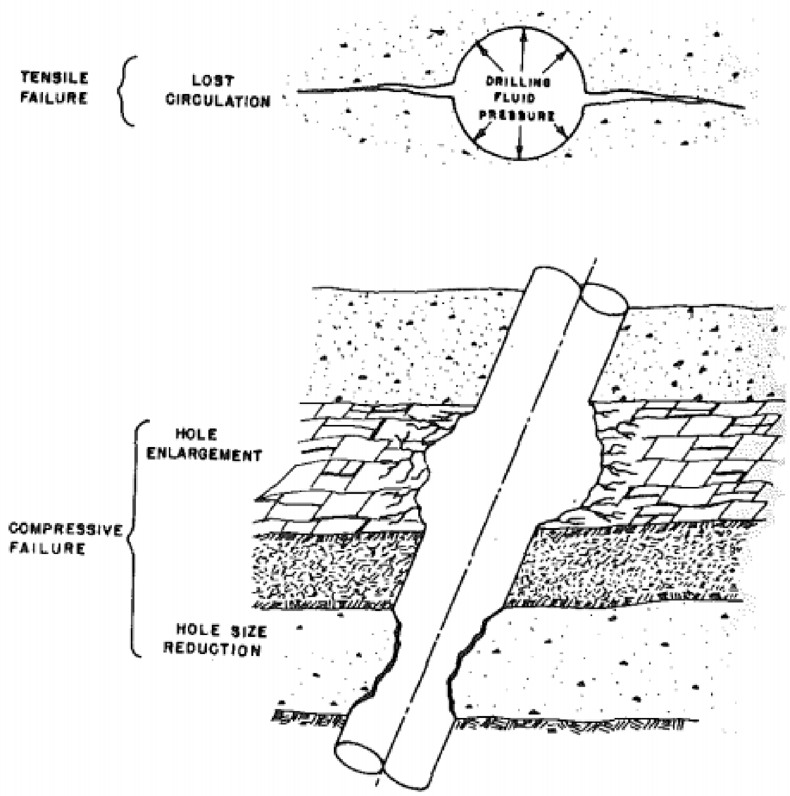


Figure 1. Types of wellbore failure after Bradley (1979).

Bradley (1979) also suggested that to understand problems related to wellbore instability, geoscientists need to have the following knowledge: (1) the *in situ* stress prior the drilling of the wellbore; (2) the extra load carried by the rock after the drilling of the wellbore; (3) the amount of pressure exerted by the drilling fluid to support the extra load carried by the surrounding rocks; (4) the rock strength characteristics; and (5) the effect of drilling fluid on the strength of the rock. For this purpose, Chardac *et al*. (2005) proposed a data acquisition program for a reliable geomechanical analysis which essentially suggested an integration of a multi-disciplinary dataset of petrophysics, geophysics, reservoir, and geology. The analyses can be either done at the planning stage, prior drilling the wellbore, or while drilling through the implementation of logging–

while drilling (LWD) technology and real-time data transmission for instantaneous model updating (see for example Capone *et al*. (2011)).

### *1.2.1. Drilling challenges in anisotropic rocks*

In wellbore stability modelling, it is common practice to assume that the rock is isotropic, even though about 75% of drilling footage must deal with inherently anisotropic shale formations (Gaede *et al*., 2012). This intrinsic characteristic of anisotropy may result from various processes such as sedimentation, compaction, diagenesis, and weathering. Elastic properties such as Poisson's ratio and Young's modulus are reported to show directional properties (Ong & Roegiers, 1995, Wang, 2002). The elastic moduli could differ by about 50% when measured normal and parallel to the bedding (Ong & Roegiers, 1995). In tight gas shale, the variation of the elastic modulus can be up to 400% between the vertical and horizontal directions (Suárez-Rivera *et al*., 2006). Several studies have also shown that rock strength varies relative to the orientation of the planes of anisotropy and the orientation of the major principal stress (Ambrose *et al*. 2014, Ambrose & Zimmerman, 2015, Shi *et al*. 2016, Tien & Kuo, 2001). Ong & Roegiers (1993a) and Ong & Roegiers (1993b) investigated the influence of anisotropy on wellbore stability, and revealed its significant impact on breakout pressure calculation.

Aadnoy & Chenevert (1987) used Mohr-Coulomb and Jaeger's weakness-plane theory to study the behaviour of an inclined wellbore in laminated rocks. They concluded that of wellbore breakout limit becomes more sensitive particularly in the range of 10° to 40° for a tectonically relaxed basin. Okland & Cook (1998) experienced wellbore instability problems in several highly inclined wellbores, which had not been experienced at lower wellbore inclination. They acknowledged that bedding plane splitting had caused the instability, rather than a conventional shear failure of the intact rock. Recommendations were made to avoid drilling parallel to the bedding plane. Aadnoy *et* *al.* (2009) implemented the “plane of weakness” concept to design a deviated wellbore in the Northeastern British Columbia foothills belt in Canada. The relative angle between the borehole and the shale bedding plane was investigated and used as a basis to determine the most stable trajectory while penetrating the problematic zone. Similarly, Zhang (2013) investigated the effect of bedding planes on wellbore instability, and concluded that stability of the wellbore behaves differently with the impact of weak bedding planes. The maximum slip failure locations and directions do not follow those of the conventional breakout, but rather depend on the intrinsic strength and orientation of the bedding planes (Zhang, 2013). From their experience with problematic wells, Wu & Tan (2010) reported that the bedding planes mainly affect wellbores having an inclination greater than 60° and drilled towards the minimum horizontal stress. They found that an additional mud weight of approximately 0.25 pounds-per-gallon (ppg) is necessary to counteract the bedding plane failure against the case without considering the weak planes. They also concluded that, by considering bedding plane failure, the wellbore stability modelling of high-angle wells becomes less sensitive to wellbore azimuth. Narayanasamy *et al*. (2010) applied a rock failure analysis based on the plane of weakness concept to explain many unsuccessful drilling of high-inclination wellbores in Clair oilfield on the UK continental shelf (UKCS). They found through experiences that wellbores could only be stabilised by increasing the mud weight to a value substantially above that suggested by a model based on conventional failure criteria. A series of rock mechanics tests were conducted to define the failure behaviour at various angles to bedding. Hence, incorporating failure of the bedding plane into the geomechanical model had helped them to improve the stability of the wellbore. In all of the cases discussed above, it is obvious that weak bedding plane stability is a complex process and that general conclusions regarding the critical inclination for the plane of weakness cannot be drawn, and are case-specific.

The intrinsic anisotropic behaviour of the rocks can influence wellbore stability in two ways: either by affecting the stress redistribution, or through the rock strength anisotropy (Gazaniol *et al*., 1995). Consequently, in view to develop a more general solution, it is necessary for the modelling of mechanical wellbore stability in anisotropic rocks to involve the following two aspects: (1) the stress calculation for a borehole in an anisotropic rock mass, and (2) determination of appropriate stress-related failure criteria for anisotropic rocks to predict the breakout pressure. In other words, both the elastic and strength anisotropy must be taken into account in the modelling. The first aspect, related to the elastic anisotropy of the rocks, can be addressed using the Lekhnitskii-Amadei solution. Amadei (1983) presented a method to calculate the stress concentration around arbitrarily oriented boreholes in anisotropic rocks of arbitrary orientation, adopted from the pioneering work of Lekhnitskii (1963); hence, in this research, the method is referred to as Lekhnitskii-Amadei.

Aadnoy (1988) implemented the Lekhnitskii-Amadei solution to calculate the limit of fracturing and breakout pressure of an arbitrarily oriented wellbore in rocks with weak bedding planes. Ong & Roegiers (1993b) and Ong & Roegiers (1993a) presented the effect of anisotropy in the wellbore collapse using the Lekhnitskii-Amadei solution. Moreover, to account for the effect of rock strength anisotropy, a generalised strength criterion of Tsai and Wu and Drucker-Prager was adopted in their study. Later, they incorporated poroelastic and thermal effects into the analysis. Similarly, Gupta & Zaman (1999) presented the sensitivity analysis of several parameters, such as the degree of anisotropy and far-field stress ratio, to study their impact on wellbore fracturing and breakout limits. They adopted the minimum normal stress theory for tensile failure, and the Drucker-Prager criterion for the breakout limit. Yan *et al*. (2014) applied the Lekhnitskii-Amadei solution for a wellbore in a shale gas reservoir. In their analysis, the Mohr-Coulomb and the *Jaeger plane of weakness* (JPW) criteria were used to calculate the breakout limit of the intact rock and the bedding plane, respectively. Other authors, *e.g.* Kanfar *et al*. (2015b), Li *et al*. (2015), Lu *et al*. (2015), also used a similar approach for their respective problems. However, in all these applications, except those of Ong & Roegiers (1993b), Ong & Roegiers (1993a) and Gupta & Zaman (1999), the analyses have been limited to the condition of conventional triaxial stress state, *i.e.* the effect of the intermediate stress is not considered in the failure criterion.

### *1.2.2. Stress profile around an irregularly-shaped hole*

All of the models discussed above have neglected the actual shape of the wellbore; the fundamental assumption is that the cross-sectional hole geometry is always a perfect circle. Evaluation of an open hole wellbore stability, open hole hydraulic fracturing and completion design, may still require information regarding the near-wellbore stress state; but, that can only be properly done if the definition of the cross-sectional hole geometry is expanded not only for a *circular* shape. Moreover, in a more general application, it is understood that accurate prediction of the stresses around underground openings or holes in mechanical components is of great importance and is necessary for various purposes not only in petroleum drilling. Highway tunnels, underground mining, oil and gas wells, and other engineering designs often require preliminary evaluation to assess the stability and safety of the structure. In general, for such preliminary studies, the knowledge of the stress state acting around the structure, coupled with the strength characteristics of the material, is essential for predicting the potential risk.

All of the above-mentioned problems related to stress computation for a non-circular geometry can be addressed by means of analytical (or semi-analytical) solutions, or numerical analysis such as finite element or boundary element methods. Recent advances in computing capability have enabled such numerical analysis to become the standard procedure among practitioners and researchers. Nevertheless, analytical solutions are still very useful in providing upfront information about the stress state around openings in elastic materials. Moreover, analytical solutions offer a great advantage to allow for a parametric investigation for such preliminary analyses, such as the influence of material properties or the geometry of the openings.

Several authors have proposed analytical solutions for the calculation of elastic stresses around holes of various shapes. For instance, Greenspan (1944) investigated square and ovaloid holes in isotropic plates, to assess the stress concentration around the hole contour. Daoust & Hoa (1991) proposed a closed-form solution to investigate the stress around a triangular hole in anisotropic plates typically found in the design of aircraft windows. Gercek (1997) and Gercek (1991) investigated the stress around an arched roof with either a flat or parabolic floor; a kind of shapes that are widely used in mining and civil engineering tunnels. In general, the shape of the hole considered in their respective solutions involved simplified geometries such as a circle, ellipse, oval, triangle, square, or other shapes that slightly depart from such standard shapes; this is also true for the analytical solutions for various shapes of holes given by Lekhnitskii (1968) and Savin (1961).

In the above-mentioned studies, the stress is calculated using conformal mapping and the complex displacement potential method developed by Kolosov (1909) and Muskhelishvili (1953). Conformal mapping facilitates the transformation of any given hole shape in one domain into a unit circle in another domain by an appropriate selection of the constants in the mapping function. The solution for the stress components will then be solved in this circular geometry using complex displacement potentials.

In the practical case of wellbore stability, the geometry of the hole can be extremely irregular, unlike all of the above-mentioned cases. One such example is reported by Zoback *et al*. (1985) from wellbores drilled at the Nevada Test Site and Auburn, New

York, USA. For such irregularly-shaped holes, the challenge lies in the determination of the mapping constants that can accurately reproduce the contour of interest, particularly in the regions associated with high-stress concentration. It is, therefore, necessary to have an appropriate mapping procedure that is capable of producing an approximated contour having a minimum misfit with the desired hole shape. One such method is the *Schwarz-Christoffel* (SC) integral that applies for polygons. A comprehensive reference on this method has been written by Driscoll & Trefethen (2002) and supplemented with a conformal mapping toolkit, *i.e.* a Matlab®-based program using the SC method. Despite its robustness, the SC method is mathematically complex. Alternatively, for holes having a relatively smooth contour with a continuously changing tangent, it is possible to use a graphical approach proposed by Melentiev (1937) that is mathematically more convenient.

### 1.3. Objective

The broad objective of this research is two-fold:

(1) to conduct a study on the impact of rock elastic anisotropy and strength anisotropy on mechanical wellbore instability and,

(2) to propose a new solution for the calculation of the in-plane stress for an irregularly-shaped cross-sectional hole commonly observed in petroleum application such as wellbore with breakouts.

For the case of anisotropic wellbore stability modelling, variations of the near-wellbore stress with rock elastic anisotropy, the far-field stress state, and the relative orientation of the wellbore to the bedding plane, are important aspects in examining the stability of the wellbore and these should be included in any analyses. The focus of the first objective is, therefore, to develop a borehole stability model for circular holes in anisotropic rocks. In the model, the true-triaxial stress condition and the rock elastic and strength anisotropy are incorporated. The model will be used to determine the breakout pressure for arbitrary wellbore trajectory and arbitrary rock anisotropy orientation and to examine the impact of the degree of elastic anisotropy on the near-wellbore stress. Sensitivity analysis of the breakout pressure with various parameters will also be evaluated. In summary, by having a better understanding of the behaviour of an anisotropic rock subjected to a true-triaxial stress state, it is expected that the research would be able to provide a better and practical approach to aid drilling operations, for instance, by way of optimising mud weight design and obtaining a more favourable drilling direction in anisotropic rocks.

The second objective is related to the need for a more general solution regarding the geometry of the wellbore. Several authors such as Lu *et al*. (2015), Daoust & Hoa (1991), Gercek (1997), (1991), Greenspan (1944), Lekhnitskii (1968), Savin (1961), Simha & Mohapatra (1998) have solved specific problems in two-dimensional elasticity using a specific mapping function in which the conformal mapping coefficients of the hole are already known. Mitchell (1966) and Exadaktylos *et al*. (2003) also presented a numerical approach to obtain appropriate conformal mapping constants for the stress calculation in a notched circular hole. Exadaktylos & Stavropoulou (2002) proposed a method to compute the conformal mapping function for a hole described by numerical values of its boundary points, and applied it to the solution for the stresses around a pre-stressed horseshoe-shaped tunnel in isotropic, linear elastic materials. Sobey (1964) implemented Melentiev's iterative procedure for a doubly-symmetric hole. Although the above-mentioned methods are general, in that they can be used for any shape of holes, these solutions pertain only to isotropic media. Thus, the second objective of the research is to develop and propose a new method that allows the calculation of the stress around an arbitrary hole of given contour in isotropic or anisotropic media. The method will allow the stress components around an arbitrary hole contour can be computed without *prior* knowledge of the conformal mapping constants. The proposed method is also used to model the wellbore breakout development around a wellbore and to assess if a correlation between breakout geometry and *in situ* stress exists. This will answer, perhaps, the most important question of whether or not the breakout geometry can be used to infer the magnitude of the *in situ* stress. Finally, another potential utilisation of ultrasonic data to obtain the in-plane near-wellbore stress around the wellbore circumference is also investigated.

# Chapter 2 Rock Anisotropy

This chapter provides a brief review of the fundamental concept of elastic anisotropy, such as the constitutive relations and material symmetry commonly used for describing rocks in petroleum applications, and briefly discusses the rock failure criteria applicable for rocks exhibiting strength anisotropy. The review on the anisotropic elasticity presented in this chapter is based on the work of Lekhnitskii (1963) and Amadei (1983). On the rock failure criteria, the work of Al-Ajmi (2006) and Ambrose (2014) is referred to mainly for the discussion on the Mogi-Coulomb and Jaeger plane of weakness failure criteria. This chapter lays the foundation for Chapter 3 and Chapter 4 in which a unified approach in anisotropic wellbore stability model is used to examine the stability of a wellbore in anisotropic rocks. The theory presented in this chapter will also be used as a foundation for Chapter 5 in which a new formula for stress computation around an irregular hole shape in isotropic and anisotropic rocks is proposed.

## 2.1. Introduction

The term *anisotropy* is used to describe a deformation behaviour of materials that vary with direction. Early investigation of such phenomena was motivated by materials such as wood and crystalline solid that naturally possess anisotropic behaviour (Sadd, 2014). In geology and petroleum applications, anisotropy may result from various processes such as sedimentation, compaction, diagenesis, and weathering. Finely laminated sedimentary rock such as shales is often characterised as an anisotropic medium that possesses one axis of symmetry perpendicular to the layering; referred to as *vertical transversely-isotropic* or TIV. In many petroleum applications, it is common practice to assume that the rock is isotropic, even though about 75% of drilling footage must deal with inherently anisotropic shale formations (Gaede *et al*., 2012). Recently, rock anisotropy has become an important factor in many aspects in geophysical data processing and unconventional resource developments, *e.g.* drilling and hydraulic fracturing of shale gas and shale oil. Neglecting the anisotropic characteristic of shale resources may lead to inaccurate estimation of fracture geometry and fracture design optimisation. In oil well drilling, many problems and challenges are attributed to the anisotropic characteristic of the rocks such as that experienced by Okland & Cook (1998), Wu & Tan (2010) and Narayanasamy *et al*. (2010).

## 2.2. Elasticity of anisotropic rocks

### *2.2.1. Generalised Hooke's law*

In elasticity, a constitutive equation relates the *in situ* stress $\sigma_{kl}$ and strain $\varepsilon_{ij}$ components for anisotropic rocks, is described by the following generalised Hooke's law:

$$\varepsilon_{ij} = A_{ijkl}\sigma_{kl} \tag{1}$$

where $A_{ijkl}$ is the fourth-rank elastic compliance tensor that, using Voigt notation, can be written as a 6 × 6 matrix with 21 independent stiffness coefficients. The $A_{ijkl}$ coefficients have definite physical meanings, as can be seen in the following relationship (Lekhnitskii, 1963):

$$\begin{bmatrix}\varepsilon_{xx}\\ \varepsilon_{yy}\\ \varepsilon_{zz}\\ \varepsilon_{yz}\\ \varepsilon_{xz}\\ \varepsilon_{xy}\end{bmatrix}=\begin{bmatrix}\frac{1}{E_x} & -\frac{\nu_{yx}}{E_y} & -\frac{\nu_{zx}}{E_z} & \frac{\eta_{x,yz}}{G_{yz}} & \frac{\eta_{x,xz}}{G_{xz}} & \frac{\eta_{x,xy}}{G_{xy}}\\ -\frac{\nu_{xy}}{E_x} & \frac{1}{E_y} & -\frac{\nu_{zy}}{E_z} & \frac{\eta_{y,yz}}{G_{yz}} & \frac{\eta_{y,xz}}{G_{xz}} & \frac{\eta_{y,xy}}{G_{xy}}\\ -\frac{\nu_{xz}}{E_x} & -\frac{\nu_{yz}}{E_y} & \frac{1}{E_z} & \frac{\eta_{z,yz}}{G_{yz}} & \frac{\eta_{z,xz}}{G_{xz}} & \frac{\eta_{z,xy}}{G_{xy}}\\ \frac{\eta_{yz,x}}{E_x} & \frac{\eta_{yz,y}}{E_y} & \frac{\eta_{yz,z}}{E_z} & \frac{1}{G_{yz}} & \frac{\mu_{yz,xz}}{G_{xz}} & \frac{\mu_{yz,xy}}{G_{xy}}\\ \frac{\eta_{xz,x}}{E_x} & \frac{\eta_{xz,y}}{E_y} & \frac{\eta_{xz,z}}{E_z} & \frac{\mu_{xz,yz}}{G_{yz}} & \frac{1}{G_{xz}} & \frac{\mu_{xz,xy}}{G_{xy}}\\ \frac{\eta_{xy,x}}{E_x} & \frac{\eta_{xy,y}}{E_y} & \frac{\eta_{xy,z}}{E_z} & \frac{\mu_{xy,yz}}{G_{yz}} & \frac{\mu_{xy,xz}}{G_{xz}} & \frac{1}{G_{xy}}\end{bmatrix}\begin{bmatrix}\sigma_{xx}\\ \sigma_{yy}\\ \sigma_{zz}\\ \sigma_{yz}\\ \sigma_{xz}\\ \sigma_{xy}\end{bmatrix} \tag{2}$$

where:

i. $E_x$, $E_y$, $E_z$ are Young's moduli in the $x$, $y$ and $z$ directions.

ii. $G_{yz}$, $G_{xz}$, $G_{xy}$ are the shear moduli on the $yz$, $xz$ and $xy$ planes.

iii. $\nu_{yx}$, $\nu_{zx}$, $\nu_{zy}$, $\nu_{xy}$, $\nu_{xz}$, $\nu_{yz}$ are the Poisson's ratio which can be interpreted as follow: the Poissons ratio $\nu_{ij}$ represents the ratio of the strain in the $j$ direction to the strain in the $i$ direction due to a stress parallel with the $i$ direction. Thus, $\nu_{yx} = \varepsilon_{xx}/\varepsilon_{yy}$ due to a stress acting coincide with the $y$-axis. For this, the following relation holds:

$$\frac{\nu_{ij}}{E_i} = \frac{\nu_{ji}}{E_j} \tag{3}$$

iv. $\mu_{ij,kl}$ is a constant that represents the shear stress in the plane parallel with $ij$ that induces tangential stress in the plane parallel with $kl$. For this, the following relation holds:

$$\frac{\mu_{ik,jk}}{G_{jk}} = \frac{\mu_{jk,ik}}{G_{ik}} \tag{4}$$

v. $\eta_{ij,k}$ represents the shear stress in the plane parallel with $ij$ due to normal stress on the plane $k$. While coefficient $\eta_{k,ij}$ represents the stretching in the direction of $k$ due to shear stress on the plane parallel with $ij$. The following relation holds:

$$\frac{\eta_{ij,k}}{E_k} = \frac{\eta_{k,ij}}{G_{ij}} \tag{5}$$

However, due to physical symmetry, the number of independent coefficients can be reduced which will further simplify the relationship. The constitutive relations of the following case of elastic symmetry will be briefly discussed in the following sub-sections: (1) one plane of elastic symmetry (*monoclinic*); (2) one rotational-axis of elastic symmetry (*transversely isotropic*); (3) three orthogonal planes of elastic symmetry (*orthotropic*); and (4) complete symmetry (*isotropic*). The schematic of these material symmetries is shown in Figure 2.

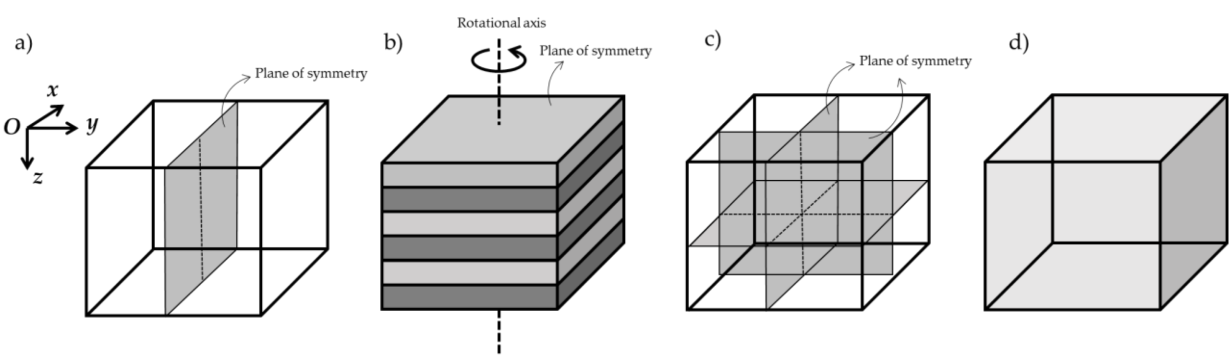


Figure 2. The schematic of material symmetry. (a) monoclinic material, (b) transversely isotropic material, (c) orthotropic material and (d) isotropic material.

### 2.2.2. *One plane of elastic symmetry*

A material is said to possess one plane of elastic symmetry if the elastic constants have the same values for every pair of coordinate systems that are reflected image of one another with respect to the plane (Amadei, 1983). This material is commonly referred to as a *monoclinic*. For instance, if plane $xOy$ is a plane of symmetry, then the following components of the compliance matrix $A_{ijkl}$ are zero:

$$a_{4i} = a_{5i} = a_{46} = a_{56} = 0 \qquad \text{where} \qquad i = 1, 2, 3$$

Then, the constitutive relation consists of 13 independent elastic constants and can be written as

$$\begin{bmatrix} \varepsilon_{xx} \\ \varepsilon_{yy} \\ \varepsilon_{zz} \\ \varepsilon_{yz} \\ \varepsilon_{xz} \\ \varepsilon_{xy} \end{bmatrix} = \begin{bmatrix} \frac{1}{E_x} & -\frac{\nu_{yx}}{E_y} & -\frac{\nu_{zx}}{E_z} & 0 & 0 & \frac{\eta_{x,xy}}{G_{xy}} \\ & \frac{1}{E_y} & -\frac{\nu_{zy}}{E_z} & 0 & 0 & \frac{\eta_{y,xy}}{G_{xy}} \\ & & \frac{1}{E_z} & 0 & 0 & \frac{\eta_{z,xy}}{G_{xy}} \\ & & & \frac{1}{G_{yz}} & \frac{\mu_{yz,xz}}{G_{xz}} & 0 \\ & & & & \frac{1}{G_{xz}} & 0 \\ & & & & & \frac{1}{G_{xy}} \end{bmatrix} \begin{bmatrix} \sigma_{xx} \\ \sigma_{yy} \\ \sigma_{zz} \\ \sigma_{yz} \\ \sigma_{xz} \\ \sigma_{xy} \end{bmatrix} \tag{6}$$

### 2.2.3. *Three orthogonal planes of elastic symmetry*

Materials that possess three orthogonal planes of elastic symmetry that pass through each point of the material is referred to as *orthotropic*. Rocks that possess two sets of fractures oriented 90° to one another can be described as orthotropic materials. The following components of the compliance matrix $A_{ijkl}$ are zero:

$$a_{4i} = a_{5i} = a_{46} = a_{56} = 0 \qquad \text{where} \qquad i = 1, 2, 3$$

$$a_{16} = a_{26} = a_{36} = a_{45} = 0$$

Hence, the constitutive relation consists of only 9 independent elastic constants and can be written as

$$\begin{bmatrix} \varepsilon_{xx} \\ \varepsilon_{yy} \\ \varepsilon_{zz} \\ \varepsilon_{yz} \\ \varepsilon_{xz} \\ \varepsilon_{xy} \end{bmatrix} = \begin{bmatrix} \frac{1}{E_x} & -\frac{\nu_{yx}}{E_y} & -\frac{\nu_{zx}}{E_z} & 0 & 0 & 0 \\ & \frac{1}{E_y} & -\frac{\nu_{zy}}{E_z} & 0 & 0 & 0 \\ & & \frac{1}{E_z} & 0 & 0 & 0 \\ & & & \frac{1}{G_{yz}} & 0 & 0 \\ & & & & \frac{1}{G_{xz}} & 0 \\ & & & & & \frac{1}{G_{xy}} \end{bmatrix} \begin{bmatrix} \sigma_{xx} \\ \sigma_{yy} \\ \sigma_{zz} \\ \sigma_{yz} \\ \sigma_{xz} \\ \sigma_{xy} \end{bmatrix} \tag{7}$$

There are three Young's moduli $E_x = E_y = E_z$, three shear moduli $G_{yz} = G_{xz} = G_{xy}$ and three Poisson's ratio $\nu_{yz} = \nu_{xz} = \nu_{xy}$.

### *2.2.4. One rotational-axis of elastic symmetry*

This type of material symmetry can be specified by stating if an axis of symmetry of order $n$ when the elastic moduli remain unchanged for rotation of $2\pi/n$ radians about the axis. For instance, a hexagonal packing crystalline has $n = 6$ (60° increment). If the rotational axis coincides with the $z$-axis then the material is isotropic within the $xOy$ plane and the $z$-axis is said to be the axis of *radial elastic symmetry* or *elastic symmetry of rotation* (Amadei, 1983). The constitutive relation for this kind of material can be described with the following conditions

$$E_x = E_y = E$$

$$E_z = E'$$

$$\nu_{xy} = \nu_{yx} = \nu_h = \nu$$

$$\nu_{zx} = \nu_{zy} = \nu_v = \nu'$$

$$G_{yz} = G_{xz} = G_v = G'$$

Rocks that possess this type of symmetry are called *transversely isotropic* or commonly written as TI. For instance, shale is commonly described as a transversely-isotropic with a vertical axis of symmetry, or referred to as TIV rocks. The elastic behaviour of shales can then be described by only five independent elastic constants that form the compliance matrix $A_{ijkl}$, *i.e.* two Young's moduli ($E_h$ and $E_v$), two Poisson's ratios ($\nu_v$ and $\nu_h$) and one shear modulus ($G_v$). In other words, the constitutive relation consists of five independent elastic constants. In matrix form, the relationship in Eq. (2) for TIV rocks can be written as:

$$\begin{bmatrix} \varepsilon_{xx} \\ \varepsilon_{yy} \\ \varepsilon_{zz} \\ \varepsilon_{yz} \\ \varepsilon_{xz} \\ \varepsilon_{xy} \end{bmatrix} = \begin{bmatrix} \frac{1}{E_h} & -\frac{\nu_h}{E_h} & -\frac{\nu_v}{E_v} & 0 & 0 & 0 \\ & \frac{1}{E_h} & -\frac{\nu_v}{E_v} & 0 & 0 & 0 \\ & & \frac{1}{E_v} & 0 & 0 & 0 \\ & & & \frac{1}{G_v} & 0 & 0 \\ & & & & \frac{1}{G_v} & 0 \\ & & & & & \frac{1}{G_h} \end{bmatrix} \begin{bmatrix} \sigma_{xx} \\ \sigma_{yy} \\ \sigma_{zz} \\ \sigma_{yz} \\ \sigma_{xz} \\ \sigma_{xy} \end{bmatrix} \tag{8}$$

where the horizontal shear modulus $G_h$ can be expressed in terms of the other two horizontal elastic moduli using the following relationship (Amadei, 1983),

$$G_h = G_{xy} = \frac{E_h}{2(1+\nu_h)} \tag{9}$$

The subscripts $v$ and $h$ denote the normal and in-plane direction of the plane of isotropy, respectively. Thus $\nu_v$ is the vertical Poisson's ratio characterizing transverse contraction in the plane of isotropy due to stress acting in the direction normal to it, and $\nu_h$ is the horizontal Poisson's ratio that corresponds to the transverse contraction in the plane of isotropy due to stress applied also in the plane of isotropy (Lekhnitskii, 1963). For example, Young's modulus of shale is often greater when measured in the plane of bedding than when measured perpendicular to layering. Ambrose (2014) found that the degree of anisotropy ($\eta$), *i.e.* ratio between the horizontal to vertical Young's modulus for Bossier shale and Vaca Muerta shale are 2.88 and 1.62, respectively. It is interesting to note that van Cauwelaert (1977) and Aadnoy (1988) used three elastic constants instead five to represent a TIV medium. However, this idea of reducing the number of elastic constants to three does not seem to have been validated against accurate datasets.

### *2.2.5. Complete symmetry*

This kind of material corresponds to an isotropic case in which all planes and axes are one of elastic symmetry. The most common practice in petroleum geomechanics is to treat rocks as isotropic material. In this case, the number of independent elastic property is further reduced to only two, *i.e.* Young's modulus ($E$) and Poisson's ratio ($\nu$)

$$\begin{bmatrix} \varepsilon_{xx} \\ \varepsilon_{yy} \\ \varepsilon_{zz} \\ \varepsilon_{yz} \\ \varepsilon_{xz} \\ \varepsilon_{xy} \end{bmatrix} = \begin{bmatrix} \frac{1}{E} & -\frac{\nu}{E} & -\frac{\nu}{E} & 0 & 0 & 0 \\ & \frac{1}{E} & -\frac{\nu}{E} & 0 & 0 & 0 \\ & & \frac{1}{E} & 0 & 0 & 0 \\ & & & \frac{1}{G} & 0 & 0 \\ & & & & \frac{1}{G} & 0 \\ & & & & & \frac{1}{G} \end{bmatrix} \begin{bmatrix} \sigma_{xx} \\ \sigma_{yy} \\ \sigma_{zz} \\ \sigma_{yz} \\ \sigma_{xz} \\ \sigma_{xy} \end{bmatrix} \tag{10}$$

whilst the shear modulus ($G$) can be calculated from the other two according to:

$$G = \frac{E}{2(1+\nu)} \tag{11}$$

The implication of these constitutive relations with stability assessment of wellbores can be substantially affecting the drilling strategy, *e.g.* the amount of minimum mud hydrostatic pressure that should be used. A detailed discussion about the influence of elastic anisotropy on the near-wellbore stress and stability of the wellbore will be presented in Chapter 3 and Chapter 4. To build a comprehensive wellbore stability model that incorporated both elastic and strength anisotropy, the failure criteria for the intact and the weak plane will be discussed in the following section.

### 2.3. Rock failure criteria

The other aspect of wellbore stability analysis lies in the selection of criteria to predict the onset of rock failure. Similar to elastic properties, the strength of rocks may also directional-dependent. In this research, to account for a more general case in practical application, a true-triaxial rock failure criteria will be discussed in addition to the standard triaxial failure criteria. And, to incorporate the strength anisotropic behaviour of the rocks, the Jaeger's plane of weakness concept is adopted in this research, thus enabling the examination of the bedding plane slippage propensity. Thus, the effect of elastic and strength anisotropy and *in situ* stress state can be examined and its impact on wellbore stability can be quantified.

### 2.3.1. *Effect of intermediate principal stress – Mogi-Coulomb failure Criteria*

Among other criteria that have been developed by researchers, the Mohr-Coulomb criterion is perhaps the most commonly used, because of its relatively simple mathematical formulation. The criterion states that when the maximum shear stress $\tau_{max}$ on a plane exceeds the shear strength of the rock, *i.e.* represented by its strength parameters cohesion ($S_o$) and the coefficient of internal friction ($\mu$), failure occurs along that plane. According to the criterion, the maximum shear stress that the rock can withstand is linearly correlated with the normal stress $\sigma_n$ acting on the plane; this can be written as:

$$\tau_{max} = S_0 + \mu\sigma_n \tag{12}$$

Equation (12) draws a straight line on the $\sigma_n$-$\tau$ plane and the angle ($\varphi$) that makes the slope of the line is referred to as the *friction angle.* The $\varphi$ and $\mu$ are related by

$$\mu = \tan\varphi \tag{13}$$

The criterion can also be represented in terms of the maximum and minimum principal stresses as (Jaeger *et al.*, 2007)

$$\sigma_1 = 2S_o\frac{\cos\varphi}{1-\sin\varphi} + \sigma_3\frac{1+\sin\varphi}{1-\sin\varphi} \tag{14}$$

Despite its popularity among geoscientists, the Mohr-Coulomb criterion neglects the strengthening effect of the intermediate principal stress, although subsurface rocks are often subjected to three unequal *in situ* stresses. This condition is referred to as to *true-triaxial stress*, or *polyaxial stress*, *i.e.*, when $\sigma_1 > \sigma_2 > \sigma_3$. Mogi (1967) conducted extensive true-triaxial experiments on several rock types, and showed that the intermediate stress appears to have an impact on rock strength. His experimental results and observations led to the development of failure criteria that show the importance of incorporating intermediate principal stress in rock failure analysis.

Numerous researchers have proposed failure criteria that account for all the three principal stresses. Colmenares & Zoback (2002) show the applicability of several failure criteria that commonly used in wellbore stability analysis, such as Drucker-Prager, Modified Wiebols & Cook and Modified Lade. To demonstrate the significance of the intermediate principal stress, the Mogi-Coulomb criterion is adopted in this research. Proposed by Al-Ajmi & Zimmerman (2005), the Mogi-Coulomb criterion is based on Mogi's assumption that the critical octahedral stress ($\tau_{oct}$) at which failure occurs depends on the effective mean stress ($\sigma_{m,2}$). The Mogi-Coulomb criterion can accurately predict true-triaxial behaviour from traditional triaxial datasets (Al-Ajmi & Zimmerman, 2005). The criterion is written as

$$\tau_{oct} = a + b\sigma_{m,2} \tag{15}$$

where, as will be shown, $a$ and $b$ are material constants that can be related to the cohesion and friction angle of the rocks. For a triaxial test, *i.e.* when $\sigma_1 > \sigma_2 = \sigma_3$, Al-Ajmi & Zimmerman (2005) found that the Mogi criterion becomes identical to the Mohr-Coulomb criterion and hence, the two constants $a$ and $b$ can be directly obtained from the Mohr-Coulomb parameters. The final form of the Mogi-Coulomb criterion can be expressed as

$$\tau_{max} = \left(a\,\frac{3}{2\sqrt{2}}\right) + \left(b\,\frac{3}{2\sqrt{2}}\right)\sigma_{m,2} \tag{16}$$

where $\sigma_{m,2} = \frac{1}{2}(\sigma_1 + \sigma_3)$. Comparing the above equation with the Mohr-Coulomb criterion, *i.e.* $\tau_{max} = S_o \cos\varphi_o + \sigma_m \sin\varphi_o$, the parameters $a$ and $b$ can be obtained directly from the Coulomb strength parameters as follows (Al-Ajmi & Zimmerman, 2005):

$$a = \frac{2\sqrt{2}}{3} S_o \cos\varphi_o \quad \text{and} \quad b = \frac{2\sqrt{2}}{3} \sin\varphi_o \tag{17}$$

where $S_o$ and $\varphi_o$ are the cohesion and friction angle of the intact rocks, respectively. Al-Ajmi & Zimmerman (2005) found that, generally, the Mogi-Coulomb criterion is more accurate than both Mohr-Coulomb and Drucker-Prager. Their observation was substantiated by testing the three failure criteria against true-triaxial data sets from a range of rock types. Similar to Mohr-Coulomb, the linear formulation in the Mogi-Coulomb criterion makes it relatively easy to be implemented in wellbore stability analysis, and yet the effect of the intermediate principal stress is considered. In wellbore stability prediction, they observed that the Mohr-Coulomb criterion leads to a more conservative design, as it under-estimate the rock strength at the wellbore wall, as compared to the Drucker-Prager criterion (Al-Ajmi & Zimmerman, 2006).

### 2.3.2. *Effect of strength anisotropy—Jaeger's "Plane of Weakness" model*

Some reservoir rocks, notably shales, are intrinsically anisotropic, and their physical properties, such as strength and deformability, will depend on the orientation of the rock with respect to the principal stresses. A simple conceptual model for the shear failure of laminated rocks such as shales was developed by Jaeger (1960). The Coulomb criterion for failure along the bedding plane is (Jaeger, 1960)

$$|\tau| = S_p + \mu_p \sigma_n \tag{18}$$

where $S_p$ and $\mu_p$ are the shear strength and the friction coefficient of a weakness plane. Jaeger (1960) postulated that for layered, transversely isotropic rocks, failure will occur either at stress and at an angle given by the Coulomb criterion, or along a bedding plane—depending on which value of $\sigma_1$ is lower. In this model, the parallel bedding planes are assumed to be planes of inherent weakness, and failure along such a plane is governed by a Coulomb-type criterion, with a cohesion and an angle of internal friction that are different than, and generally lower than, that of other planes within the rock. The equations that govern the potential failure in terms of principal stress are:

(Intact rock) $$\sigma_1 = 2S_o \tan\left(\frac{\pi}{4} + \frac{\varphi_o}{2}\right) + \sigma_3 \tan^2\left(\frac{\pi}{4} + \frac{\varphi_o}{2}\right) \tag{19a}$$

(Bedding plane) $$\sigma_1 = \sigma_3 + \frac{2S_p + 2\mu_p\sigma_3}{\sin 2\beta_p \left(1 - \mu_p \cot\beta_p\right)} \tag{19b}$$

The angle $\beta_p$ is defined as the angle made by the maximum principal stress $\sigma_1$ and the normal of the bedding plane as shown in Figure 3a. For a fixed value of $\sigma_3$, the value of $\sigma_1$ required to cause failure somewhere within the rock will then be equal to the smaller of the two values given by Eqs. (19a) and (19b). The Jaeger's plane of weakness envelope for various bedding angles $0° < \beta_p < 90°$ is shown in Figure 3b. If the stress given by Eq. (19b) is the lesser of the two, then failure will occur along a plane of weakness, corresponding to the "parabolic" arcs in Figure 3. On the other hand, if the stress given by Eq. (19a) is the lesser, failure will occur along a plane passing through the "intact rock", whose normal vector makes an angle $\beta = 45° + \varphi/2$, with the direction of $\sigma_1$; these cases correspond to envelope describes by the horizontal lines in Figure 3b.

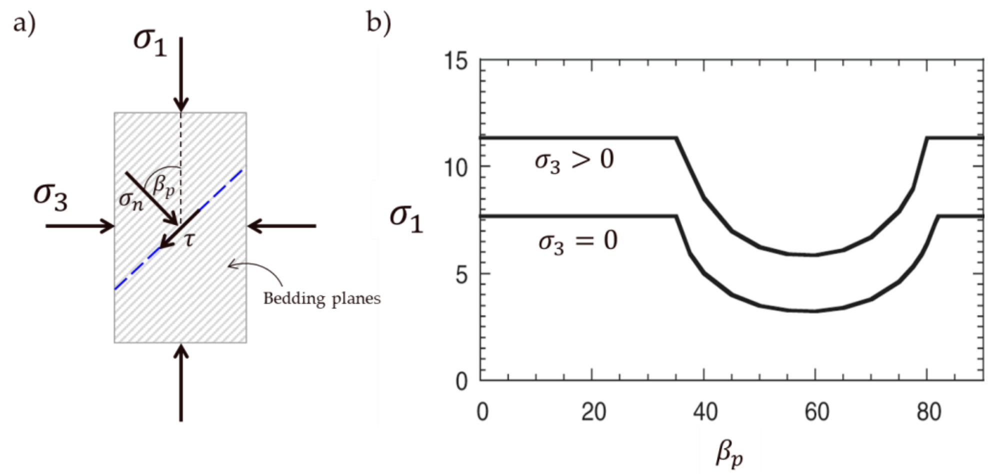


Figure 3. Jaeger's plane of weakness failure envelope.

Ambrose & Zimmerman (2015), who conducted extensive conventional triaxial rock mechanics testing on anisotropic shales, found that the data could be fit reasonably well using Jaeger's plane of weakness criterion for failure along the bedding planes, and the Mohr-Coulomb criterion for failure within the intact rock. A case example will be discussed in Chapter 4 to illustrate the effect of bedding plane on wellbore stability analysis.

# Chapter 3 Near-Wellbore Stress in Anisotropic Rocks

## 3.1. Introduction

The solution for stress calculation of a circular opening for elastic isotropic homogeneous rocks was first published by Ernst Gustav Kirsch, a German engineer, who is primarily known for the Kirsch's equation (Kirsch, 1898). The generalised solution of the Kirsch equation for nonaligned wellbores and regional stress was presented by Hiramatsu & Oka (1968) and Fairhurst (1968). In its generalised formulation, the near-wellbore stress components are calculated as a function of the far-field stresses, the wellbore geometry (its inclination and azimuth) and the wellbore pressure (mud weight). The Kirsch equation expressed in a cylindrical polar coordinate system of $r$-$\theta$-$z$ can be written as

$$\sigma_\theta = \frac{\sigma_{x,0} + \sigma_{y,0}}{2}\left(1 + \frac{R_w^2}{r^2}\right) - \frac{\sigma_{x,0} - \sigma_{y,0}}{2}\left(1 + 3\frac{R_w^4}{r^4}\right)\cos 2\theta - \sigma_{xy,0}\left(1 + 3\frac{R_w^4}{r^4}\right)\sin 2\theta - p_w\left(\frac{R_w^2}{r^2}\right)$$

$$\sigma_r = \frac{\sigma_{x,0} + \sigma_{y,0}}{2}\left(1 - \frac{R_w^2}{r^2}\right) + \frac{\sigma_{x,0} - \sigma_{y,0}}{2}\left(1 + 3\frac{R_w^4}{r^4} - 4\frac{R_w^2}{r^2}\right)\cos 2\theta$$

$$+ \sigma_{xy,0}\left(1 + 3\frac{R_w^4}{r^4} - 4\frac{R_w^2}{r^2}\right)\sin 2\theta + p_w\left(\frac{R_w^2}{r^2}\right)$$

$$\sigma_z = \sigma_{z,0} - \upsilon\left[2\left(\sigma_{x,0} - \sigma_{y,0}\right)\frac{R_w^2}{r^2}\cos 2\theta + 4\sigma_{xy,0}\frac{R_w^2}{r^2}\sin 2\theta\right]$$

$$\sigma_{r\theta} = \frac{\sigma_{x,0} - \sigma_{y,0}}{2}\left(1 - 3\frac{R_w^4}{r^4} + 2\frac{R_w^2}{r^2}\right)\sin 2\theta + \sigma_{xy,0}\left(1 - 3\frac{R_w^4}{r^4} + 2\frac{R_w^2}{r^2}\right)\cos 2\theta$$

$$\sigma_{\theta z} = \left(-\sigma_{xz,0}\sin\theta + \sigma_{yz,0}\cos\theta\right)\left(1 + \frac{R_w^2}{r^2}\right)$$

$$\sigma_{rz} = \left(\sigma_{xz,0}\cos\theta + \sigma_{yz,0}\sin\theta\right)\left(1 - \frac{R_w^2}{r^2}\right) \tag{20}$$

where $r$ represents the radial distance from the borehole wall, $\theta$ represents the angular direction around the wellbore measured from the top of wellbore, and $z$ represents the axial position along the wellbore axis. In the equations above, $\sigma_{x,0}$, $\sigma_{y,0}$ and $\sigma_{z,0}$ refer to the far-field stresses. The Kirsch equation implies that the magnitude of the stresses around a wellbore varies as a function of radial distance ($r$) and angular position ($\theta$). For a non-aligned wellbore trajectory and far-field stress, the shear stress would be non-zero, and therefore the circumferential stress ($\sigma_\theta$), axial stress ($\sigma_z$) and radial stress ($\sigma_r$) are not the principal stresses.

The Kirsch equation was derived based on the classical plane strain assumption, which deals with a situation where the dimension of the body in the longitudinal direction, *i.e.* along the wellbore axis, is extremely large in comparison with the dimension of the other two directions, *i.e.* the wellbore cross-section. It is important to note that, except for the axial stress ($\sigma_z$), *i.e.*, the normal stress acting along the wellbore axis, all the other stress components in the Kirsch equation are independent of the material properties. The axial stress component depends on Poisson's ratio, due to the plane strain assumption that is inherent in the Kirsch equation. Furthermore, the classical plane strain assumption is introduced to simplify the mathematical formulation. It states that the displacement components induced by the forces must be such that the displacements in the $x$ and $y$ directions, *i.e.* $u$ and $v$, are functions of $x$ and $y$ alone, and that the axial displacement $w$ vanishes (Amadei, 1983):

$$\varepsilon_{zz} = -\frac{\partial w}{\partial z};\ \gamma_{xz} = -\left(\frac{\partial u}{\partial z} + \frac{\partial w}{\partial x}\right);\ \gamma_{yz} = -\left(\frac{\partial w}{\partial y} + \frac{\partial v}{\partial z}\right) \tag{21}$$

$$\varepsilon_{zz} = \gamma_{xz} = \gamma_{yz} = 0 \tag{22}$$

Consequently, with regards to anisotropic rocks, the classical plane strain assumption limits the application of the Kirsch equation to the following conditions: (1) the wellbore axis is parallel to the principal stress direction and (2) the material has a maximum of one plane of elastic symmetry that is perpendicular to the wellbore axis. In practice, this limits the solution only for the case of a vertical or horizontal wellbore in isotropic rocks or a wellbore in transversely isotropic rocks where the bedding is orthogonal to the hole axis (Kanfar *et al*., 2015a). Another simplification often made in mechanics is referred to as 'plane stress'. This model is applicable to in-plane loading of thin plates, and is not of much relevance to wellbore stability problems.

### 3.2. The formulation for three-dimensional elasticity problem in anisotropic rocks

Because of the restricted application of the classical plane strain assumption for anisotropic rocks, generalised plane strain concept has been proposed by Lekhnitskii (1963) which served as the basis for the development of the Leknitskii-Amadei solution. In this section, the formulation for the stress around a circular hole in anisotropic rocks will be explained based on the work of Lekhnitskii (1963) and Amadei (1983).

To incorporate the anisotropic deformability behaviour of the rocks, Amadei (1983) presented a method to calculate the stress concentration around arbitrarily oriented boreholes in anisotropic rocks of arbitrary orientation, adopted from the pioneering work of Lekhnitskii (1963). Amadei (1983) addresses the problem of an infinitely long internally-pressurised wellbore that can take an arbitrary orientation penetrating an anisotropic rock subjected to arbitrary external stresses. This makes the Lekhnitskii-Amadei solution relevant to many challenges recently faced by oil and gas practitioners particularly those dealing with drilling, for instance, through shales and interbedded-sandstone where the isotropic solution such as Kirsch equation is no longer valid.

In the Lekhnitkii-Amadei solution, the three-dimensional stress state around the wellbore is calculated by assuming that the wellbore is infinitely long, and the anisotropic body is subjected to three arbitrary external principal stresses (*in situ* stress).

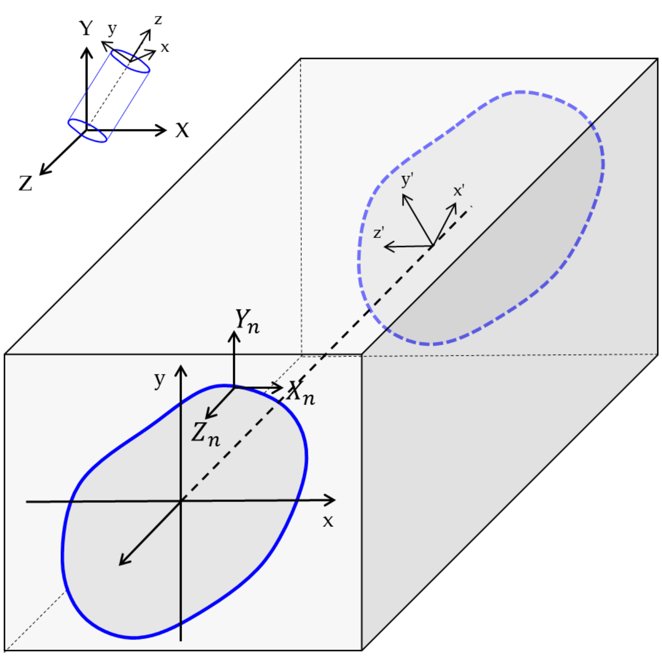


Figure 4. The geometry of the problem after Amadei (1983).

For any problem of elastostatics, the stress, strain and displacement components must satisfy the following equations: (1) the equilibrium equations, (2) the strain compatibility equations, (3) the strain displacement relations, (4) constitutive relations and (5) boundary conditions. The equilibrium equations can be written as:

$$\frac{\partial \sigma_{xx}}{\partial x}+\frac{\partial \sigma_{xy}}{\partial y}+\frac{\partial \sigma_{xz}}{\partial z}+X=0$$

$$\frac{\partial \sigma_{xy}}{\partial x}+\frac{\partial \sigma_{yy}}{\partial y}+\frac{\partial \sigma_{yz}}{\partial z}+Y=0 \tag{23}$$

$$\frac{\partial \sigma_{xz}}{\partial x}+\frac{\partial \sigma_{yz}}{\partial y}+\frac{\partial \sigma_{zz}}{\partial z}+Z=0$$

where $X, Y, Z$ are the components parallel to the axes of the body forces per unit volume. It is assumed that the body forces do not vary along the circular cross-section *i.e.* $Z=0$ and that surface forces do not vary along the generator, *i.e.* the components of the Eq. (23) with respect to $z$-axis are equal to zero, hence the equation of equilibrium can be further simplified to

$$\frac{\partial \sigma_{x}}{\partial x}+\frac{\partial \sigma_{xy}}{\partial y}+X=0$$

$$\frac{\partial \sigma_{xy}}{\partial x}+\frac{\partial \sigma_{y}}{\partial y}+Y=0 \tag{24}$$

$$\frac{\partial \sigma_{xz}}{\partial x}+\frac{\partial \sigma_{yz}}{\partial y}=0$$

The relation of infinitesimal strains and displacement can be written in the following forms

$$\varepsilon_{xx}=-\frac{\partial u}{\partial x};\ \varepsilon_{yy}=-\frac{\partial v}{\partial y};\ \varepsilon_{zz}=-\frac{\partial w}{\partial z} \tag{25}$$

$$\gamma_{xy} = -\left(\frac{\partial u}{\partial y} + \frac{\partial v}{\partial x}\right);\ \gamma_{xz} = -\left(\frac{\partial u}{\partial z} + \frac{\partial w}{\partial x}\right);\ \gamma_{yz} = -\left(\frac{\partial w}{\partial y} + \frac{\partial v}{\partial z}\right) \tag{26}$$

where $u$, $v$, $w$ are the displacements in the $x$, $y$, $z$ directions, respectively. Note that the definition of engineering strain is used here where $\gamma_{xy} = 2\varepsilon_{xy}$ for shear strain and $\gamma_{xx} = \varepsilon_{xx}$ for normal strain. The strain compatibility equations assume that strains are compatible if they result in displacement that produces no separation between the small elements of the body. The six relations between the components of the strain can, therefore, be written as follow:

$$\begin{gathered}
\frac{\partial^2 \varepsilon_{xx}}{\partial y^2} + \frac{\partial^2 \varepsilon_{yy}}{\partial x^2} = \frac{\partial^2 \gamma_{xy}}{\partial x \partial y} \\
\frac{\partial^2 \varepsilon_{yy}}{\partial z^2} + \frac{\partial^2 \varepsilon_{zz}}{\partial y^2} = \frac{\partial^2 \gamma_{yz}}{\partial y \partial z} \\
\frac{\partial^2 \varepsilon_{xx}}{\partial z^2} + \frac{\partial^2 \varepsilon_{zz}}{\partial x^2} = \frac{\partial^2 \gamma_{xz}}{\partial x \partial z} \\
2\frac{\partial^2 \varepsilon_{xx}}{\partial y \partial z} = \frac{\partial}{\partial x}\left(\frac{\partial \gamma_{xz}}{\partial y} + \frac{\partial \gamma_{xy}}{\partial z} - \frac{\partial \gamma_{yz}}{\partial x}\right) \\
2\frac{\partial^2 \varepsilon_{yy}}{\partial x \partial z} = \frac{\partial}{\partial y}\left(\frac{\partial \gamma_{yz}}{\partial x} + \frac{\partial \gamma_{xy}}{\partial z} - \frac{\partial \gamma_{xz}}{\partial y}\right) \\
2\frac{\partial^2 \varepsilon_{zz}}{\partial x \partial y} = \frac{\partial}{\partial z}\left(\frac{\partial \gamma_{yz}}{\partial x} + \frac{\partial \gamma_{xz}}{\partial y} - \frac{\partial \gamma_{xy}}{\partial z}\right)
\end{gathered} \tag{27}$$

The boundary condition along the surface of the circular hole can be expressed as follow:

$$\begin{gathered}
\sigma_{xx}\cos(n,x) + \sigma_{xy}\cos(n,y) = X_n \\
\sigma_{xy}\cos(n,x) + \sigma_{yy}\cos(n,y) = Y_n \\
\sigma_{xz}\cos(n,x) + \sigma_{yz}\cos(n,y) = Z_n
\end{gathered} \tag{28}$$

where $n$ denotes the unit normal vector of the contour and $X_n, Y_n$ and $Z_n$ are the surface forces per unit area acting on the surface of the cylinder. For the case of wellbore stability, these boundary conditions are related to the *in situ* stress and the mud weight. For instance, the traction on the borehole wall is the normal traction which is controlled by the weight of the hydrostatic drilling fluid.

In Eq. (28), the term $\cos(n, x)$ and $\cos(n, y)$ can be expressed in terms of the arc length $S$ of the hole contour (Figure 5):

$$\cos(n, x) = -\frac{dy}{dS} \quad \text{and} \quad \cos(n, y) = \frac{dx}{dS} \tag{29}$$

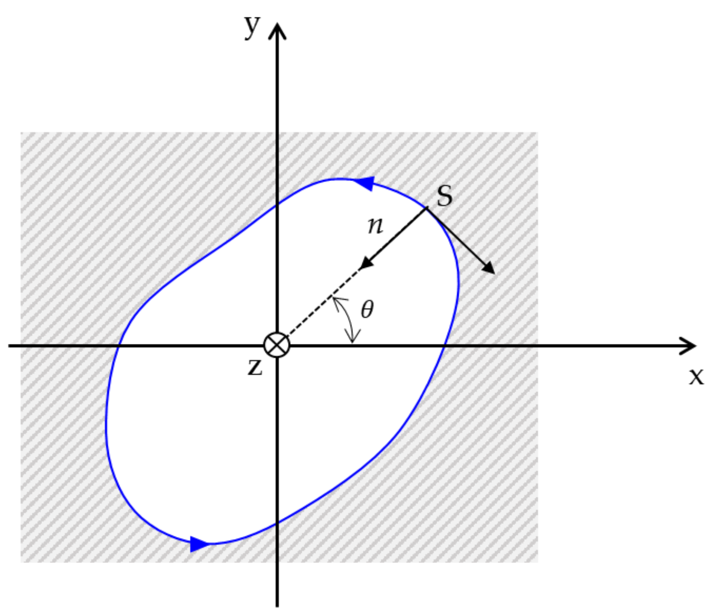


Figure 5. The orientation of the coordinate system attached to the contour of the hole after Amadei (1983).

The stress around the hole induced by the surface and body forces can be determined by introducing two stress function $F(x, y)$ and $\psi(x, y)$ such that

$$\sigma_{xx} = \frac{\partial^2 F}{\partial y^2}; \quad \sigma_{yy} = \frac{\partial^2 F}{\partial x^2} \tag{30}$$

$$\sigma_{xy} = -\frac{\partial^2 F}{\partial x \partial y}; \ \sigma_{xz} = \frac{\partial \psi}{\partial y}; \ \sigma_{yz} = -\frac{\partial \psi}{\partial x} \tag{31}$$

If the stress components are assumed to be independent of the $z$-axis then the strain will also be independent of the $z$-axis through the constitutive relationship. Hence, the strain compatibility Eq. (27) can be simplified to only be dependent on $x$ and $y$. In other words, only the first, fourth and fifth of Eq. (27) are considered,

$$\begin{gathered}
\frac{\partial^2 \varepsilon_{xx}}{\partial y^2} + \frac{\partial^2 \varepsilon_{yy}}{\partial x^2} = \frac{\partial^2 \gamma_{xy}}{\partial x \partial y} \\
2\frac{\partial^2 \varepsilon_{xx}}{\partial y \partial z} = \frac{\partial}{\partial x}\left(\frac{\partial \gamma_{xz}}{\partial y} + \frac{\partial \gamma_{xy}}{\partial z} - \frac{\partial \gamma_{yz}}{\partial x}\right) \\
2\frac{\partial^2 \varepsilon_{yy}}{\partial x \partial z} = \frac{\partial}{\partial y}\left(\frac{\partial \gamma_{yz}}{\partial x} + \frac{\partial \gamma_{xy}}{\partial z} - \frac{\partial \gamma_{xz}}{\partial y}\right)
\end{gathered} \tag{32}$$

Lekhnitskii (1963) introduced a generalised plane strain concept which states that all components of displacement are to be identical in all planes perpendicular to the hole axis, such that

$$\frac{\partial u}{\partial z} = \frac{\partial v}{\partial z} = \frac{\partial w}{\partial z} = 0 \tag{33}$$

$$\varepsilon_{zz} = -\frac{\partial w}{\partial z} = 0 \tag{34}$$

$$\varepsilon_{xx} = -\frac{\partial u}{\partial x} \ ; \ \varepsilon_{yy} = -\frac{\partial v}{\partial y} \tag{35}$$

$$\gamma_{xy} = -\left(\frac{\partial u}{\partial y} + \frac{\partial v}{\partial x}\right); \ \gamma_{xz} = -\left(\frac{\partial u}{\partial z} + \frac{\partial w}{\partial x}\right); \ \gamma_{yz} = -\left(\frac{\partial w}{\partial y} + \frac{\partial v}{\partial z}\right) \tag{36}$$

and hence, only the axial strain ($\varepsilon_{zz}$) vanishes; unlike the classical plane strain in which the anti-plane strain $\gamma_{xz}$ and $\gamma_{yz}$ are also zero (see Eqs. (21) and (22)). To obtain the exact solution of the stress concentration in anisotropic rocks, two stress functions $F(x,y)$ and $\psi(x,y)$ are defined, which are related to the stress components by

$$\sigma_{xx} = \frac{\partial^2 F}{\partial y^2}; \qquad \sigma_{yy} = \frac{\partial^2 F}{\partial x^2}; \qquad \sigma_{xy} = -\frac{\partial^2 F}{\partial x \partial y} \tag{37}$$

$$\sigma_{xz} = -\frac{\partial \psi}{\partial y}; \qquad \sigma_{yz} = -\frac{\partial \psi}{\partial x} \tag{38}$$

Inserting Eqs. (30) and (31) into the equation of equilibrium, constitutive equations, and strain compatibility equations, two coupled differential equations, referred as to the *Beltrami-Michell* equations, are obtained. The exact solution of the near-wellbore stress components can be obtained by simultaneously solving the following Beltrami-Michell equations (Amadei, 1983):

$$L_4 F + L_3 \psi = 0 \tag{39}$$

$$L_3 F + L_2 \psi = 0 \tag{40}$$

in which the linear differential operators $L_2$, $L_3$ and $L_4$, which are associated with the elastic properties of the rocks, can be expressed as:

$$L_2 = \beta_{44}\frac{\partial^2}{\partial x^2} - 2\beta_{45}\frac{\partial^2}{\partial x \partial y} + \beta_{55}\frac{\partial^2}{\partial y^2} \tag{41}$$

$$L_3 = -\beta_{24}\frac{\partial^3}{\partial x^3} + (\beta_{25} + \beta_{46})\frac{\partial^3}{\partial x^2 \partial y} - (\beta_{14} + \beta_{56})\frac{\partial^3}{\partial y^2 \partial x} + \beta_{15}\frac{\partial^3}{\partial y^3} \tag{42}$$

$$L_4 = \beta_{22}\frac{\partial^4}{\partial x^4} - 2\beta_{26}\frac{\partial^4}{\partial x^3 \partial y} - 2\beta_{16}\frac{\partial^4}{\partial y^3 \partial x} + (2\beta_{12} + \beta_{66})\frac{\partial^4}{\partial x^2 \partial y^2} + \beta_{11}\frac{\partial^4}{\partial y^4} \tag{43}$$

where $\beta_{ij} = a_{ij} - \frac{a_{i3}a_{j3}}{a_{33}}$, and $\{a_{ij}\}$ are the components of the compliance tensor $A_{ijkl}$ as in Eq. (1) which corresponds to the rocks elastic property. From the above equations, unlike the Kirsch equation that is independent of the rock elastic properties, it is obvious that the Lekhnitskii-Amadei solution explicitly accounts for the elastic properties of the medium under investigation. Simplifying Eqs. (39) and (40) in terms of $F$ through substitution, it can be obtained that

$$(L_4L_2 - L_3^2)F = 0 \tag{44}$$

and by using the following notation:

$$l_2(\mu) = \beta_{44} - 2\beta_{45}\mu + \beta_{55}\mu^2 \tag{45}$$

$$l_3(\mu) = -\beta_{24} + (\beta_{25} + \beta_{46})\mu - (\beta_{14} + \beta_{56})\mu^2 + \beta_{15}\mu^3 \tag{46}$$

$$l_4(\mu) = \beta_{22} - 2\beta_{26}\mu - 2\beta_{16}\mu^3 + (2\beta_{12} + \beta_{66})\mu^2 + \beta_{11}\mu^4 \tag{47}$$

Lekhnitskii (1963) showed that the operator in Eq. (44) can be written as

$$l_4(\mu)l_2(\mu) - l_3^2(\mu) = 0 \tag{48}$$

which is a sixth-order differential equation that that has six roots of $\mu_k$ $(k = 1, \ldots, 6)$. The six roots are always complex or purely imaginary and three of them are the complex conjugate of the others (Amadei, 1983). Therefore, in solving the equation, one can ignore the conjugate roots and only consider the other three roots as the solution of the equation. It is important to also note that one must use the roots that have positive imaginary parts in the calculation.

Further, by defining three complex number $\lambda_i$ , where $i = 1, 2, 3$, as

$$\lambda_1 = -\frac{l_3(\mu_1)}{l_2(\mu_1)}; \qquad \lambda_2 = -\frac{l_3(\mu_2)}{l_2(\mu_2)}; \qquad \lambda_3 = -\frac{l_3(\mu_3)}{l_4(\mu_3)} \tag{49}$$

Lekhnitskii (1963) showed that the general expressions for the two stress functions $F(x, y)$ and $\psi(x, y)$ take the following forms:

$$F(x, y) = 2Re[F_1(z_1) + F_2(z_2) + F_3(z_3)] \tag{50}$$

$$\psi(x, y) = 2Re\left[\lambda_1 F_1'(z_1) + \lambda_2 F_2'(z_2) + \frac{1}{\lambda_3} F_3'(z_3)\right] \tag{51}$$

where $Re$ takes only the real part of the result in the bracket and $F_k(z_k)$ is an analytic function of the complex variable $z_k = x + \mu_k y$. Its derivation with respect to $z_k$ can be expressed by other forms of analytic functions $\Phi_k = F_k'(z_k)$, defined as:

$$\Phi_1 = F_1'(z_1); \qquad \Phi_2 = F_2'(z_2); \qquad \Phi_3 = \frac{1}{\lambda_3} F_3'(z_3) \tag{52}$$

Thus, using the above definition, the function $\psi(x, y)$ can be expressed as,

$$\psi(x, y) = 2Re[\lambda_1 \Phi_1(z_1) + \lambda_2 \Phi_2(z_2) + \Phi_3(z_3)] \tag{53}$$

and the derivatives of $F(x, y)$ in Eq. (50) with respect to $x$ and $y$ are

$$\frac{\partial F}{\partial x} = 2Re[\Phi_1(z_1) + \Phi_2(z_2) + \lambda_3 \Phi_3(z_3)] \tag{54}$$

$$\frac{\partial F}{\partial y} = 2Re[\mu_1 \Phi_1(z_1) + \mu_2 \Phi_2(z_2) + \lambda_3 \mu_3 \Phi_3(z_3)] \tag{55}$$

The total induced stress components in an anisotropic body bounded internally with a circular hole of infinite length, in Cartesian coordinates, can then be obtained as:

$$\sigma_{xx,h} = \frac{\partial^2 F}{\partial y^2} = 2Re[\mu_1^2 \Phi_1'(z_1) + \mu_2^2 \Phi_2'(z_2) + \lambda_3 \mu_3^2 \Phi_3'(z_3)]$$

$$\sigma_{yy,h} = \frac{\partial^2 F}{\partial x^2} = 2Re[\Phi_1'(z_1) + \Phi_2'(z_2) + \lambda_3 \Phi_3'(z_3)]$$

$$\sigma_{xy,h} = -\frac{\partial^2 F}{\partial x \partial y} = -2Re[\mu_1 \Phi_1'(z_1) + \mu_2 \Phi_2'(z_2) + \lambda_3 \mu_3 \Phi_3'(z_3)] \tag{56}$$

$$\sigma_{xz,h} = -\frac{\partial \psi}{\partial y} = 2Re[\lambda_1 \mu_1 \Phi_1'(z_1) + \lambda_2 \mu_2 \Phi_2'(z_2) + \mu_3 \Phi_3'(z_3)]$$

$$\sigma_{yz,h} = -\frac{\partial \psi}{\partial x} = -2Re[\lambda_1 \Phi_1'(z_1) + \lambda_2 \Phi_2'(z_2) + \Phi_3'(z_3)]$$

where $\Phi_k'(z_k)$ is the derivative of $\Phi_k(z_k)$ with respect to $z_k$. Finally, the total stress components are the sum of the induced stress and the *in situ* stress:

$$\sigma_{xx} = \sigma_{xx}^w + \sigma_{xx,h} = \sigma_{xx}^w + 2Re[\mu_1^2 \Phi_1'(z_1) + \mu_2^2 \Phi_2'(z_2) + \lambda_3 \mu_3^2 \Phi_3'(z_3)]$$

$$\sigma_{yy} = \sigma_{yy}^w + \sigma_{yy,h} = \sigma_{yy}^w + 2Re[\Phi_1'(z_1) + \Phi_2'(z_2) + \lambda_3 \Phi_3'(z_3)]$$

$$\sigma_{xy} = \sigma_{xy}^w + \sigma_{xy,h} = \sigma_{xy}^w - 2Re[\mu_1 \Phi_1'(z_1) + \mu_2 \Phi_2'(z_2) + \lambda_3 \mu_3 \Phi_3'(z_3)] \tag{57}$$

$$\sigma_{xz} = \sigma_{xz}^w + \sigma_{xz,h} = \sigma_{xz}^w + 2Re[\lambda_1 \mu_1 \Phi_1'(z_1) + \lambda_2 \mu_2 \Phi_2'(z_2) + \mu_3 \Phi_3'(z_3)]$$

$$\sigma_{yz} = \sigma_{yz}^w + \sigma_{yz,h} = \sigma_{yz}^w - 2Re[\lambda_1 \Phi_1'(z_1) + \lambda_2 \Phi_2'(z_2) + \Phi_3'(z_3)]$$

in which the stress components $\sigma_{xx}^w$, $\sigma_{yy}^w$, $\sigma_{xy}^w$, $\sigma_{xz}^w$, $\sigma_{yz}^w$ are the *in situ* stress components in the wellbore coordinate system. The transformation of the stress component from the Earth coordinate system to the wellbore coordinate system will be detailed in the next section. The axial stress $\sigma_{zz}$ can be obtained from the constitutive equation by recalling the definition of plane strain, *i.e.* $\varepsilon_{zz} = 0$,

$$\sigma_{zz} = -\frac{1}{a_{33}}\left(a_{31}\sigma_{xx} + a_{32}\sigma_{yy} + a_{34}\sigma_{yz} + a_{35}\sigma_{xz} + a_{36}\sigma_{xy}\right) \tag{58}$$

To find the stress components around the body the two stress functions $F(x, y)$ and $\psi(x, y)$ must also satisfy boundary conditions. If the boundary condition of Eq. (28) is expressed in terms of the two stress functions $F(x,y)$ and $\psi(x,y)$ and using the definition in Eq. (30), the boundary condition can be written as

$$\frac{\partial}{\partial y}\left(\frac{\partial F}{\partial y}\right)\frac{dy}{dS}+\frac{\partial}{\partial x}\left(\frac{\partial F}{\partial y}\right)\frac{dx}{dS}=-X_n$$

$$\frac{\partial}{\partial y}\left(\frac{\partial F}{\partial x}\right)\frac{dy}{dS}+\frac{\partial}{\partial x}\left(\frac{\partial F}{\partial x}\right)\frac{dx}{dS}=Y_n \tag{59}$$

$$\frac{\partial \psi}{\partial x}\frac{dy}{dS}+\frac{\partial \psi}{\partial x}\frac{dx}{dS}=Z_n$$

By integrating the above equations with respect to the arc length $S$, the expressions of the boundary condition as in Eq. (28) expressed in term of the two stress functions $F(x,y)$ and $\psi(x,y)$ can be obtained:

$$\frac{\partial F}{\partial y}=\int_0^S -X_n ds + C_1$$

$$\frac{\partial F}{\partial x}=\int_0^S Y_n ds + C_2 \tag{60}$$

$$\psi = -\int_0^S Z_n ds + C_3$$

And, if the boundary condition in Eq. (60) is combined with the definition of Eqs. (49) to (51), the general expressions of the boundary conditions that relate the stress functions with the analytic functions of complex variables $\Phi_k'(z_k)$, can be derived

$$2Re[\Phi_1(z_1)+\Phi_2(z_2)+\lambda_3\Phi_3(z_3)]=\int_0^S Y_n dS + C_2$$

$$2Re[\mu_1\Phi_1(z_1)+\mu_2\Phi_2(z_2)+\lambda_3\mu_3\Phi_3(z_3)]=\int_0^S -X_n dS + C_1 \tag{61}$$

$$2Re[\lambda_1\Phi_1(z_1)+\lambda_2\Phi_2(z_2)+\Phi_3(z_3)]=-\int_0^S Z_n dS+C_3$$

In summary, as concluded by Amadei (1983), the problem of an anisotropic linear elastic medium that possesses rectilinear anisotropy of a general form and bounded internally by a cylindrical inclusion with an arbitrary orientation is reduced to the determination of three analytic functions of complex variables $\Phi_k = F_k'(z_k)$. These functions must satisfy the boundary conditions on the surface of the hole. Amadei (1983) showed that the derivative of the analytic functions of complex variables $\Phi_k'(z_k)$ can be expressed as

$$\Phi_1'(z_1) = \frac{-1}{r_w\sqrt{\left(\frac{z_1}{r_w}\right)^2-1-\mu_1^2}}\left\{\frac{\left(\bar{a}_1(\mu_2-\lambda_2\lambda_3\mu_3)+\bar{b}_1(\lambda_2\lambda_3-1)+\bar{c}_1\lambda_3(\mu_3-\mu_2)\right)}{\mu_2-\mu_1+\lambda_2\lambda_3(\mu_1-\mu_3)+\lambda_1\lambda_3(\mu_3-\mu_2)}\frac{1}{\xi_1}\right\} \tag{62}$$

$$\Phi_2'(z_2) = \frac{-1}{r_w\sqrt{\left(\frac{z_2}{r_w}\right)^2-1-\mu_2^2}}\left\{\frac{\left(\bar{a}_1(\lambda_1\lambda_3\mu_3-\mu_1)+\bar{b}_1(1-\lambda_1\lambda_3)+\bar{c}_1\lambda_3(\mu_1-\mu_3)\right)}{\mu_2-\mu_1+\lambda_2\lambda_3(\mu_1-\mu_3)+\lambda_1\lambda_3(\mu_3-\mu_2)}\frac{1}{\xi_2}\right\} \tag{63}$$

$$\Phi_3'(z_3) = \frac{-1}{r_w\sqrt{\left(\frac{z_3}{r_w}\right)^2-1-\mu_3^2}}\left\{\frac{\left(\bar{a}_1(\lambda_2\mu_1-\lambda_1\mu_2)+\bar{b}_1(\lambda_1-\lambda_2)+\bar{c}_1(\mu_2-\mu_1)\right)}{\mu_2-\mu_1+\lambda_2\lambda_3(\mu_1-\mu_3)+\lambda_1\lambda_3(\mu_3-\mu_2)}\frac{1}{\xi_3}\right\} \tag{64}$$

where the constants $\bar{a}_1$, $\bar{b}_1$, $\bar{c}_1$ are obtained from the boundary conditions, and can be expressed as (Amadei, 1983)

$$\bar{a}_1=\frac{r_w}{2}\left(p_w-\left(\sigma_{y,o}-i\sigma_{xy,o}\right)\right)$$

$$\bar{b}_1 = \frac{r_w}{2}\left(ip_w + \left(\sigma_{xy,o} - i\sigma_{x,o}\right)\right) \tag{65}$$

$$\bar{c}_1 = \frac{r_w}{2}\left(\sigma_{yz,o} - i\sigma_{xz,o}\right)$$

the expression of $\xi_k$ in Eq. (23) are

$$\xi_k = \frac{\frac{z_k}{r_w} + \sqrt{\left(\frac{z_k}{r_w}\right)^2 - 1 - \mu_k^2}}{1 - i\mu_k}\ ; \qquad \text{where}\ \ k = 1,2,3 \tag{66}$$

where the complex variable $z_k = x + y\mu_k$ is the coordinate of the contour of the circular hole with $x = r_w \cos\theta$ and $y = r_w \sin\theta$; $r_w$ and $p_w$ are the wellbore radius and the wellbore pressure, respectively, and the three complex numbers $\lambda_i$ are defined by Eq. (49).

Validation of the Lekhnitskii-Amadei solution has been carried out by Gaede *et al*. (2012) by comparing the predicted stresses with those of finite element simulations. Gaede *et al*. (2012) demonstrated that the three-dimensional stress profile calculated from the Lekhnitskii-Amadei solution and the finite element simulation results show an excellent agreement at the wellbore wall, and thus validate the application of the Lekhnitskii-Amadei solution for all special cases of symmetry, *i.e.*, transversely anisotropic, orthorhombic and, even, isotropic. The following section discusses the coordinate transformation that is necessary in wellbore stability modelling particularly for the case of a wellbore that is not aligned with one of the principal stresses such as inclined wellbores.

### 3.3. *In situ* stress and rock property coordinate transformation

#### *3.3.1. In situ stress configuration and transformation*

In wellbore stability modelling, the vertical stress $\sigma_v$ is commonly assumed to be one of the principal stresses, although a more generalised assumption is sometimes necessary, *e.g.* when drilling in a geologically faulted structure, tilted principal stress is usually expected. In this research, the orientation of the minimum horizontal stress $\sigma_h$, attached with the earth coordinate system $x$-$y$-$z$, is defined by their angle with respect to the North along the $x$-axis (Figure 6).

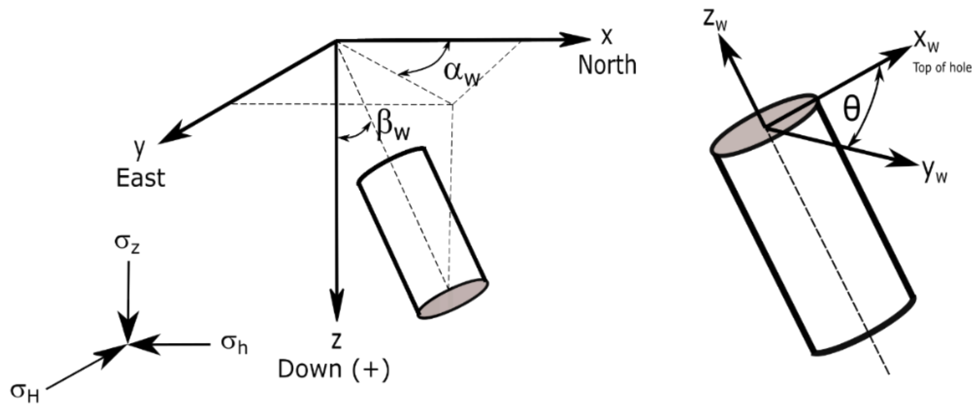


Figure 6. The Earth coordinate system (left) and the wellbore coordinate systems (right).

The wellbore can take an arbitrary orientation, and ties up with the Earth coordinate system by its azimuth $\alpha_w$, measured from north, and inclination angle $\beta_w$ measured with respect to the vertical axis as such a horizontal wellbore is defined by $\beta_w = 90°$. Similarly, the rock property orientation is also attached to the Earth coordinate system by defining their dip azimuth and dip angle, $\alpha_{bp}$ and $\beta_{bp}$, respectively (Figure 7). Since the goal is to evaluate the onset of breakouts at the wellbore wall, it is convenient to transform the *in situ* stress components $\sigma_o$ to the wellbore coordinate system $x_b$-$y_b$-$z_b$. The transformation of the *in situ* stress components $\sigma_o$,

$$\sigma_o = \begin{bmatrix} \sigma_h & 0 & 0 \\ 0 & \sigma_H & 0 \\ 0 & 0 & \sigma_v \end{bmatrix} \tag{67}$$

from the Earth coordinate system $x$-$y$-$z$ into the wellbore coordinate system $x_b$-$y_b$-$z_b$, can be achieved using the following matrix operation:

$$\sigma_{wcs} = R_w\, R_{xyz}^T\, \sigma_o\, R_{xyz}\, R_w{}^T = \begin{bmatrix} \sigma_{xx}^w & \sigma_{xy}^w & \sigma_{xz}^w \\ \sigma_{yx}^w & \sigma_{yy}^w & \sigma_{yz}^w \\ \sigma_{zx}^w & \sigma_{zy}^w & \sigma_{zz}^w \end{bmatrix} \tag{68}$$

in which the rotational matrices $R_{xyz}$ and $R_w$ are defined as

$$R_{xyz} = \begin{bmatrix} \cos\alpha & \sin\alpha & 0 \\ -\sin\alpha & \cos\alpha & 0 \\ 0 & 0 & 1 \end{bmatrix} \tag{69}$$

$$R_w = \begin{bmatrix} \cos\beta_w \cos\alpha_w & \cos\beta_w \sin\alpha_w & \sin\beta_w \\ -\sin\alpha_w & \cos\alpha_w & 0 \\ -\sin\beta_w \cos\alpha_w & -\sin\beta_w \sin\alpha_w\, 0 & \cos\beta_w \end{bmatrix} \tag{70}$$

where $\alpha$ is the azimuth of the minimum horizontal stress measured from north, and $\alpha_w$ and $\beta_w$ are the wellbore azimuth and wellbore inclination, respectively. The superscript $T$ denotes the matrix transpose.

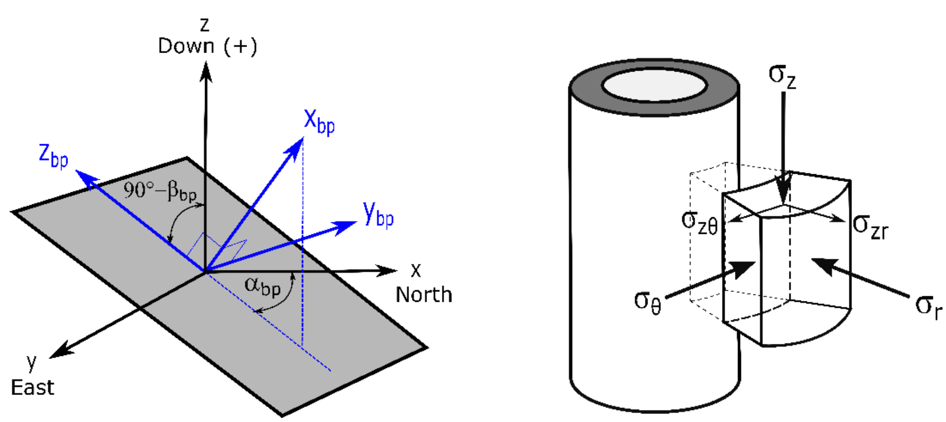


Figure 7. The bedding plane local axes and the stress components around the wellbore.

### *3.3.2. Material property transformation*

The transformation process of the compliance tensor into wellbore coordinate system requires two 6 × 6 transformation matrices $M_\varepsilon$ and $N_\sigma$, written as (Amadei, 1983):

$$M_\varepsilon = \begin{bmatrix} l_{11}^2 & l_{12}^2 & l_{13}^2 & l_{12}l_{13} & l_{13}l_{11} & l_{12}l_{11} \\ l_{21}^2 & l_{22}^2 & l_{23}^2 & l_{23}l_{22} & l_{23}l_{21} & l_{22}l_{21} \\ l_{31}^2 & l_{32}^2 & l_{33}^2 & l_{33}l_{32} & l_{33}l_{31} & l_{32}l_{31} \\ 2l_{11}l_{21} & 2l_{32}l_{22} & 2l_{33}l_{23} & l_{33}l_{22}+l_{32}l_{23} & l_{33}l_{21}+l_{31}l_{23} & l_{31}l_{22}+l_{32}l_{21} \\ 2l_{11}l_{31} & 2l_{32}l_{12} & 2l_{33}l_{13} & l_{33}l_{13}+l_{32}l_{13} & l_{33}l_{11}+l_{31}l_{13} & l_{31}l_{12}+l_{32}l_{11} \\ 2l_{21}l_{31} & 2l_{12}l_{22} & 2l_{13}l_{23} & l_{13}l_{22}+l_{12}l_{23} & l_{13}l_{21}+l_{11}l_{23} & l_{11}l_{22}+l_{12}l_{21} \end{bmatrix} \tag{71}$$

$$N_\sigma = \begin{bmatrix} l_{11}^2 & l_{12}^2 & l_{13}^2 & 2l_{12}l_{13} & 2l_{13}l_{11} & 2l_{12}l_{11} \\ l_{21}^2 & l_{22}^2 & l_{23}^2 & 2l_{23}l_{22} & 2l_{23}l_{21} & 2l_{22}l_{21} \\ l_{31}^2 & l_{32}^2 & l_{33}^2 & 2l_{33}l_{32} & 2l_{33}l_{31} & 2l_{32}l_{31} \\ l_{11}l_{21} & l_{32}l_{22} & l_{33}l_{23} & l_{33}l_{22}+l_{32}l_{23} & l_{33}l_{21}+l_{31}l_{23} & l_{31}l_{22}+l_{32}l_{21} \\ l_{11}l_{31} & l_{32}l_{12} & l_{33}l_{13} & l_{33}l_{13}+l_{32}l_{13} & l_{33}l_{11}+l_{31}l_{13} & l_{31}l_{12}+l_{32}l_{11} \\ l_{21}l_{31} & l_{12}l_{22} & l_{13}l_{23} & l_{13}l_{22}+l_{12}l_{23} & l_{13}l_{21}+l_{11}l_{23} & l_{11}l_{22}+l_{12}l_{21} \end{bmatrix} \tag{72}$$

The components of the strain transformation matrix $M_\varepsilon$ with respect to wellbore coordinate system are:

$$\begin{aligned} &l_{11} = \cos\beta_w \cos\alpha_w && l_{12} = \cos\beta_w \sin\alpha_w && l_{13} = \sin\beta_w \\ &l_{21} = -\sin\alpha_w && l_{22} = \cos\alpha_w && l_{23} = 0 \\ &l_{31} = -\sin\beta_w \cos\alpha_w && l_{32} = -\sin\beta_w \sin\alpha_w && l_{33} = \cos\beta_w \end{aligned} \tag{73}$$

while the components for the stress transformation $N_\sigma$ can be obtained from the bedding dip azimuth ($\alpha_{bp}$) and dip angle ($\beta_{bp}$), as such $\beta_{bp} = 90°$ describes a horizontal plane (see Figure 7), as follow,

$$l_{11} = \cos(90° - \beta_{bp}) \cos \alpha_{bp} \quad l_{12} = \cos(90° - \beta_{bp}) \sin \alpha_{bp} \quad l_{13} = \sin(90° - \beta_{bp})$$

$$l_{21} = -\sin \alpha_{bp} \quad l_{22} = \cos \alpha_{bp} \quad l_{23} = 0 \tag{74}$$

$$l_{31} = -\sin(90° - \beta_{bp}) \cos \alpha_{bp} \quad l_{32} = -\sin(90° - \beta_{bp}) \sin \alpha_{bp} \quad l_{33} = \cos(90° - \beta_{bp})$$

Making use of the two transformation matrices in Eqs. (71) and (72), the transformation process for a compliance tensor $A_{ijkl}$ can be achieved by

$$A_t = M_\varepsilon \, N_\sigma^T \, A \, N_\sigma \, M_\varepsilon^T \tag{75}$$

### 3.4. The near-wellbore stress modelling and validation

The overall workflow to determine the onset of wellbore stability, *i.e.* breakout pressure, is shown in Figure 9. Breakout pressure in this report is defined as the minimum mud pressure to avoid shear failure. Hence, according to this definition, the shear failure does not occur if the mud pressure is higher than the breakout pressure. Essentially, the workflow for breakout pressure calculation of an arbitrary wellbore orientation in transversely isotropic rocks with a vertical axis of symmetry (TIV) can be divided into three key steps: (1) the transformation of the *in situ* stress components and the rock elastic tensor from the Earth coordinate system to the wellbore coordinate system and then (2) then the calculation of the near-wellbore stress using Lekhnitskii-Amadei solution, and (3) the calculation and examination of the shear failure of the intact rock and bedding plane around the wellbore circumference; which will be discussed in Chapter 4. Prior to the computation of the stability of the wellbore, validation with that of Gaede *et al*. (2012) will be first carried out to ensure the Lekhnitskii-Amadei solution is properly translated into Matlab codes. To validate the Lekhnitskii-Amadei solution, Gaede *et al*. (2012) used a commercial finite element solver COMSOL to develop a 3D model that can compute the stresses around a borehole in an arbitrarily anisotropic medium. To validate our Matlab code, their finite element simulation results have been digitised using a computeraided software and were used to benchmark the codes for several scenarios including vertical, deviated and horizontal wellbores in transversely-isotropic rock with a vertical axis of symmetry (TIV) and *tilted-transversely-isotropic* (TTI) rocks.

The comparison with that of Gaede *et al*. (2012) for a TIV (top panel) and TTI (bottom panel) rocks is shown in Figure 8. The black-dots are the finite element simulation results digitised from Gaede *et al*. (2012). The first, second and third columns in Figure 8 are for the case of vertical, deviated with 45° inclination and horizontal wellbores, respectively. The red curve shows the tangential stress ($\sigma_\theta$), purple and blue curve are the radial ($\sigma_r$) and axial stress ($\sigma_\theta$) and the shear stress ($\sigma_{\theta z}$) is shown by the green curve. For all possible cases, the results are in excellent agreement with the finite element simulation and, thus, validate the codes.

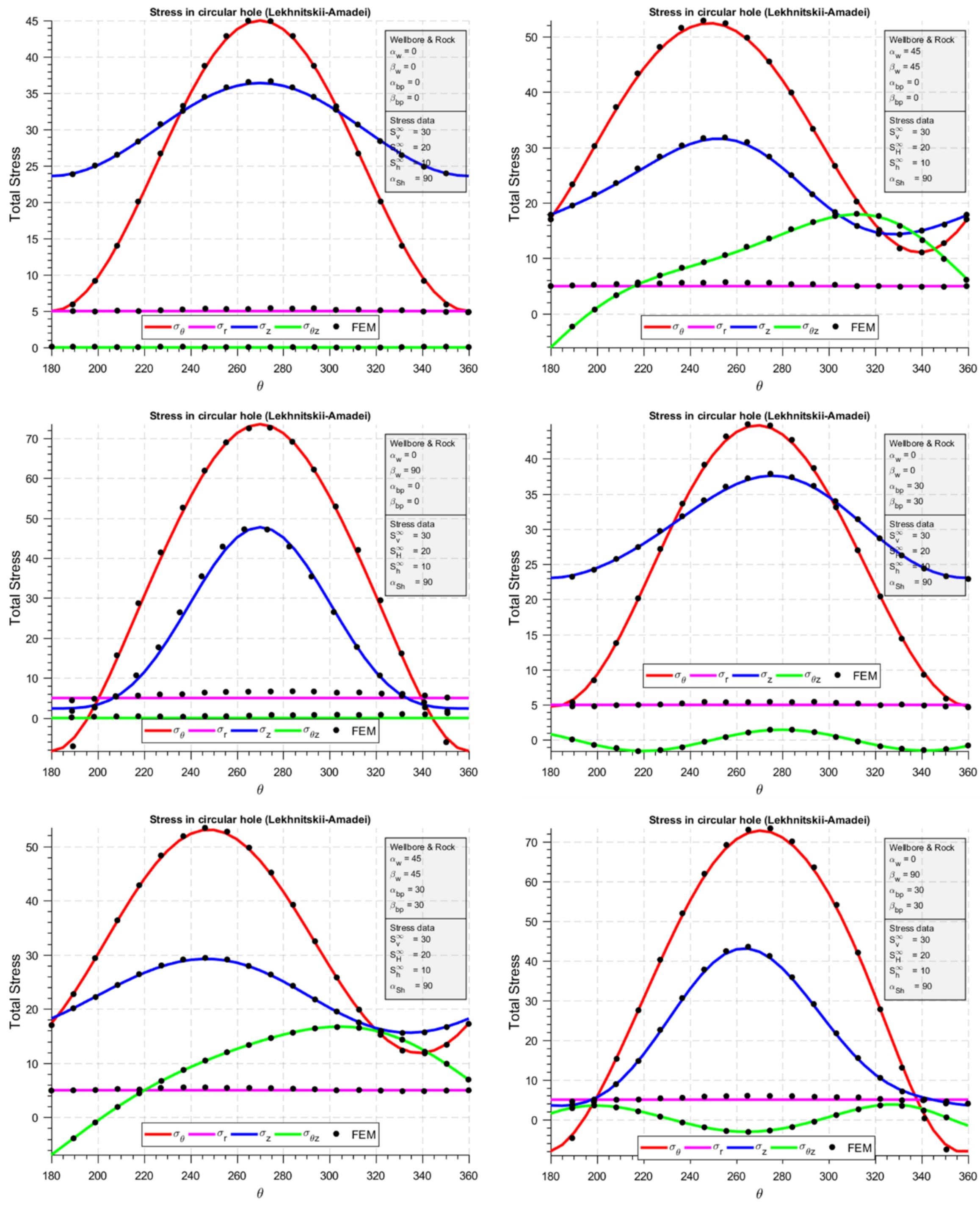


Figure 8. Comparison with the numerical simulation results of Gaede *et al*. (2012) for a TIV (top panel) and TTI (bottom panel) rocks. The black-dots are the finite element simulation results digitised from Gaede *et al*. (2012).

A hypothetical case of a vertical wellbore penetrating a TIV rock has also been used to validate the code. The *in situ* stress state is assumed to be in the normal fault stress regime, where $\sigma_v > \sigma_H > \sigma_h$ with a considerable horizontal stress magnitude difference. The overburden stress ($\sigma_v$) gradient is assumed to be 1.0 psi/ft, and the maximum ($\sigma_H$) and minimum horizontal stress ($\sigma_h$) gradients are 0.85 psi/ft and 0.7 psi/ft, respectively, at depth of 10,000 ft. The azimuth of the minimum horizontal stress is N 120° E and the pore pressure gradient is 0.43 psi/ft. The elastic properties of the TIV rocks, listed in Table 2, are adopted from the work of Ambrose (2014) who conducted an extensive triaxial test on Vaca Muerta shale, indicating a degree of anisotropy ($\eta = \frac{E_h}{E_v}$) of 1.62.

Table 2. Elastic properties of Vaca Muerta rock (Ambrose, 2014).

| | Young's modulus (MPsi) | Poisson's ratio (-) | Shear modulus (MPsi) |
|---|---|---|---|
| Vertical | 2.40 | 0.18 | 1.24 |
| Horizontal | 3.88 | 0.24 | 1.56 |
| Degree of anisotropy ($\eta$) | 1.62 | | 1.26 |

The vertical Poisson's ratio ($\nu_v$) in Table 2 characterise transverse contraction in the plane of isotropy due to stress acting in the direction normal to it, and the horizontal Poisson's ratio ($\nu_h$) corresponds to the transverse contraction in the plane of isotropy due to stress applied also in the plane of isotropy.

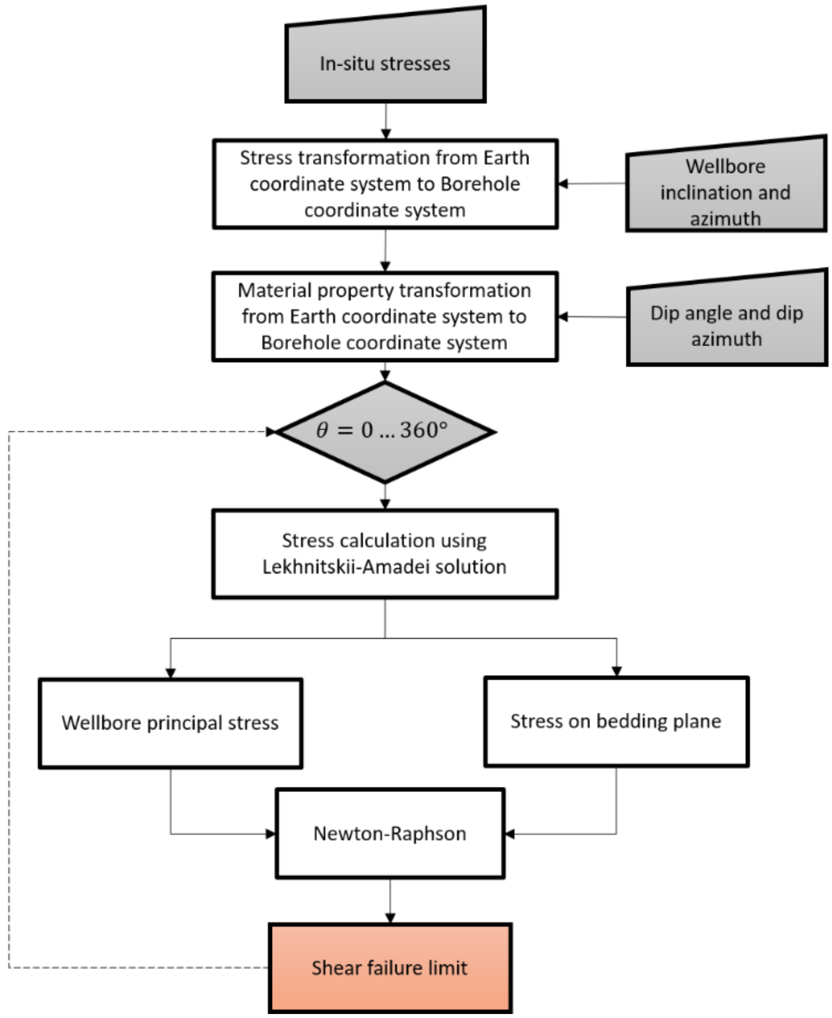


Figure 9. The workflow to determine the breakout pressure limit at the wellbore wall.

In this special case of anisotropy, when the wellbore axis coincides with the rock axis of symmetry, the presence of elastic anisotropy would *not* affect the near-wellbore stress. This is because the two differential Beltrami-Michell equations, see Eqs. (39) and (40), are no longer coupled (Amadei, 1983). Thus, the Kirsch solution can be used as a benchmark for the in-plane stress components $\sigma_\theta$, $\sigma_r$ as well as $\sigma_z$ if the Poisson's ratio in the Kirsch equation is replaced with the vertical Poisson's ratio ($\nu_v$) of the anisotropic rocks. The validated result, shown in Figure 10, shows excellent agreement between the near-wellbore stress components modelled using the Leknitskii-Amadei solution and the Kirsch equation, around the wellbore circumference and up to two wellbore radii into the formation.

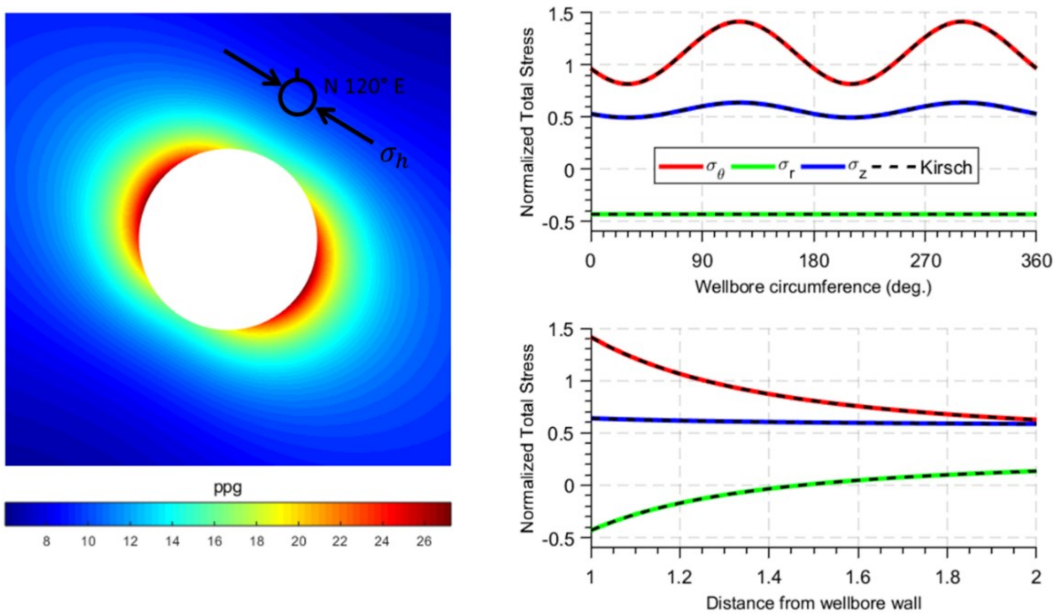


Figure 10. The tangential stress ($\sigma_\theta$) distribution up to two wellbore radii using the Lekhnitskii-Amadei solution (left) and comparison of the stress components at the wellbore wall calculated using the Lekhnitskii-Amadei solution (solid curve) and Kirsch equation (black dash-line) of a vertical wellbore in TIV rocks where the two methods show an excellent agreement (top and bottom right). The azimuth of the minimum horizontal stress is N 120° E.

Upon validating the code and to examine the effect of anisotropic elastic property on the near-wellbore stress distribution, the case was then generalised into an inclined wellbore penetrating a TIV rock. For a 15° deviated wellbore drilled perpendicular to the minimum horizontal stress direction, the effect of the elastic anisotropy embedded in the

Lekhnitskii-Amadei solution is more prominent and, hence, the difference with that of Hiramatsu-Oka solution is more pronounced (Figure 11).

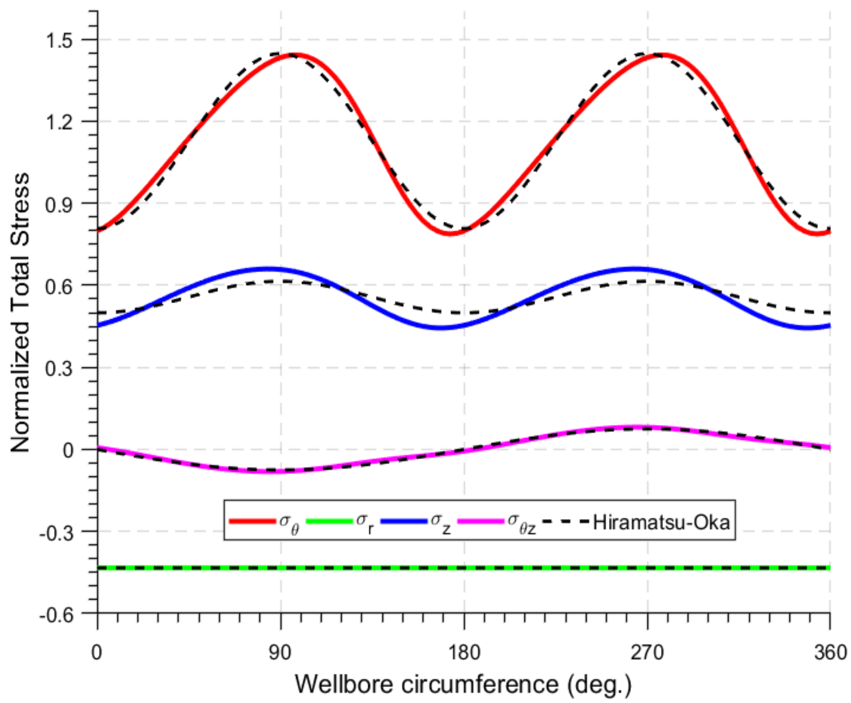


Figure 11. Stress components at the wall of a 15° deviated wellbore drilled perpendicular to the minimum horizontal stress in a TIV rock. For an inclined wellbore, the effect of elastic anisotropy is more prominent and hence the near-wellbore stress components from Lekhnitskii-Amadei (solid curves) are different with that of isotropic (Hiramatsu-Oka) equation (black dash-line). The azimuth of the minimum horizontal stress is N 120° E. The near-wellbore stress has been normalised with the *in situ* vertical stress ($\sigma_v$).

Although, for this case, the tangential stress ($\sigma_\theta$) difference between the two methods is approximately 5%, there is more than 13% difference observed on the axial stress ($\sigma_z$) which will alter the magnitude of the breakout pressure. In Figure 12, the magnitude of the stresses has been normalised with the *in situ* vertical stress ($\sigma_v$). A detailed examination also suggests that there is a phase shift on the peak stress location which will affect not only the potential breakout location but also, on a broader sense, the optimum drilling direction.

### 3.5. Effect of elastic anisotropy on the near-wellbore principal stress

To demonstrate the dependency of the near-wellbore stress on elastic anisotropy, a parametric study was carried out by varying the degree of anisotropy ($\eta$). In Figure 12a, it is shown that a higher degree of anisotropy appears to induce more stress concentration compared to the case with a lower degree of anisotropy. The difference with that of the isotropic case could reach approximately 30% for the highest degree of anisotropy compared with that of the isotropic case. Figure 12b illustrates the difference of the other near-wellbore stress components with that of the isotropic case. Recalling that the intermediate principal stress has an influence on rock strength, the magnitude of the breakout pressure would be altered if one ignores the presence of the intermediate principal stress. Moreover, the case shown in Figure 12b emphasizes not only the importance of considering the intermediate stress, but more importantly, neglecting elastic anisotropy would also affect the breakout pressure attributed to the reduction of the tangential stress and axial stress by approximately 5% and 35%, respectively.

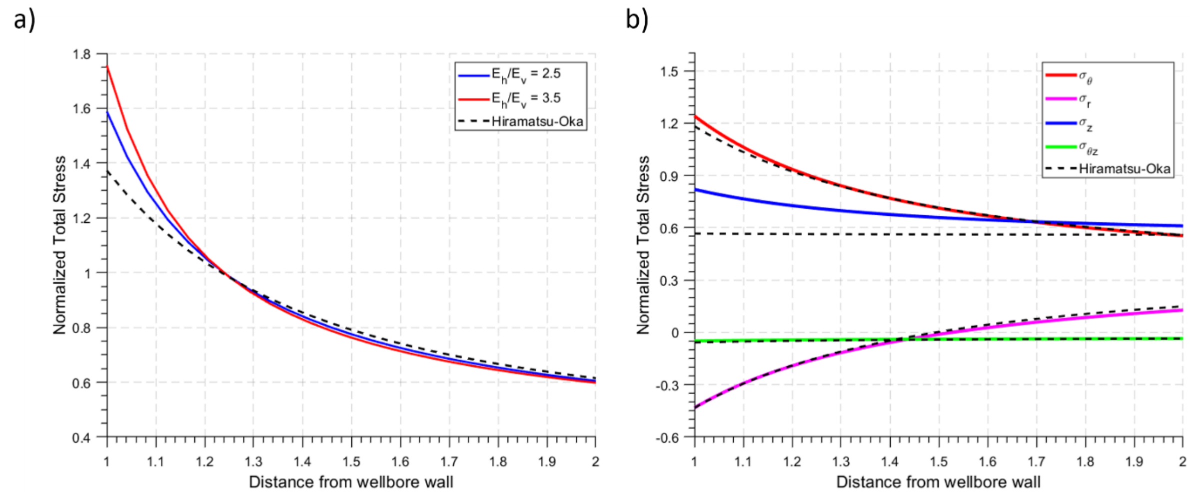


Figure 12. (a) The near-wellbore major principal stress for various degree of anisotropy ($\eta$) of a deviated wellbore with 15° inclination drilled perpendicular to the minimum horizontal stress in a TIV rock. The difference with that of the isotropic case (black dash-line) is approximately 25% for the highest degree of anisotropy (red curve). (b) At the wellbore wall, the difference of the anisotropic near-wellbore stress components with that of isotropic (Hiramatsu-Oka) solution is approximately 5% and 35% for tangential stress and axial stress, respectively. The case was run assuming a degree of anisotropy $\eta = 3.0$.

# Chapter 4 Wellbore Stability Modelling

## 4.1. Introduction

This chapter presents a unified approach through which the influence of the elastic and strength anisotropy on wellbore instability can be thoroughly examined. The stresses at the wellbore wall are first calculated using the Lekhnitskii-Amadei solution outlined in Chapter 3, which accounts for elastic anisotropy. Then, shear failure is treated by combining the Mohr-Coulomb or Mogi-Coulomb criterion for intact rock, with the Jaeger plane of weakness concept (Chapter 2). By utilising the Mogi-Coulomb criterion for the intact rock, the developed model accounts for all three principal stresses in predicting the onset of shear failure.

As described in Chapter 1, many drilling problems can only be addressed by considering the anisotropic behaviour of the rocks. To demonstrate the influence of the anisotropic characteristic and the true-triaxial stress state, a hypothetical example has been presented. The results of the specific case considered here show that rock elastic anisotropy induces higher stress concentration. As shown in Chapter 3, the difference compared with the stresses found using the isotropic elastic model, could reach as high as 25% for the highest degree of anisotropy that might be expected for rocks of practical interest. As will be shown in the following sections, the strengthening effect of the intermediate stress, as reflected in the Mogi-Coulomb criterion, reduces the required mud weight density by approximately 1.0 pounds-per-gallon (ppg). Furthermore, it will be demonstrated that the risk posed by bedding slippage, for a wellbore with an inclination between 15°–50° from the vertical, is masked when an isotropic elastic stress model is used. In contrast, the fully anisotropic model shows that an extra mud weight of approximately 4.5 ppg would be required, to avoid bedding plane slippage for the case under investigation. Although these results apply for a particular choice of strength properties and elastic properties, they give an indication of the implications of fully accounting for anisotropy and the effect of the intermediate stress when doing borehole stability analysis.

### 4.2. Calculation of breakout pressure and examination of the shear failure limit

The workflow for breakout pressure calculation of an arbitrary wellbore orientation in transversely isotropic rocks with a vertical axis of symmetry (TIV) can be divided into three key steps: (1) the transformation of the *in situ* stress components and the rock elastic tensor from the Earth coordinate system to the wellbore coordinate system, (2) calculation of the near-wellbore stress using Lekhnitskii-Amadei solution, and (3) calculation and examination of the shear failure of the intact rock and bedding plane around the wellbore circumference.

To incorporate the anisotropic characteristic of the rocks, the Lekhnitskii-Amadei solution is used to obtain the three-dimensional near-wellbore stress components, after which, by means of Newton-Raphson technique, the solution of the minimum mud pressure, and therefore the principal stress components that satisfy the failure criteria, can be obtained. The solution sought using the Newton-Raphson iteration is obtained by setting a tolerance of $10^{-4}$ with an initial value for the mud pressure set to zero. The highest mud pressure around the wellbore circumference is then taken as the minimum breakout pressure. Similarly, to determine the slippage onset of the bedding plane, the near-wellbore stress was projected onto the bedding orientation, after which the minimum mud pressure that satisfies the Jaeger's plane of weakness criterion is determined. The overall breakout limit is then obtained by contrasting the breakout for the intact rock with that of the bedding plane. The higher of the two was chosen as the overall breakout limit. The general workflow describing the procedure is shown in Figure 9. Although conceptually, failures can occur either along the bedding plane or through the intact rock. In reality, as shown by Ambrose (2014), the failure process involving bedding plane weakness is complicated that for a certain case it is difficult to distinguish a rock failure induced by only the bedding plane or only the intact portion of the rocks.

To predict the onset of the wellbore wall instability, upon obtaining the near-wellbore stress, the principal stress must then be calculated and inserted into the failure criterion. Acting on a free surface at the wellbore wall, the radial stress ($\sigma_r$), exerted by the hydrostatic pressure of the drilling mud, is always one of the principal stresses, while the other two must act on any surface such that the three are perpendicular to each other. For instance, as clearly shown in Figure 11, the anti-plane shear stress $\sigma_{\theta z}$ is non-zero, thus $\sigma_\theta$ and $\sigma_z$ are not the principal stresses. Hence, the other two principal stress components must be obtained from the axial stress ($\sigma_z$), tangential stress ($\sigma_\theta$) and the shear stress $\sigma_{\theta z}$ using the following relationship:

$$\sigma_{P1,2} = \frac{\sigma_\theta + \sigma_z}{2} \pm \sqrt{\sigma_{\theta z}^2 + \frac{(\sigma_\theta + \sigma_z)^2}{4}} \tag{76}$$

The internal wellbore pressure ($p_w$) affects the near-wellbore stress as such, for example, the tangential stress ($\sigma_\theta$) decreases with the increasing ($p_w$). For instance, if the Mohr-Coulomb failure criterion is considered, then rearranging Eq. (14) leads to the following relation

$$F = \sigma_1 - \left(2S_o \frac{\cos\varphi}{1-\sin\varphi} + \sigma_3 \frac{1+\sin\varphi}{1-\sin\varphi}\right) \tag{77}$$

in which $F$ is the failure function describing the stability of the rock as a function of the internal wellbore pressure ($p_w$), the stress state and the rock strength properties (Figure 13). The principal stress component in the failure criteria in Eq. (77) should be used in terms of the effective stress in which the effect of pore pressure $p_p$ has been subtracted from the total principal stress. Therefore, the underlining concept in any breakout limit calculation is to determine the necessary value of the mud pressure $p_w$ to avoid shear failure that satisfies the chosen failure criterion for a given rock strength and given *in situ* stress configuration, as illustrated in Figure 9. The procedure to determine the minimum mud pressure to avoid breakout is shown in Figure 13. Initially, as the mud pressure ($\sigma_3$) monotonically increases, the failure function ($F$) decreases and crosses zero when it satisfies the failure criterion (Figure 13a). The Mohr circle of this stress state will touch the failure line as shown in Figure 13b and Figure 13c. To determine the minimum mud pressure to avoid breakout, the iteration is terminated once the failure function ($F$) crosses zero.

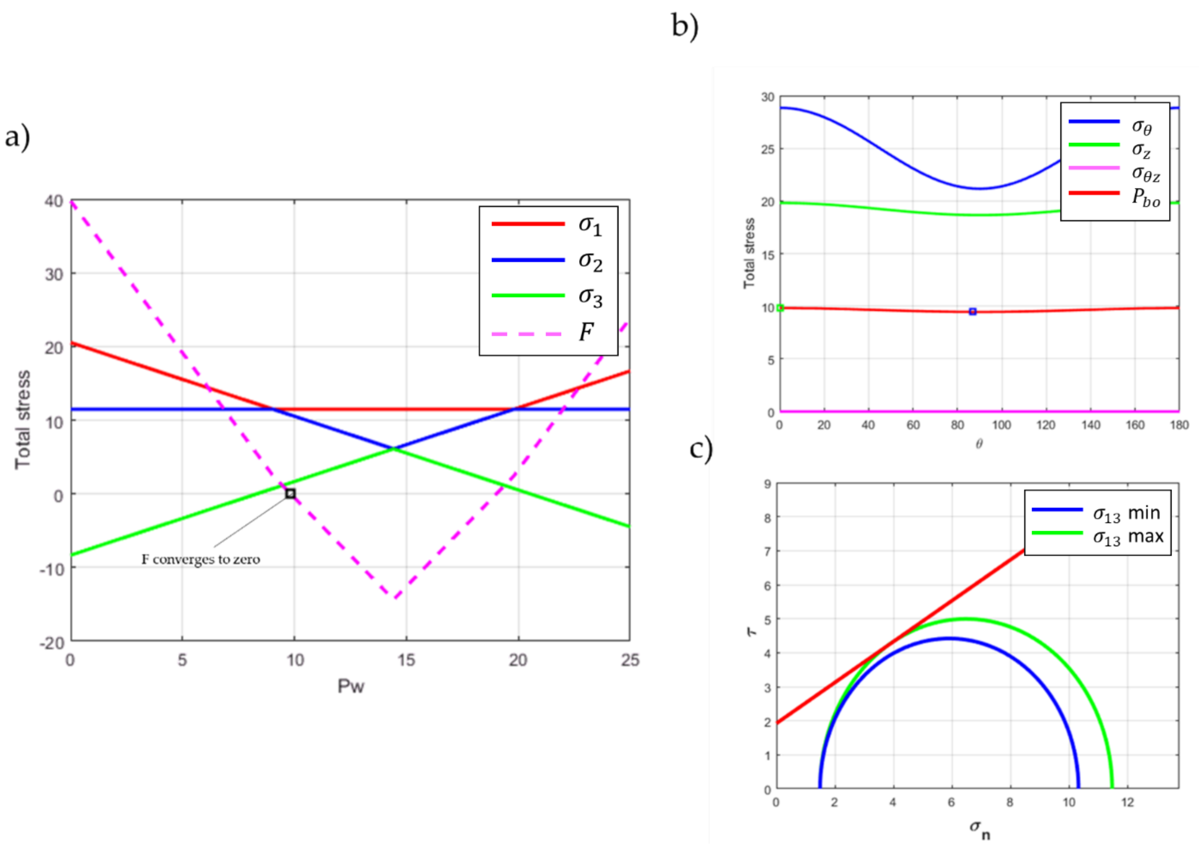


Figure 13. Relationship between circumferential stress ($\sigma_\theta$) with the internal wellbore pressure ($p_w$). (a) The failure function ($F$) crosses zero when the Mohr circle of $\sigma_1$-$\sigma_3$ touches the failure line. (b) The value of $\sigma_3$ at which $F$ crosses zero is taken as the minimum mud pressure to avoid breakout ($p_{bo}$; red curve). (c) The Mohr circle at the wellbore wall at minimum and maximum breakout pressure. The values in these plots are presented in ppg.

### 4.3. Effect of elastic and strength anisotropy on breakout pressure

To demonstrate the importance of incorporating the anisotropic behaviour of the rocks in wellbore stability modelling, in addition to the *in situ* stress configuration and the rock elastic properties listed in Table 2, the following rock strength was also assumed (Table 3).

Table 3. Rock strength properties.

| | Cohesion (psi) | Friction angle (deg) | Bedding orientation | |
|---|---|---|---|---|
| Intact rock | 1462 | 30 | Dip angle ($\beta_{bp}$) (deg) | Dip azimuth ($\alpha_{bp}$) (N-E) |
| Bedding plane | 850 | 18 | 30 | 0 |

For a highly inclined wellbore with $\beta_w = 80°$, the profile of the breakout pressure as a function of the degree of anisotropy ($\eta$) is shown in Figure 14 for several elastic anisotropy ratios. It is obvious that the profile of the breakout pressure as a function of the wellbore inclination using Mohr-Coulomb is less sensitive compared to that of Mogi-Coulomb criterion for a wellbore with an inclination higher than 45°. With Mogi-Coulomb, as the wellbore approaches horizontal, *i.e.* $\beta_w = 90°$, the gap between the lower degree of anisotropy with that of a higher degree of anisotropy widens. For a highly inclined wellbore, as previously illustrated in Figure 12, high elastic anisotropy induces higher near-wellbore stress and, hence, reduces the deviatoric stress around the wellbore wall. In other words, since the near-wellbore stress was calculated using the Lekhnitskii-Amadei solution, the inclusion of the intermediate principal stress in the Mogi-Coulomb criterion seems to be responsible for reducing the breakout pressure by 0.5 ppg, *i.e.* the difference of the normalised breakout pressure of a horizontal wellbore between that with $\eta = 1.1$ and 4.0, in Figure 14.

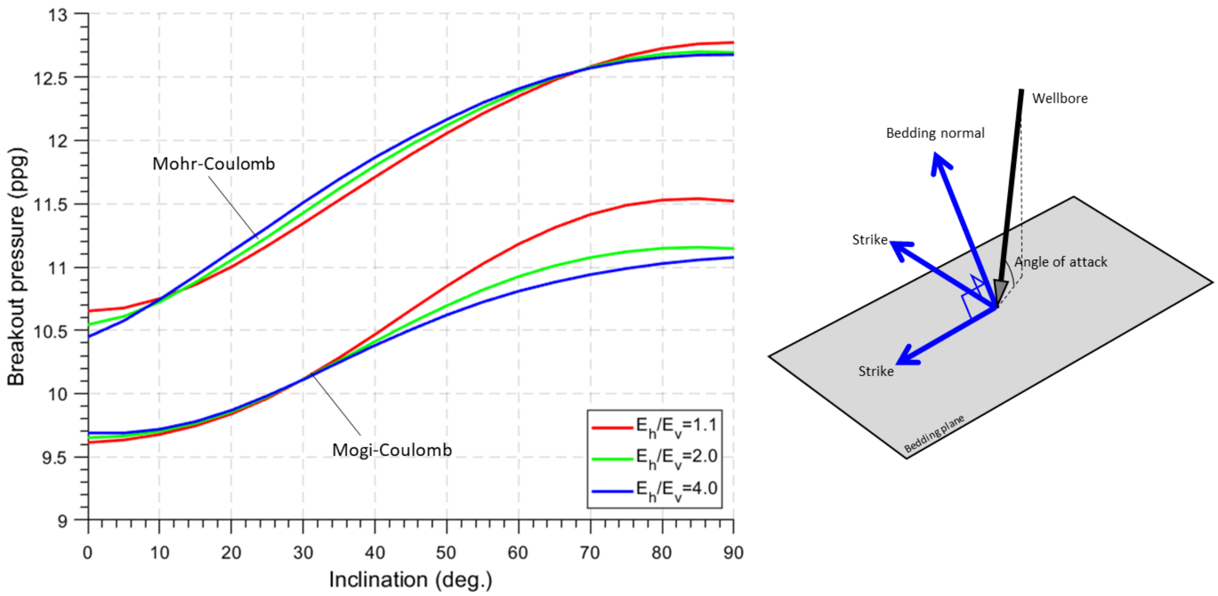


Figure 14. Sensitivity of breakout pressure with wellbore inclination for different degree of anisotropy ($\eta$). The breakout pressure was calculated using Mohr-Coulomb and Mogi-Coulomb and has been normalised with the *in situ* vertical stress. In both cases, the risk of wellbore collapse increases with the increasing wellbore inclination. The schematic of the relative orientation between the wellbore and the bedding plane is shown on the right; please refer to Figures 6 and 7 for the detail definition of the reference frame.

For a given rock characteristic (Table 3), the sensitivity for various bedding orientations and strengths as a function of wellbore inclination is given in Figure 15. When the angle of attack is low, *i.e.* the relative angle between the wellbore axis and the bedding normal, the influence of weak bedding plane diminishes and, when coincide, it vanishes. In practical engineering design, this suggests that wells drilled sub-parallel through a fracture or fault are less stable than those drilled at an oblique angle.

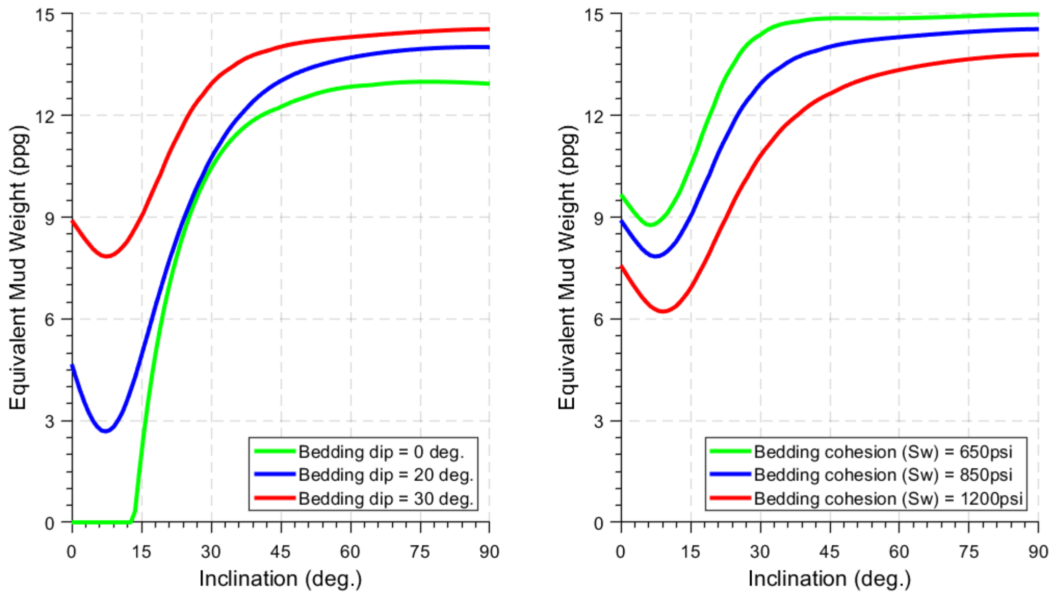


Figure 15. The sensitivity analysis of bedding dip and bedding plane cohesion with breakout pressure.

### 4.4. Sensitivity analysis of breakout pressure

To demonstrate the importance of incorporating elastic anisotropy and rock strength anisotropy in predicting breakout pressure, four individual figures have been generated illustrating the variation of the breakout pressure of an inclined wellbore with $\alpha_w = 130°$ and $\beta_w = 60°$. It is important to note that although the rock properties in Table 2 and Table 3 characterise an anisotropic material, here, for illustration purposes, the Hiramatsu-Oka equation was also used by treating the rock as an elastically isotropic material, apart from the Lekhnitskii-Amadei solution, to calculate the near-wellbore stress. All results are tabulated in Figure 16 and Figure 17. The schematic diagram of the wellbore and the bedding plane orientations follows the illustrations in Figure 6 and Figure 7. The white dot and the white triangle in each figure represent the wellbore and the bedding orientations, respectively. The black curve in the wellbore inclination and azimuth sensitivity plot is the breakout pressure of the intact rocks while the red curve represents that of the bedding plane and the white dot is the assumed mud weight. The overall breakout limit is determined by taking the highest of the two and shaded as a blue area in the sensitivity plot.

When the rock was elastically treated as an isotropic material, *i.e.* the Hiramatsu-Oka solution was deployed, the preferable drilling direction was found to be at around N 120° E using Mohr-Coulomb criterion (Figure 16a). A similar trend is observed when the Mogi-Coulomb true-triaxial failure criterion was used, as shown in Figure 16b; although the general profile of the breakout pressure is different. However, when the elastic anisotropic behaviour of the rock is considered, in which the near-wellbore stress is calculated using the Leknitskii-Amadei solution, the preferable drilling orientation shifts towards around N 160° E (Figure 17).

For intact rock breakout pressure, shown as a black curve in the wellbore inclination and azimuth sensitivity plot, the inclusion of the intermediate stress embedded in the Mogi-Coulomb criterion is responsible for reducing the breakout limit by approximately 1.0 ppg; see for example Figure 16b in which the intact rock breakout is 1.0 ppg less than that of Figure 16a. It is also obvious that not just the overall minimum breakout pressure is changing but the preferable drilling direction, represented by the dark blue area, is also shifted azimuthally.

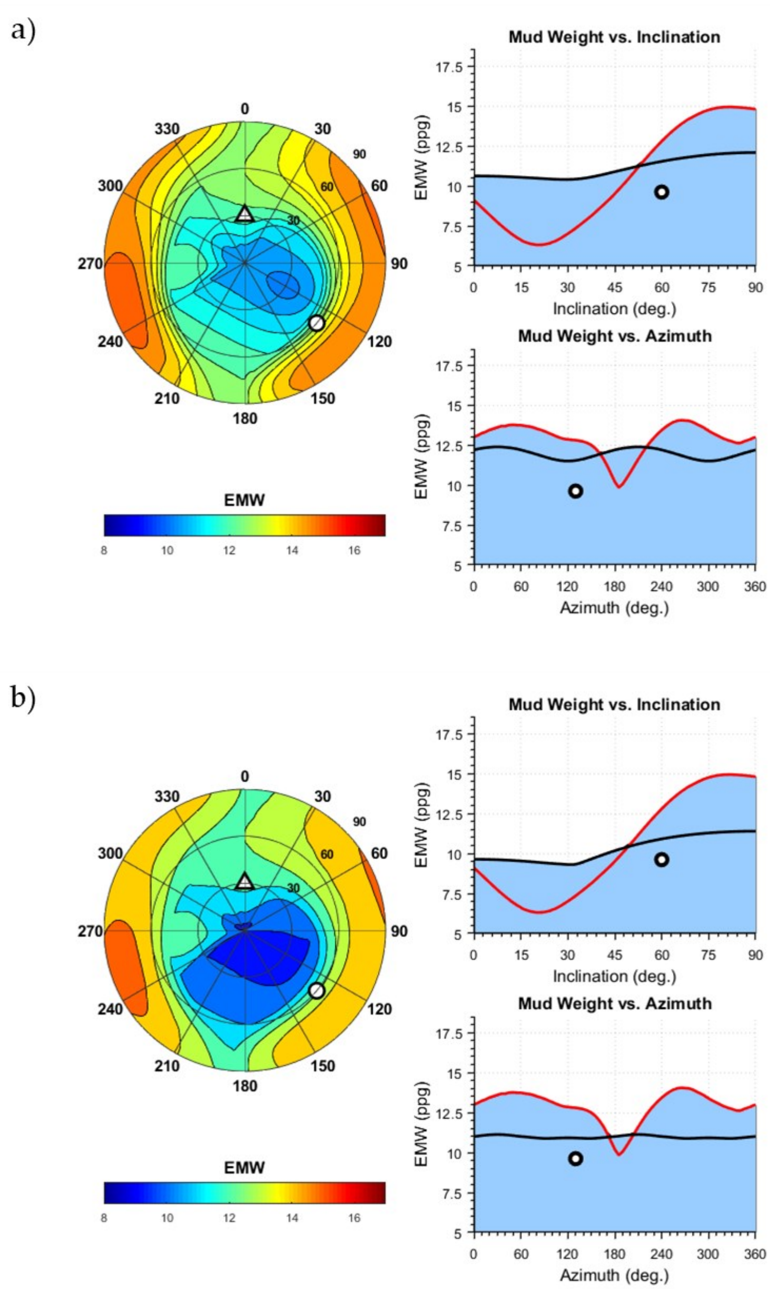


Figure 16. Sensitivity analysis of breakout pressure for an inclined wellbore with $\alpha_w = 130°$ and $\beta_w = 60°$ using Hiramatsu-Oka equation for the near-wellbore stress and (a) Mohr-Coulomb and (b) Mogi-Coulomb failure criteria. The material property used in this case is presented in Table 2 and Table 3.

a)

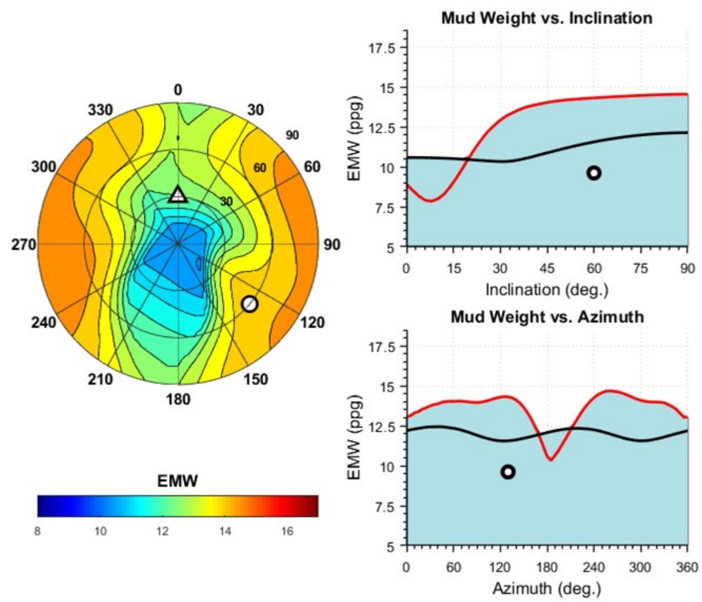


b)

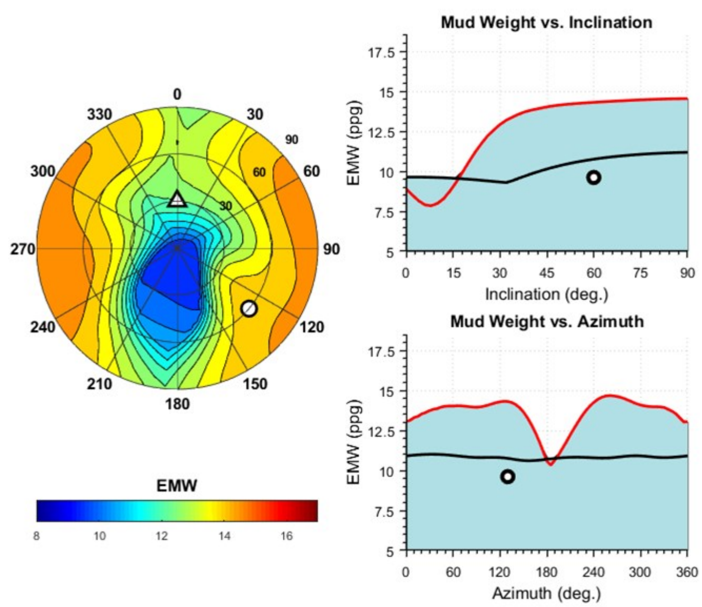


Figure 17. Sensitivity analysis of breakout pressure for an inclined wellbore with $\alpha_w = 130°$ and $\beta_w = 60°$ using Lekhnitskii-Amadei solution for the near-wellbore stress and (a) Mohr-Coulomb and (b) Mogi-Coulomb failure criteria. The material property used in this case is presented in Table 2 and Table 3.

Another interesting observation that can be made from the figures is that the risk posed by the weak bedding plane is masked by the isotropic assumption. For instance, the blue shaded area in Figure 16a is much less than that of Figure 17a, as such the risk posed by the bedding slippage for a wellbore with an inclination between 15° - 50° is not captured when isotropic stress model is used. In contrast, an extra mud weight of approximately 4.5 ppg is necessary to avoid bedding slippage when the anisotropic approach is used (Figure 17). In Figure 16, the wellbore instability could be avoided by increasing the mud weight by at least 2.5 ppg from the current 10.0 ppg, *i.e.* to push the white dot in the sensitivity plots higher than the blue shaded area. However, the anisotropic model shows that at least 14.5 ppg is needed to prevent breakouts. In all cases in Figure 16 and Figure 17, the weak bedding plane governs the breakout limit for the given wellbore orientation.

Figure 18 shows the ratio of the breakout pressure with that of the isotropic model for various degree of elastic anisotropy $E_h/E_v$ and wellbore deviations. The figure can be used to to investigate the sensitivity of the intact rock critical breakout pressure. As shown in Figure 18, when the Mohr-Coulomb criterion is considered, the effect of the elastic anisotropy seems to be negligible for a wellbore with a deviation of less than 40°, for all elastic anisotropy ratios. One can then define a cut-off ratio, *i.e.* a ratio below which anisotropy can be considered as negligible and the rock can be thought as isotropic. For a breakout cut-off ratio of 5%, it can be seen that rock with $E_h/E_v$ of 2.5 will only influence the breakout pressure when the wellbore deviation is higher than 70°. However, according to the Mogi-Coulomb criterion, this 5% cut-off ratio is already observed even for a 60° wellbore deviation. Moreover, anisotropy will affect the breakout pressure for a nearly vertical wellbore with 5-10° deviation angle if $E_h/E_v$ is 2.3 or greater. Thus, it is reasonable to conclude that $E_h/E_v = 2.3$ is the limiting value for which elastic anisotropy should not be neglected in the near-wellbore stress calculation.

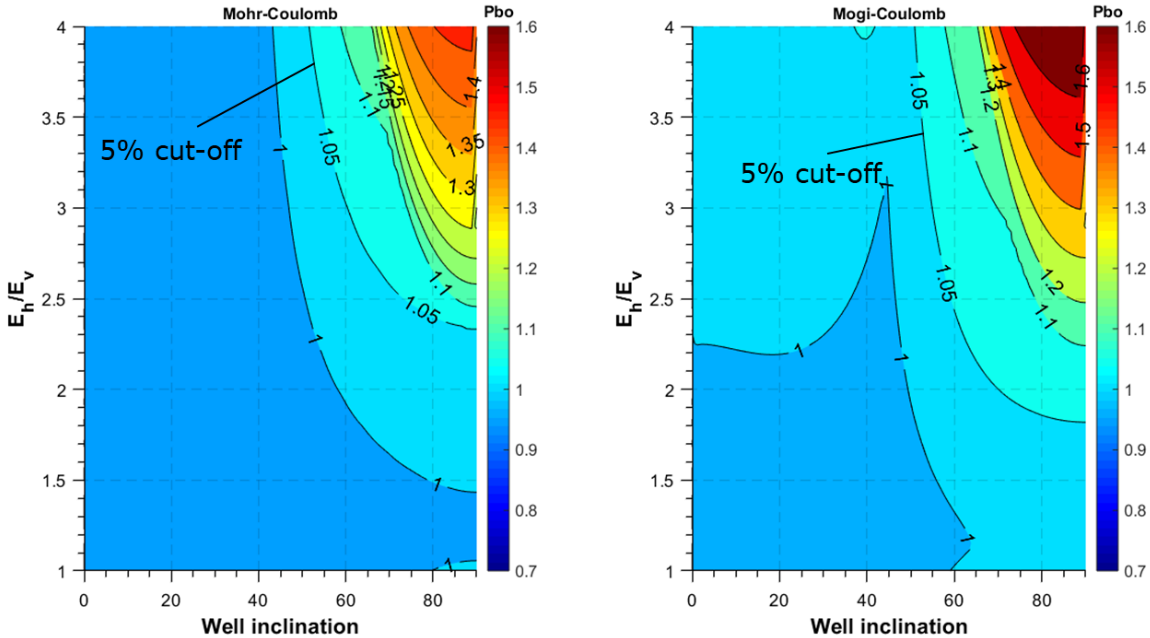


Figure 18. Sensitivity of the intact rock breakout pressure calculated using Mohr-Coulomb (left) and Mogi-Coulomb (right) failure criteria, as functions of the elastic anisotropy ratio ($E_h/E_v$) and wellbore inclination. The breakout pressure has been normalised against the isotropic case.

### 4.5. Sensitivity of critical bedding plane mud weight

To investigate the implications of using the various models described above in wellbore stability analysis, the rock properties as shown in Table 4 and Table 5 are used. Here, the vertical Poisson's ratio ($\nu_v$) characterizes transverse contraction in the plane of isotropy due to the stress acting in the direction normal to the plane, and the horizontal Poisson's ratio ($\nu_h$) corresponds to the transverse contraction in the plane of isotropy due to stress applied also in the plane of isotropy (Lekhnitskii, 1963).

Table 4. Elastic properties chosen for examples.

| | Young's modulus (MPsi) | Poisson's ratio (-) | Shear modulus (MPsi) |
|---|---|---|---|
| Vertical | 2.7 | 0.27 | 1.0 |
| Horizontal | 3.2 | 0.34 | 1.2 |

At a depth of 10,000 ft, the *in situ* stress state is assumed to be in normal fault stress regime, where $\sigma_v > \sigma_H > \sigma_h$, with a considerable horizontal stress magnitude difference. The overburden stress ($\sigma_v$) gradient is taken to be 1.1 psi/ft. The maximum ($\sigma_H$) and minimum ($\sigma_h$) horizontal stresses gradients are 0.87 psi/ft and 0.72 psi/ft, respectively, and the azimuth of $\sigma_h$ is N 0° E, *i.e.,* aligned with the North, and the pore pressure gradient is taken to be 0.44 psi/ft. The mud weight is 10 ppg (0.52 psi/ft). A hypothetical case of an inclined wellbore with an azimuth of N 30°E and inclination of 40° penetrating the TIV rock has been considered. According to Table 5, it is obvious that the wellbore intersects the bedding planes from the cross-dip direction, *i.e.* the wellbore is perpendicular with the bedding dip azimuth.

Table 5. Strength properties chosen for examples.

| | Cohesion (MPsi) | Friction angle (deg) | Bedding orientation | |
|---|---|---|---|---|
| Intact rock | 1.45 | 27 | Dip angle ($\beta_{bp}$) (deg) | Dip azimuth ($\alpha_{bp}$) (N-E) |
| Bedding plane | 0.85 | 18 | 15 | 120 |

To maintain the stability of the bedding plane alone, for a wellbore drilled towards N 30°E, the margin for its inclination is limited up to 15°, measured from vertical. Whereas if the wellbore azimuth is rotated towards the bedding plane up-dip, *i.e.*

N 300°E, the margin widens to up to about 30° as shown in Figure 19. This figure also indicates that the lowest critical bedding plane mud pressure is in the direction perpendicular to the bedding plane, *i.e.* azimuth N 300°E with 15° inclination. This optimum orientation is associated with the lowest shear stress acting on the given bedding plane. The interaction of all factors involved in determining the onset of the bedding plane failure as shown in Figure 19 is complicated that one cannot expect a monotonically increasing trend. This is obvious from the cross-dip case shown in Figure 19 where the slope of the curve becomes less steep at around 45°.

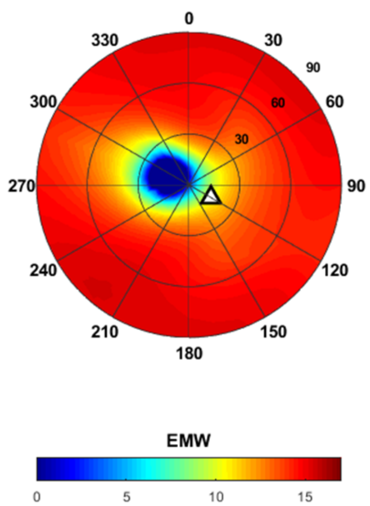


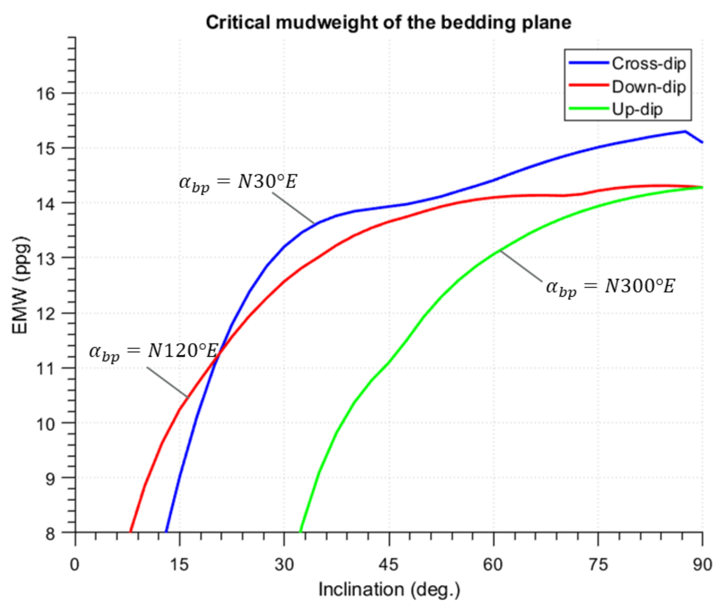


Figure 19. Variation of critical bedding plane mud weight (left) and their sensitivity with wellbore inclination for three drilling azimuths (right). The stress is calculated using Lekhnitskii-Amadei solution.

### 4.6. Wellbore damage prediction and risk quantification

An assessment of the potential instability of a wellbore can also be carried out by evaluating the limit at which the surrounding rocks can withstand the stresses that exist at the wellbore wall. This can be achieved by combining two essential pieces of information: (1) the strength characteristic of the rocks, and (2) the state of stress around the borehole after drilling. In this research, the true-triaxial Mogi-Coulomb failure criterion was chosen, which accounts for the effect of all the three principal stress components. Thus, the Mogi-Coulomb criterion tends to produce a less conservative failure limit as compared to conventional failure criteria, such as Mohr-Coulomb.

Consider the following case: an inclined wellbore with 60° deviation towards N 30° E is assumed to penetrate a TIV rock whose horizontal to vertical Young's modulus ratio is 1.62. The rock is subjected to a vertical *in situ* stress of 10,000 psi, with 8,500 psi and 7,000 psi maximum and minimum horizontal stress, respectively; the pore pressure is assumed to be hydrostatic. The plane of isotropic of the TIV rock is tilted towards N 50° E by 60° with respect to a horizontal plane. While the intact portion of the rock is characterised by cohesion of 1,462 psi and a 30° angle of internal friction, the cohesion of the bedding plane is assumed to be only 360 psi, with 18° friction angle. Two drilling scenarios, using 10.0 ppg and 11.5 ppg mud weight, were simulated to demonstrate the dependency of the potential failure around the wellbore (Figure 20a and b). The irregularity shown by the red curve shown in Figure 20a and b corresponds to the combined effect of breakout initiation failure for the intact rock and bedding plane. As shown, the support provided by the hydrostatic mud pressure to counter the concentrated stress around the hole improves the stability of the wellbore, thus, higher mud weight will correspond to a relatively less damaged wellbore. The potential severity of the hole enlargement can be obtained by computing the area of the region bounded by the red curve and compared them with the ideal wellbore size. For instance, the wellbore would potentially enlarge by 15% of its original area when the drilling is performed using a 9.5 ppg of mud weight, whereas an extra mud weight of 11.0 ppg would reduce the enlargement by 10%. Also, for the case presented here, the 9.5 ppg mud weight is still insufficient to maintain the stability of the bedding plane. Hence, the outline of the potential failure initiation in Figure 20a is governed by both the intact rock and bedding plane; unlike in the case with 11.0 ppg where only the intact rock failure is contributing to the potential failure. Although higher mud weight seems to correspond to a more in-gauge hole, *i.e.*, less damage and lower risk, higher mud weight will have an impact on the reduction of the drilling rate of penetration (ROP), in addition to the risk posed by the initiation of unplanned fractures around the wellbore. Therefore, the result suggests that a strategy to use a lower mud weight can still be recommended if accompanied by an adequate hole cleaning practice to minimise the excessive accumulation of drilling cutting volume. In other words, a sensible balance between the tolerable wellbore damage and the hole cleaning capacity must be achieved. For this purpose, an *a priori* estimate of the potential damage becomes important.

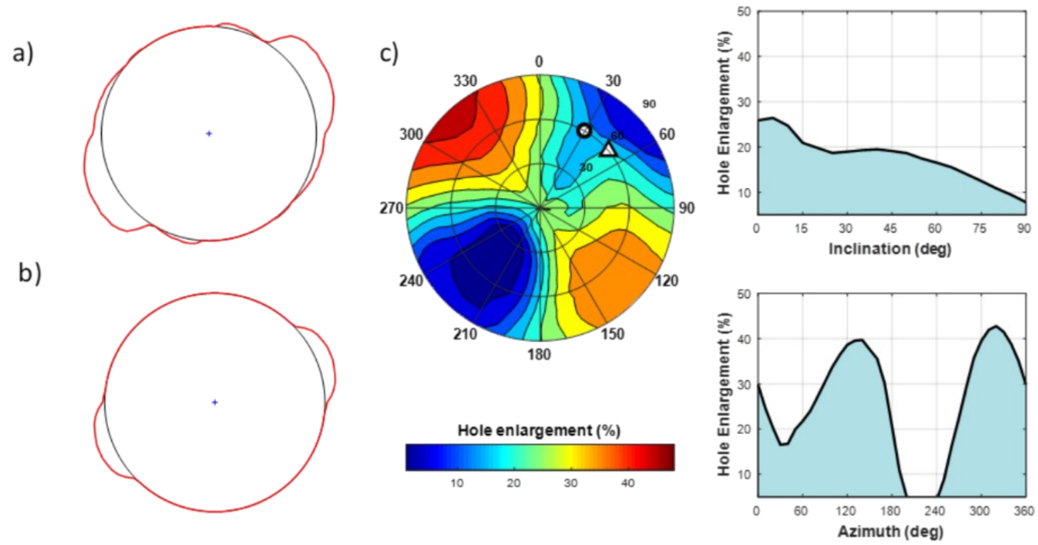


Figure 20. Potential hole enlargement during drilling, using (a) 9.5 ppg and (b) 11.0 ppg mud weight. The hole potentially enlarges by 15% and 5% of its original area for the two cases, respectively. (c) Variation of the potential failure severity around the wellbore for various azimuths and inclinations. The white circle in the polar plot shows the inclination and azimuth of the wellbore, and the white triangle indicates the orientation of the bedding plane.

To further explore the dependency of wellbore damage with drilling direction, consider the case of drilling using 9.5 ppg mud weight with various drilling directions, as illustrated in Figure 20c. The potential failure differs by more than 30° when the drilling azimuth is directed counterclockwise by 90°, *i.e.* towards N 120° E, or about the strike azimuth of the bedding planes. Moreover, for the given drilling azimuth in this example, although the predicted wellbore damage decreases from 15° to a minimum of 8° for a horizontal wellbore, the risk might still be considered high if the drilling operation is not accompanied by an adequate hole cleaning strategy. Thus, this approach can be used to provide complementary information to design an appropriate mitigation plan for a given drilling plan in anisotropic formations.

# Chapter 5 Stress profile of a damaged wellbore

## 5.1. Introduction

In this chapter, a new semi-analytical formulation for two-dimensional in-plane stress computation is proposed. The semi-analytical solution is based on graphical conformal mapping and complex potential methods that can be used to calculate the in-plane stress around an arbitrarily-shaped hole in isotropic or anisotropic materials. The method requires only the outline coordinates of the hole, the elastic moduli of the material, and the magnitude and direction of the far-field stresses. The hole contour, whose outline coordinate is known, is conformally mapped into a unit circle using the successive approximation method proposed by Melentiev (1937). Although Melentiev's method is discussed in some detail in the monograph by Kantorovich & Krylov (1958), there seem to be few if any examples of it being implemented, in the English-language open literature.

The proposed solution is derived by assuming that the material is anisotropic, and the body is subjected to a uniaxial far-field tensional or compressional stress. Using the principle of superposition, the solution can be extended to the more general case of biaxial loading. Moreover, by taking the two roots of the material characteristic equation to be nearly equal, *i.e.* $\mu_1 \approx \mu_2$, the solution can be used for isotropic materials. In this regard, see the discussion given by Gaede *et al*. (2012).

Comparison with several published results for a wide range of possible shapes, such as triangles, squares, ovaloids, and ellipses, has been carried out to validate the method. The method has also been applied to a highly irregular geometry that has been observed in a breakout of a subsurface borehole. As an example of a non-symmetrical and irregular shape, an actual wellbore shape reported by Zoback *et al*. (1985) has been digitised, and the stress around the wellbore wall has been calculated to identify a region with high-stress concentration.

The proposed solution is essentially closed-form, in the sense that it can be explicitly expressed in terms of the mapping coefficients, and parameters that depend only on the elastic moduli of the materials. With such a degree of flexibility, the method will be useful to study the effect of hole geometry on the stress distribution around holes in isotropic or anisotropic materials. In the subsequent sections, the procedure of conformal mapping using the graphical method proposed by Melentiev will be first discussed. Subsequently, the theory of complex stress and displacement potentials will be presented as the basis of the derivation of the proposed semi-analytical solution. Finally, a comparison with several published results will be presented.

## 5.2. Conformal mapping and Melentiev's successive approximation

Conformal mapping can be used to transform a region external to a given hole in the $z$-plane into the region external to the unit circle in the $\xi$-plane. (The mapping can also be done to the interior of the unit circle in the $\xi$-plane. In this research, the mapping will be done from exterior to exterior). Kantorovich & Krylov (1958) provide a detailed discussion of a graphical approach to conformal mapping that was originally developed by Melentiev (1937). Melentiev's method does not seem to have been used in the English-language open literature, although Sobey (1964) used it in a report to the *UK Ministry of Aviation* in 1964. The procedure ensures that the region outside the unit circle is conformally mapped onto a simply connected region outside a hole in the $z$-plane, by an analytic function of the form

$$z = \sum_{k=0}^{\infty} m_k \xi^{1-k} = m_0 \xi + m_1 + m_2 \xi^{-1} + \cdots \tag{78}$$

in which $m_k = \alpha_k + i\beta_k$ are the complex conformal mapping coefficients, and $z = x + iy$. The function in Eq. (78) maps the region outside of the unit circle in the $\xi$-plane into the region outside of the given contour in the $z$-plane.

In practice, the method of Melentiev involves mapping the unit circle in the $\xi$-plane onto the given contour in the $z$-plane. The required calculations, therefore, involve only points on the two contours, and hence many of the subsequent equations in this section are only intended to be valid on the unit circle, $|\xi| = 1$. However, the structure of Eq. (78) guarantees that the mapping will be conformal throughout the regions outside of the two contours. On the circle $|\xi| = 1$, the Fourier series of the real and imaginary parts of $z$ can be written as

$$x = \sum_{k=0}^{\infty} \alpha_k \cos(1-k)\theta - \beta_k \sin(1-k)\theta \tag{79}$$

$$y = \sum_{k=0}^{\infty} \beta_k \cos(1-k)\theta + \alpha_k \sin(1-k)\theta \tag{80}$$

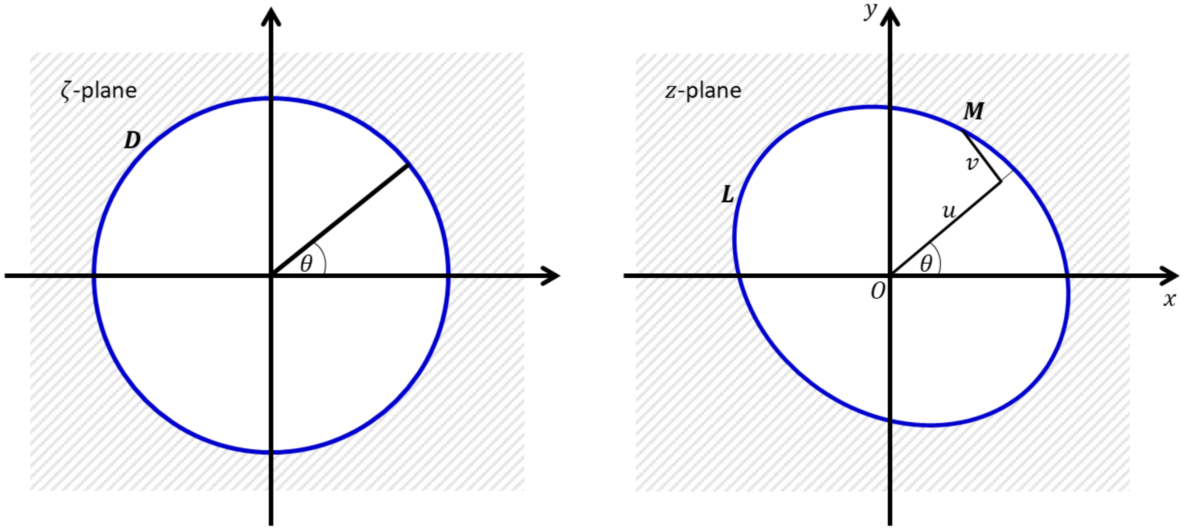


Figure 21. Conformal mapping of the region outside of a unit circle in the $\xi$-plane into the region outside of a given contour in the $z$-plane.

Melentiev suggested working with the ratio $w = z/\xi$, rather than with $z$ itself. This ratio can be written as

$$w = \frac{z}{\xi} = u + iv = \sum_{k=0}^{\infty} m_k \xi^{-k} \tag{81}$$

Hence, the expansion of $u$ and $v$ in a Fourier series can be written as (Kantorovich & Krylov, 1958)

$$u = \sum_{k=0}^{\infty} \alpha_k \cos k\theta + \beta_k \sin k\theta \tag{82}$$

$$v = \sum_{k=0}^{\infty} \beta_k \cos k\theta - \alpha_k \sin k\theta \tag{83}$$

(Note that the notation of $u$ and $v$ in this chapter is not denoting displacement as in Chapter 3.) Since both series contain the same coefficients, it is sufficient to only calculate one of the functions, $u$ or $v$. Subsequent steps will, therefore, be based on Eq. (82). Since in practice the mapping function must be truncated at a finite number of terms, a series containing $(M/2)+1$ terms will be constructed, *i.e.*,

$$z = \sum_{k=0}^{M/2} m_k \xi^{1-k} = m_0 \xi + m_1 + m_2 \xi^{-1} + \cdots + m_{M/2} \xi^{1-(M/2)} \tag{84}$$

which leads to

$$w = \frac{z}{\xi} = \sum_{k=0}^{M/2} m_k \xi^{-k} = m_0 + m_1 \xi^{-1} + m_2 \xi^{-2} + \cdots + m_{M/2} \xi^{-(M/2)} \tag{85}$$

so that *on the contour*, the real part of $w$ takes the form

$$u = \sum_{k=0}^{M/2} \alpha_k \cos k\theta + \beta_k \sin k\theta \tag{86}$$

The total angle $2\pi$ of the circle in the $\xi$-plane is now divided into $M$ equal parts. Sets of rays are constructed from the origin (Figure 22). By allowing the angle $\theta$ to take on the values $2\pi/M$ , $4\pi/M$ , ... ,$2\pi$, the value of $u$ for each ray can be calculated as follows:

$$u_1 = \sum_{k=0}^{M/2} \alpha_k \cos\left(\frac{2\pi k}{M}\right) + \beta_k \sin\left(\frac{2\pi k}{M}\right) \tag{87}$$

$$u_M = \sum_{k=0}^{M/2} \alpha_k \cos(2\pi k) + \beta_k \sin(2\pi k) \tag{88}$$

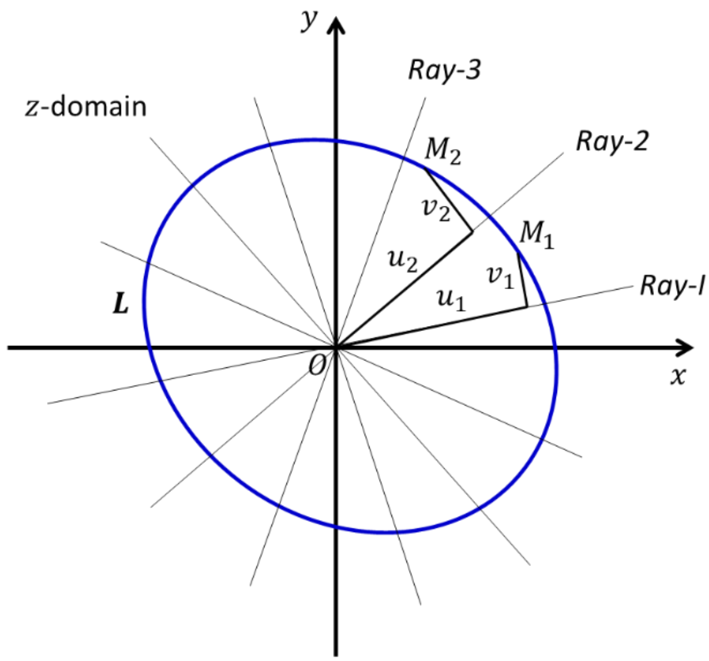


Figure 22. Construction of rays around the shape in the $z$-plane.

This set of equations can be solved for the coefficients $\alpha_k$ and $\beta_k$, as follows (Kantorovich & Krylov, 1958):

$$\alpha_k = \frac{2}{M}\sum_{n=1}^{M} u_n \cos\left(\frac{2\pi nk}{M}\right) \tag{89}$$

$$\alpha_0 = \frac{1}{M}\sum_{n=1}^{M} u_n \tag{90}$$

$$\alpha_{M/2} = \frac{1}{M}\sum_{n=1}^{M}(-1)^n u_n \tag{91}$$

$$\beta_k = \frac{2}{M}\sum_{n=1}^{M} u_n \sin\left(\frac{2\pi nk}{M}\right) \tag{92}$$

$$\beta_0 = -\sum_{n=1}^{M/2} \beta_n \tag{93}$$

Although the final coefficient $\beta_{M/2}$ cannot be computed, for a sufficiently large value of $M$, this coefficient can be taken to be zero (Kantorovich & Krylov, 1958).

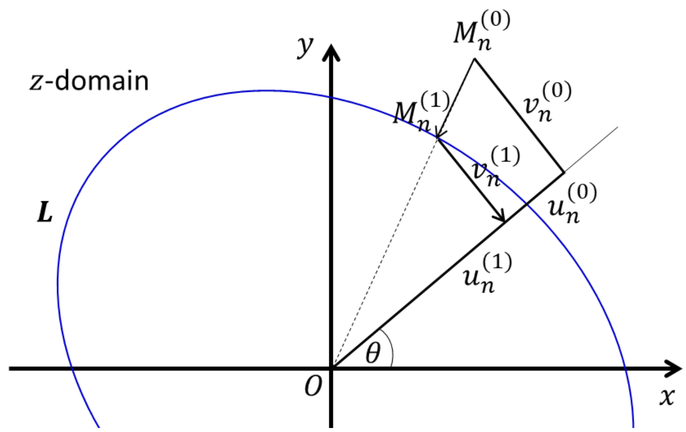


Figure 23. A step in the iterative procedure to transfer point $M_n^{(0)}$ to the contour $L$.

An iterative process is required to determine the most appropriate values of the coefficients $\alpha_k$ and $\beta_k$ such that the approximated contour is as close as possible to the desired contour in the $z$-plane. For instance, assume that some values for $\{u_1, u_2, \dots, u_M\}$ have successfully been determined. The coefficients $\alpha_k$ and $\beta_k$ can then be calculated from the equations given above. The $v_n$ can then be calculated as

$$v_n = \sum_{k=0}^{M/2} \beta_k \cos\left(\frac{2\pi nk}{M}\right) - \alpha_k \sin\left(\frac{2\pi nk}{M}\right) \tag{94}$$

Finally, by using $u_n$ and $v_n$, the points $\{M'_1, M'_2, \dots, M'_M\}$ can be constructed as an approximation to the desired values of $\{M_1, M_2, \dots, M_M\}$ that lie on curve $L$ in the $z$-plane

(Figure 21). However, it will generally not be the case that the initial values of $u_n$, which can be denoted by $\left\{u_1^{(0)}, u_2^{(0)}, \dots, u_M^{(0)}\right\}$, satisfy the desired condition in the first instance, *i.e.* the initial estimated values $\left\{M_1^{(0)}, M_2^{(0)}, \dots, M_M^{(0)}\right\}$ will slightly depart from the desired values $\{M_1, M_2, \dots, M_M\}$.

Melentiev (1937) proposed an iterative method to transfer the value $M'_n$ to be arbitrarily close to the desired position $M_n$. As illustrated in Figure 23, a line is drawn from the point $M_n^{(0)}$ to the origin, and the intersection of this line with the curve $L$ is taken to be the new point $M_n^{(1)}$. The ray $O{-}M_n^{(1)}$ is then projected onto the ray $O{-}u_n^{(0)}$, which defines the new value, $u_n^{(1)}$.

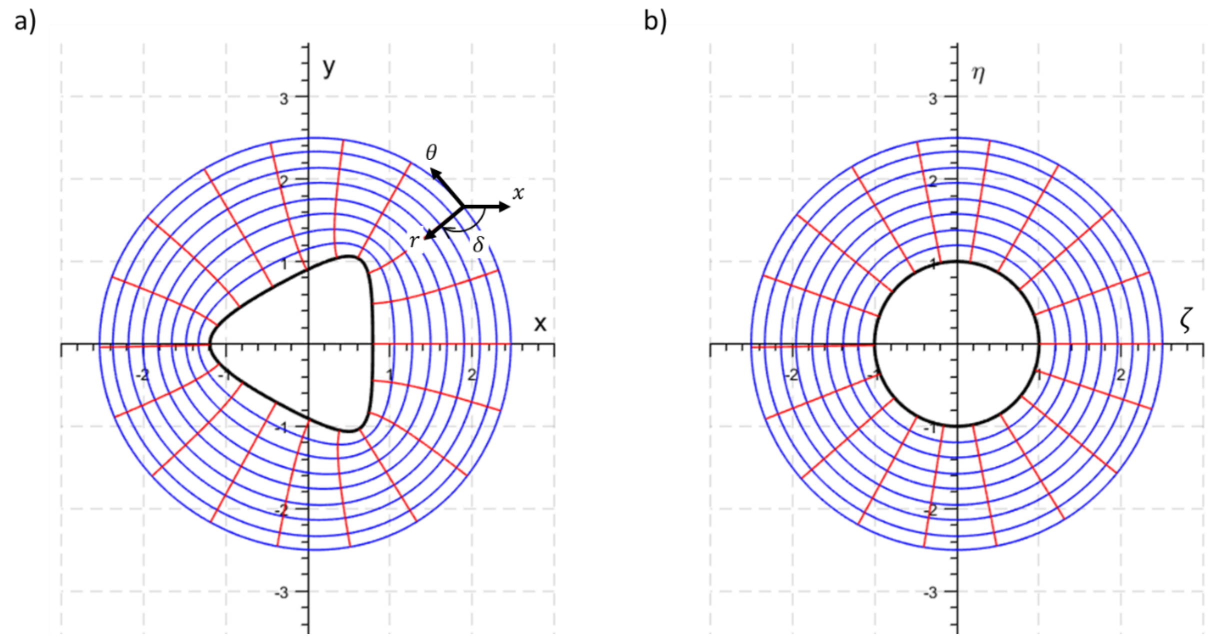


Figure 24. Conformal mapping of the region outside a triangular shape in the $z$-plane into the region outside the unit circle in the $\xi$-plane.

To start the computation, the first approximation, $u_n^{(0)}$, can be taken as

$$u_n^{(0)} = \frac{1}{M}\sum_{k=1}^{M}(x_k + y_k) \tag{95}$$

The $v_n^{(0)}$ values can then be computed from Eq. (94), thereby locating the initial point, $M_n^{(0)}$. The misfit between $M_n^{(0)}$ and the desired value $M_n$ can be quantified as follows:

$$\varepsilon = \frac{1}{M}\sqrt{\sum_{n=1}^{M}\left(u_n^{(i+1)} - u_n^{(i)}\right)^2} \tag{96}$$

Iterations continue until $\varepsilon$ is less than some tolerance, taken here to be $10^{-6}$. Figure 24 shows an example of the region outside a triangle conformally mapped into the region outside the unit circle. The closed curves and quasi-radial lines in the $z$-plane correspond to constant values of the angular and radial coordinates in the $\xi$-plane. The orthogonality of these curves in the $z$-plane shows that the mapping is indeed conformal.

## 5.3. Formulation of two-dimensional elasticity problem in anisotropic rocks

For a plane problem in elasticity, under the plane stress assumptions of $\sigma_{zz} = \sigma_{yz} = \sigma_{xz} = 0$, the generalised Hooke's law as in Eq. (2) can be written as

$$\begin{bmatrix}\varepsilon_{xx}\\ \varepsilon_{yy}\\ \varepsilon_{xy}\end{bmatrix} = \begin{bmatrix}a_{11} & a_{12} & a_{16}\\ a_{12} & a_{22} & a_{26}\\ a_{16} & a_{26} & a_{66}\end{bmatrix}\begin{bmatrix}\sigma_{xx}\\ \sigma_{yy}\\ \sigma_{xy}\end{bmatrix} \tag{97}$$

where the $\{a_{ij}\}$ are the elastic compliances of the material. The first two of the equilibrium equations as in Eq. (23) become:

$$\frac{\partial\sigma_x}{\partial x} + \frac{\partial\tau_{xy}}{\partial y} + X = 0 \quad \text{and} \quad \frac{\partial\tau_{xy}}{\partial x} + \frac{\partial\sigma_y}{\partial y} + Y = 0 \tag{98}$$

and the third equation becomes $Z = 0$, and the stress component on the long axis $OZ$ will also become zero. For a plane problem, the only non-trivial compatibility relation Eq. (27) is

$$\frac{\partial^2 \varepsilon_{xx}}{\partial y^2} + \frac{\partial^2 \varepsilon_{yy}}{\partial x^2} = \frac{\partial^2 \gamma_{xy}}{\partial x \partial y} \tag{99}$$

The equilibrium equations (99) may be satisfied if the Airy stress function is introduced. The stress components can be written in terms of the Airy stress function $U(x, y)$, as follows:

$$\sigma_{xx} = \frac{\partial^2 U}{\partial y^2}; \quad \sigma_{yy} = \frac{\partial^2 U}{\partial x^2}\ ; \quad \sigma_{xy} = -\frac{\partial^2 U}{\partial x \partial y} \tag{100}$$

If the constitutive equation is inserted into the compatibility relation, the following governing fourth-order partial differential equation is obtained:

$$a_{22}\frac{\partial^4 U}{\partial x^4} - 2a_{26}\frac{\partial^4 U}{\partial x^3 \partial y} + (2a_{12} + a_{66})\frac{\partial^4 U}{\partial x^2 \partial y^2} - 2a_{16}\frac{\partial^4 U}{\partial x \partial y^3} + a_{11}\frac{\partial^4 U}{\partial y^4} = 0 \tag{101}$$

The solution to this *partial differential equation* (PDE) depends on following characteristic equation,

$$a_{11}\mu^4 - 2a_{16}\mu^3 + (2a_{12} + a_{66})\mu^2 - 2a_{26}\mu + a_{22} = 0 \tag{102}$$

the four roots of which can be written as

$$\mu_1 = \gamma_1 + i\delta_1, \quad \bar{\mu}_1 = \gamma_1 - i\delta_1, \quad \mu_2 = \gamma_2 + i\delta_2, \quad \bar{\mu}_2 = \gamma_2 - i\delta_2 \tag{103}$$

The roots of the characteristic equation (102) depend on the material's elastic moduli through $\{a_{ij}\}$, *i.e.* the elastic compliances of the material. According to Lekhnitskii (1968), three cases are possible: the roots may be complex and different, they may be complex and equal, or they may be different and purely imaginary. Some specific examples are given by Lekhnitskii (1968), who points out that the case of purely real roots can be ruled out by energy considerations. Finally, note that to apply this formalism to the problem of plane strain, it is merely necessary to replace $\{a_{ij}\}$ in the characteristic equation with $c_{ij} = a_{ij} - a_{i3}a_{3j}/a_{33}$.

The general solution for the Airy stress function $U(x, y)$ can be written in terms of two complex potentials, $F_1(z_1)$ and $F_2(z_2)$,

$$U(x, y) = F_1(z_1) + F_2(z_2) + \overline{F_1(z_1)} + \overline{F_2(z_2)} = 2Re[F_1(z_1) + F_2(z_2)] \tag{104}$$

where $z_j = x + \mu_j y$ and $Re[F(z)]$ takes only the real component of the function $F(z)$. Two new complex potentials that are the derivatives of the original pair are now defined as

$$\phi(z_1) = F_1'(z_1) \qquad \text{and} \qquad \psi(z_2) = F_2'(z_2) \tag{105}$$

Thus, if we substitute the definition of the general solution Eq. (104) into Eq. (100) and take into consideration definition Eq. (105), the expression of the stress components through the two complex functions $\phi(z_1)$ and $\psi(z_2)$ can be obtained:

$$\sigma_{xx} = \frac{\partial^2 U}{\partial y^2} = 2Re[\mu_1^2 \phi'(z_1) + \mu_2^2 \psi'(z_2)] \tag{106}$$

$$\sigma_{yy} = \frac{\partial^2 U}{\partial x^2} = 2Re[\phi'(z_1) + \psi'(z_2)] \tag{107}$$

$$\sigma_{xy} = -\frac{\partial^2 U}{\partial x \partial y} = -2Re[\mu_1 \phi'(z_1) + \mu_2 \psi'(z_2)] \tag{108}$$

In addition to the basic characteristic equation (102), the Airy stress function $U(x, y)$ should also satisfy the boundary condition

$$\sigma_{xx} \cos(n, x) + \sigma_{xy} \cos(n, y) = X_n \tag{109}$$

$$\sigma_{xy} \cos(n, x) + \sigma_{yy} \cos(n, y) = Y_n \tag{110}$$

where $X_n$ and $Y_n$ are the traction components acting on the hole contour. If the boundary condition is expressed in terms of the Airy stress function $U(x, y)$ and if the term $\cos(n, x)$ and $\cos(n, y)$ is expressed in terms of the arc length $S$ of the hole contour (Savin, 1961):

$$\cos(n, x) = \frac{dy}{dS} \qquad \text{and} \qquad \cos(n, y) = -\frac{dx}{dS}$$

then, the boundary condition can be written as

$$\frac{\partial^2 U}{\partial y^2}\frac{dy}{dS} + \frac{\partial^2 U}{\partial x \partial y}\frac{dx}{dS} = \frac{d}{dS}\left(\frac{\partial U}{\partial y}\right) = X_n$$

$$-\frac{\partial^2 U}{\partial x \partial y}\frac{dy}{dS} - \frac{\partial^2 U}{\partial x^2}\frac{dx}{dS} = -\frac{d}{dS}\left(\frac{\partial U}{\partial x}\right) = Y_n$$

By integrating the above equations with respect to the arc length of the hole contour $S$, the boundary condition expressed in terms of the stress function $U(x, y)$ can be obtained (Savin, 1961)

$$\frac{\partial U}{\partial x} = -\int_0^S Y_n \, ds + C_1 \quad \text{and} \quad \frac{\partial U}{\partial y} = -\int_0^S X_n \, ds + C_2 \tag{111}$$

where $C_1$ and $C_2$ are arbitrary real constants. If we substitute the definition in Eqs. (104) and (111), the final expressions of the boundary condition as a function of the two complex functions $\phi(z_1)$ and $\psi(z_2)$ can be obtained. These are,

$$2Re[\phi(z_1) + \psi(z_2)] = -\int_0^s Y_n \, ds + C_1 \equiv f_1 \tag{112}$$

$$2Re[\mu_1\phi(z_1) + \mu_2\psi(z_2)] = -\int_0^s X_n \, ds + C_2 \equiv f_2 \tag{113}$$

where $S$ is a point on the contour, and the $C_i$ are constants of integration. The above definitions are required in the derivation of the new formulation for the stress computation around an arbitrary hole shape that will be detailed in the next section. Thus, for the plane problem, the solution for the stress components reduces to the determination of the two complex potentials $\phi(z_1)$ and $\psi(z_2)$.

## 5.4. New formulation for two-dimensional problem of an arbitrary hole shape

To find the stresses around an arbitrarily-shaped hole in a medium subject to a given far-field stress, the two stress potentials defined in Eq. (105) need to be found. First, recall the mapping function given by Eq. (78), truncated to $N$ terms:

$$z = \omega(\xi) = \sum_{k=0}^{N} m_k \xi^{1-k} \tag{114}$$

The auxiliary variables $z_1$ and $z_2$ are related to $z$ by (Lu *et al.*, 2015, Savin, 1961, Ukadgaonker & Rao, 2000)

$$z_1 = x + \mu_1 y = \frac{(1 - i\mu_1)}{2} z + \frac{(1 + i\mu_1)}{2} \bar{z} \tag{115}$$

and similarly for $z_2$. Substituting Eq. (115) into (114) yields, for $j = 1$ or 2,

$$z_j = \frac{1}{2} \sum_{k=0}^{N} (1 - i\mu_j)\alpha_k \, \xi^{1-k} + (1 + i\mu_j)\alpha_k \bar{\xi}^{1-k} + (i + \mu_j)\beta_k \xi^{1-k} \\ + (\mu_j - i)\beta_k \bar{\xi}^{1-k} \tag{116}$$

On the unit circle, where $\xi = e^{i\theta}$ and $\bar{\xi} = e^{-i\theta} = 1/\xi$, these relations take the form

$$z_j = \frac{1}{2} \sum_{k=0}^{N} (1 - i\mu_j)\alpha_k \, \xi^{1-k} + (1 + i\mu_j)\alpha_k \xi^{-(1-k)} + (i + \mu_j)\beta_k \xi^{1-k} \\ + (\mu_j - i)\beta_k \xi^{-(1-k)} \tag{117}$$

Now, recall the boundary conditions Eqs. (112) and (113). The focus of the present method is on the problem of a traction-free hole in an infinite body, subjected to a far-field state of uniform stress. In this case, $X_n = Y_n = 0$. Moreover, although the $C_i$ will influence the displacements, they have no effect on the stresses, and so for the present purposes, they can be set to 0. Consequently, $f_1 = f_2 = 0$ in the boundary conditions Eqs. (112) and (113). In this case, the two potentials take the following general form (Savin, 1961)

$$\phi(z_1) = B^* z_1 + \phi_0(z_1) \qquad \text{and} \qquad \psi(z_2) = (B'^* + iC'^*)z_2 + \psi_0(z_2) \tag{118}$$

where the potentials having subscript 0 are analytical functions outside of the hole, and the constants can be expressed in terms of the far-field stresses, as follows (Savin, 1961):

$$B^* = \frac{\sigma_{xx}^{\infty} + (\gamma_2^2 + \delta_2^2)\sigma_{yy}^{\infty} + 2\gamma_2\sigma_{xy}^{\infty}}{2[(\gamma_2 - \gamma_1)^2 + (\delta_2^2 - \delta_1^2)]} \tag{119}$$

$$B'^* = \frac{(\gamma_1^2 - \delta_1^2 - 2\gamma_1\gamma_2)\sigma_{yy}^{\infty} - \sigma_{xx}^{\infty} - 2\gamma_2\sigma_{xy}^{\infty}}{2[(\gamma_2 - \gamma_1)^2 + (\delta_2^2 - \delta_1^2)]} \tag{120}$$

$$C'^* = \frac{(\gamma_2 - \gamma_1)\sigma_{xx}^{\infty} + [\gamma_2(\gamma_1^2 + \delta_1^2) - \gamma_1(\gamma_2^2 + \delta_2^2)]\sigma_{yy}^{\infty} + [(\gamma_1^2 + \delta_1^2) - (\gamma_2^2 + \delta_2^2)]\sigma_{xy}^{\infty}}{2\delta_2[(\gamma_2 - \gamma_1)^2 + (\delta_2^2 - \delta_1^2)]} \tag{121}$$

where $\sigma_{xx}^{\infty}$, $\sigma_{yy}^{\infty}$ and $\sigma_{xy}^{\infty}$ are the *in situ* stress, and $\gamma_i$ and $\delta_i$ are related to the material elastic property as described in Eq. (103).

Substitution of Eq. (118) into Eqs. (112) and (113) shows that the 0-subscripted potentials must satisfy the following boundary conditions (Savin, 1961):

$$2Re[\phi_0(z_1) + \psi_0(z_2)] = -2Re[B^* z_1 + (B'^* + iC'^*)z_2] \equiv f_1^0 \tag{122}$$

$$2Re[\mu_1\phi_0(z_1) + \mu_2\psi_0(z_2)] = -2Re[\mu_1 B^* z_1 + \mu_2(B'^* + iC'^*)z_2] \equiv f_2^0 \tag{123}$$

Now, by combining Eqs. (117) and (122), the first boundary function $f_1^0$ can be expressed, on the hole contour, as

$$f_1^0 = -\frac{1}{2}\left[\begin{array}{l} (K_1 + \bar{K}_2)\sum_{k=0}^{N} \alpha_k \, \xi^{1-k} + (\bar{K}_1 + K_2)\sum_{k=0}^{N} \alpha_k \, \xi^{-(1-k)} \\ +(K_3 + \bar{K}_4)\sum_{k=0}^{N} \beta_k \xi^{1-k} + (\bar{K}_3 + K_4)\sum_{k=0}^{N} \beta_k \, \xi^{-(1-k)} \end{array}\right] \tag{124}$$

in which the constants $K_i$ are defined by

$$K_1 = B^*(1 - i\mu_1) + (B'^* + iC'^*)(1 - i\mu_2) \tag{125}$$

$$K_2 = B^*(1 + i\mu_1) + (B'^* + iC'^*)(1 + i\mu_2) \tag{126}$$

$$K_3 = B^*(\mu_1 + i) + (B'^* + iC'^*)(\mu_2 + i) \tag{127}$$

$$K_4 = B^*(\mu_1 - i) + (B'^* + iC'^*)(\mu_2 - i) \tag{128}$$

Following the same process, the second boundary function Eq. (123) can be expressed, on the hole contour, as

$$f_2^0 = -\frac{1}{2}\left[\begin{array}{l} (K_5 + \bar{K}_6)\sum_{k=0}^{N} \alpha_k \, \xi^{1-k} + (\bar{K}_5 + K_6)\sum_{k=0}^{N} \alpha_k \, \xi^{-(1-k)} \\ +(K_7 + \bar{K}_8)\sum_{k=0}^{N} \beta_k \xi^{1-k} + (\bar{K}_7 + K_8)\sum_{k=0}^{N} \beta_k \, \xi^{-(1-k)} \end{array}\right] \tag{129}$$

in which the constants $K_i$ are defined by

$$K_5 = \mu_1 B^*(1 - i\mu_1) + \mu_2(B'^* + iC'^*)(1 - i\mu_2) \tag{130}$$

$$K_6 = \mu_1 B^*(1 + i\mu_1) + \mu_2(B'^* + iC'^*)(1 + i\mu_2) \tag{131}$$

$$K_7 = \mu_1 B^*(\mu_1 + i) + \mu_2(B'^* + iC'^*)(\mu_2 + i) \tag{132}$$

$$K_8 = \mu_1 B^*(\mu_1 - i) + \mu_2(B'^* + iC'^*)(\mu_2 - i) \tag{133}$$

It can be verified that, on the unit circle, both expressions (124) and (129) are purely real, as required by Eqs. (122) and (123).

Since $z_1$and $z_2$ are each known functions of $\xi$, the two 0-subscripted potentials, which can now be denoted as $\phi_0(\xi)$ and $\psi_0(\xi)$, can be found by contour integration, as explained on p.155 of Savin (1961), modified to account for the fact that in the current formulation, the mapping is made from the region outside the unit circle, rather than inside the unit circle:

$$\phi_0(\xi) = \frac{-i}{4\pi(\mu_1 - \mu_2)} \int_{\gamma} (\mu_2 f_1^0 - f_2^0) \frac{t+\xi}{t-\xi} \frac{dt}{t} + \lambda_1 \tag{134}$$

$$\psi_0(\xi) = \frac{i}{4\pi(\mu_1 - \mu_2)} \int_{\gamma} (\mu_1 f_1^0 - f_2^0) \frac{t+\xi}{t-\xi} \frac{dt}{t} + \lambda_1 \tag{135}$$

where $\gamma$ is the unit circle in the $\xi$-plane, and the $\lambda_i$ are constants whose values are known, but which will be ignored here, as they have no influence on the stresses. In the present formulation, the exterior of the unit circle in the $\xi$-plane has been mapped into the region outside of the physical hole (see Figure 21). Note that Savin (1961) considered a situation in which the *interior* of the unit circle in the $\xi$-plane is mapped into the region outside of the physical hole. The connection between the two situations is discussed by Muskhelishvili (1953), p.268. The two approaches are essentially identical, since one can imagine a two-stage mapping in which the first stage is an inversion, $\xi = 1/s$, that first maps the interior of the unit circle into its exterior. This would merely change the signs of the power exponents in the mapping function given by Eq. (78), but would not change the numerical values of the mapping coefficients.

In light of Eqs. (124) and (129), the parenthesised terms in Eqs. (134) and (135) are series that involve terms of the form $t^n$, for non-zero integer values of $n$. Since the relevant values of $\xi$ lie outside the unit circle, the integrals have the following values (England, 2003):

$$\int_{\gamma} t^n \cdot \frac{t+\xi}{t-\xi}\frac{\mathrm{d}t}{t} = 0, \qquad \int_{\gamma} \frac{1}{t^n} \cdot \frac{t+\xi}{t-\xi}\frac{\mathrm{d}t}{t} = -4\pi i \xi^{-n} \tag{136}$$

in which $n$ is taken to be a positive integer, and a constant term on the right side of each integral has been ignored, as they do not contribute to the stresses. Note also that the $m_1$ term in the mapping function (78), which would contribute terms in the integrand having $k-1=n=0$, represents a rigid-body translation of the hole contour, and therefore has no influence on the boundary stresses. Non-zero values of $m_1$ that may be generated by the Melentiev iterative mapping procedure can, therefore, be set to zero, when computing the stresses. Hence, there is no need to consider the case $n=0$ in Eq. (136).

Substituting $f_1^0$ and $f_2^0$ from Eqs. (124) and (129) into expressions (134) and (135), and making use of the integrals in Eq. (136), leads to the following expressions for the two potentials:

$$\phi_0(\xi) = A_1\alpha_0\xi^{-1} + A_2\beta_0\xi^{-1} + A_3\sum_{k=2}^{N}\alpha_k\,\xi^{1-k} + A_4\sum_{k=2}^{N}\beta_k\,\xi^{1-k} \tag{137}$$

$$\psi_0(\xi) = A_5\alpha_0\xi^{-1} + A_6\beta_0\xi^{-1} + A_7\sum_{k=2}^{N}\alpha_k\,\xi^{1-k} + A_8\sum_{k=2}^{N}\beta_k\,\xi^{1-k} \tag{138}$$

in which the constants $A_i$ are given by

$$A_1 = \frac{1}{2(\mu_1-\mu_2)}\left[\mu_2(\bar{K}_1+K_2)-(\bar{K}_5+K_6)\right] \tag{139}$$

$$A_2 = \frac{1}{2(\mu_1-\mu_2)}\left[\mu_2(\bar{K}_3+K_4)-(\bar{K}_7+K_8)\right] \tag{140}$$

$$A_3 = \frac{1}{2(\mu_1 - \mu_2)}[\mu_2(K_1 + \bar{K}_2) - (K_5 + \bar{K}_6)] \tag{141}$$

$$A_4 = \frac{1}{2(\mu_1 - \mu_2)}[\mu_2(K_3 + \bar{K}_4) - (K_7 + \bar{K}_8)] \tag{142}$$

$$A_5 = \frac{-1}{2(\mu_1 - \mu_2)}[\mu_1(\bar{K}_1 + K_2) - (\bar{K}_5 + K_6)] \tag{143}$$

$$A_6 = \frac{-1}{2(\mu_1 - \mu_2)}[\mu_1(\bar{K}_3 + K_4) - (\bar{K}_7 + K_8)] \tag{144}$$

$$A_7 = \frac{-1}{2(\mu_1 - \mu_2)}[\mu_1(K_1 + \bar{K}_2) - (K_5 + \bar{K}_6)] \tag{145}$$

$$A_8 = \frac{-1}{2(\mu_1 - \mu_2)}[\mu_1(K_3 + \bar{K}_4) - (K_7 + \bar{K}_8)] \tag{146}$$

The stress components can now be calculated as

$$\sigma_{xx} = \sigma_{xx}^{\infty} + 2Re\left[\mu_1^2 \phi'_0(z_1) + \mu_2^2 \psi'_0(z_2)\right] \tag{147}$$

$$\sigma_{yy} = \sigma_{yy}^{\infty} + 2Re\left[\phi'_0(z_1) + \psi'_0(z_2)\right] \tag{148}$$

$$\sigma_{xy} = \sigma_{xy}^{\infty} - 2Re[\mu_1 \phi'_0(z_1) + \mu_2 \psi'_0(z_2)] \tag{149}$$

in which the derivatives of the potentials can be computed using the chain rule, as follows:

$$\phi'_0(z_1) = \frac{d\phi_0(\xi)}{d\xi}\frac{d\xi}{dz_1} = \frac{\phi'_0(\xi)}{\omega'_1(\xi)} \tag{150}$$

$$\psi'_0(z_2) = \frac{d\psi_0(\xi)}{d\xi}\frac{d\xi}{dz_2} = \frac{\psi'_0(\xi)}{\omega'_2(\xi)} \tag{151}$$

The tangential and radial stress components can be calculated using the following transformation (Jaeger *et al.*, 2007):

$$\sigma_{\theta\theta} - \sigma_{rr} + 2\sigma_{r\theta} = \left(\sigma_{xx} - \sigma_{yy} + 2\sigma_{xy}\right)e^{2i\delta} \tag{152}$$

$$\sigma_{\theta\theta} + \sigma_{rr} = \sigma_{xx} + \sigma_{yy} \tag{153}$$

where $\delta$ is the rotational angle from the $x$-axis to the radial axis $r$ (see Figure 24). For biaxial tension or compression, the principle of superposition can be used.

## 5.5. Calculation and validation with known results

The general workflow of the proposed method is as follows. The hole contour, whose outline coordinates are known in the $z$-plane, is conformally mapped into the outside of the unit circle using Melentiev's successive approximation method, to obtain the mapping coefficients, $m_k$. The characteristic equation (102) is then solved for the characteristic roots, after which the $B$ and $C$ constants appearing in the stress potentials can be computed from knowledge of these roots and the far-field stresses, using Eqs. (119) to (121). The potentials are then given by Eqs. (137) and (138), and the derivatives of the two potentials are calculated using Eqs. (150) and (151). The stress components can then be calculated using Eqs. (147) and (149), and can be converted into polar coordinates using Eqs. (152) and (153).

To demonstrate the robustness of this method, the following section provides validation by comparing the stress obtained with the proposed method against several known formulations and published results. The validation covers a wide range of possible shapes, such as ellipses, triangles, squares, ovaloids, *etc.*, in both isotropic and anisotropic plates.

### *5.5.1. Elliptical hole*

For an elliptical hole in an isotropic medium, Jaeger *et al*. (2007) showed that the stress concentration around the hole contour is given by the following equation:

$$\sigma_\theta = \sigma^\infty \left[\frac{2ab + (a^2 - b^2)\cos 2\alpha - (a+b)^2 \cos 2(\alpha - \chi)}{(a^2 + b^2) - (a^2 - b^2)\cos 2\chi}\right] \tag{154}$$

in which $\alpha$ denotes the angle between the direction of the far-field stress $\sigma^\infty$ with the $x$-axis, and $a$ and $b$ are the lengths of the ellipse's axes in the $x$ and $y$ directions, respectively. Figure 25 shows ellipses with $a/b = 3/2$ and $a/b = 2/3$. The elliptical coordinate $\chi$ is related to the polar coordinate $\theta$ by $\tan\chi/\tan\theta = a/b$ (England, 2003).

Savin (1961) gave the following alternative expression for the hoop stress in this problem:

$$\sigma_\theta = \sigma^\infty \left[\frac{(1+k)^2 \sin^2(\theta + \alpha) - \sin^2\alpha - k^2\cos^2\alpha}{\sin^2\theta + k^2\cos^2\theta}\right] \tag{155}$$

in which $k = b/a$.

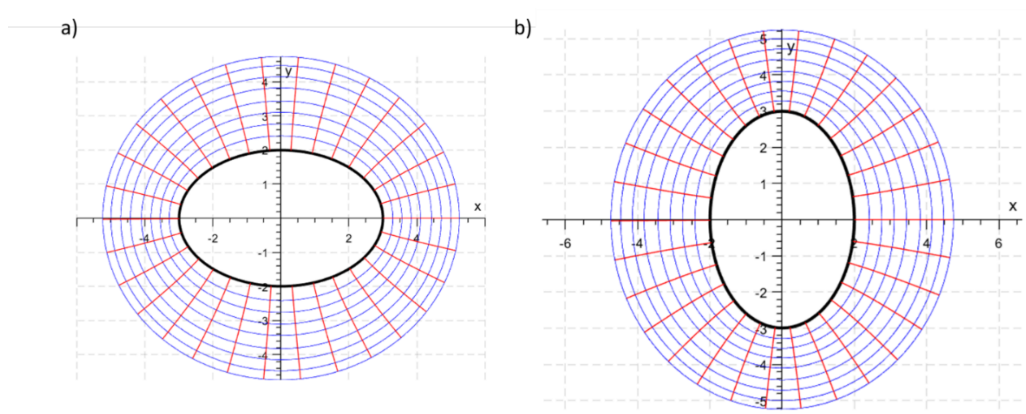


Figure 25. Elliptical holes with (a) $a/b = 3/2$ and (b) $a/b = 2/3$, showing the mapped curves that correspond to the lines of constant $r$ and constant $\theta$ in the $\xi$-plane.

The conformal mapping constants for an ellipse with $a/b = 3/2$ that are obtained using Melentiev's method, with seven terms in the mapping function, are $m_0 = 0.9976$, $m_1 = 0.0017$, $m_2 = 1.999$, $m_3 = 0.0002$ and $m_4 = m_5 = m_6 = 0.0001$. The hoop stresses that are computed with the present method are compared in Figure 26 to those given by the analytical expressions (154) and (155), for three different orientations of the far-field stress. The agreement is extremely good, for all angles around the ellipse, and all three loading cases.

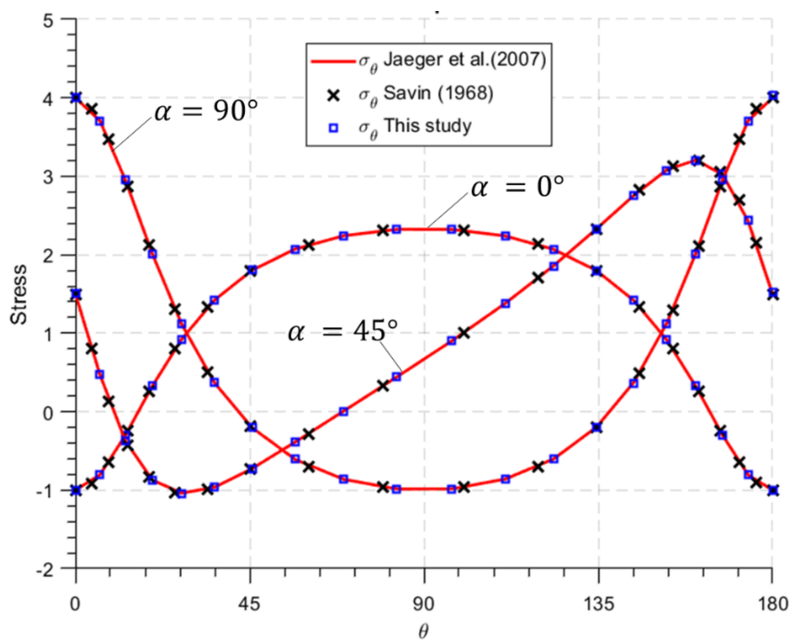


Figure 26. Hoop stress around an elliptical hole having $a/b = 3/2$, in an isotropic medium, subjected to a far-field stress acting at an angle $\alpha$ to the $x$-axis. The hoop stress is normalised against the far-field stress.

The proposed method can also be tested against results for an elliptical hole in an anisotropic medium. Savin (1961) considered an anisotropic material with Young's modulus ratio of $E_1/E_2 = 12$. For this material, the roots of the characteristic equation are

$\mu_1 = 3.08i$ and $\mu_2 = 1.12i$. Elliptical holes with $a/b = 3$ and $a/b = 1/3$ were considered, and the far-field stress was taken to be parallel to the $x$-axis. The normalised hoop stress is plotted in Figure 27, with the curves showing the values computed by the present method, and the data points taken from Tables 38 and 39 of Savin (1961). Again, the agreement is excellent.

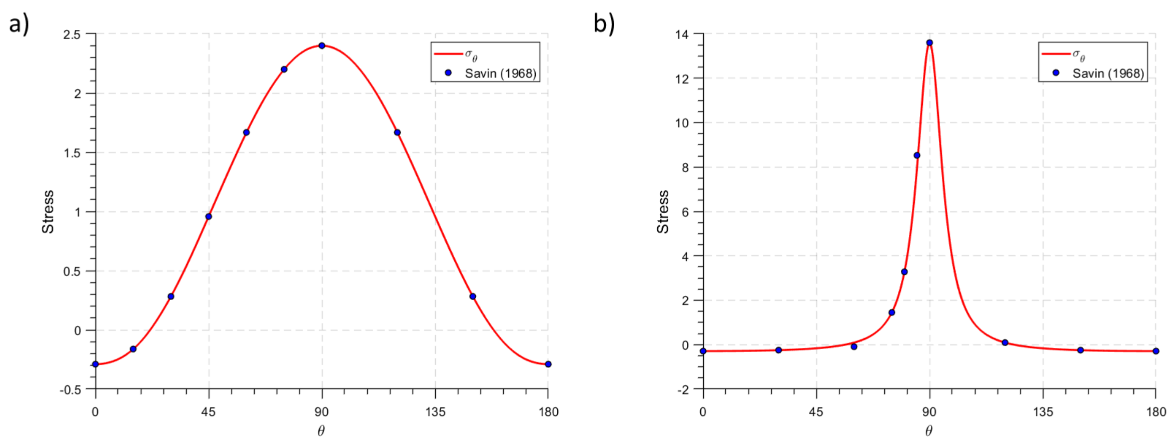


Figure 27. Normalised hoop stress around elliptical holes in an anisotropic medium, having (a) $a/b = 3$ and (b) $a/b = 1/3$, subjected to a far-field stress parallel to the $x$-axis. The curves show the values computed by the present method; the data points are taken from Savin (1961).

### *5.5.2. Triangular hole*

The distribution of stress around a triangular hole is given by Savin (1961) for the case of anisotropic materials. The equation of the hole contour was given by

$$x = \cos\theta + \frac{1}{3}\cos 2\theta\,, \quad y = -\sin\theta + \frac{1}{3}\sin 2\theta \tag{156}$$

which corresponds to a triangle that is "pointing towards" the positive $x$-axis. Using Melentiev's approximate method, the conformal mapping constants of this triangle are found to be $m_0 = 0.9978$, $m_1 = 0.0020$, $m_2 = 0.0019$, $m_3 = 0.3303$, $m_4 = 0.0006$, $m_5 = 0.0002$ and $m_6 = m_7 = m_8 = m_9 = 0.0001$. The stress distributions around the triangular hole, for the two cases in which the far-field stress is parallel to the $x$-axis or parallel to the $y$-axis, are shown in Figure 28. The results of the present method, shown as solid curves, are in an excellent agreement with those of Savin, which are shown as dots taken from Tables 5 and 6 of Savin (1961).

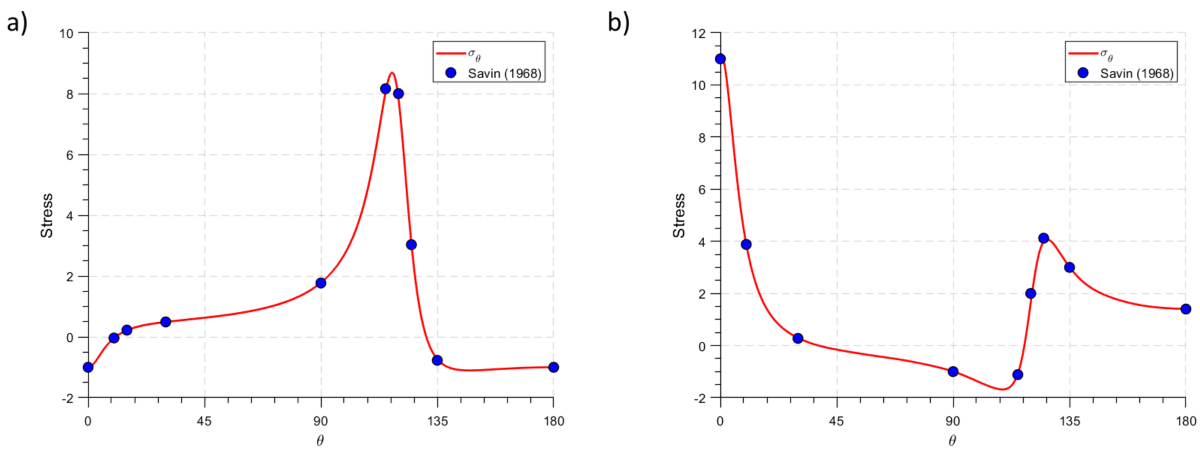


Figure 28. Normalised hoop stress around a triangular hole in an isotropic infinite plate, when the far-field stress is aligned with the (a) $x$-axis or the (b) $y$-axis. The solid curves are the predictions of the present method; the dots are taken from Savin (1961).

Daoust & Hoa (1991) proposed an analytical solution for a family of quasi-triangular holes in isotropic or anisotropic materials. The shape of their triangles was controlled by a shape factor $\varepsilon$, in which smaller values of $\varepsilon$ correspond to more rounded corners:

$$x = \cos\theta + \varepsilon\cos 2\theta\,, \qquad y = -\sin\theta + \varepsilon\sin 2\theta \tag{157}$$

The shapes of the triangles for $\varepsilon = 1/4$ and $\varepsilon = 1/8$ are shown in Figure 29, on the left. The tangential stresses around the contour are plotted for several values of $\varepsilon$, with the curves showing the predictions of the present method, and the data points taken from Daoust & Hoa (1991). Note that the curve for $\varepsilon = 1/3$ agrees closely with Savin's result, which corresponds to this same value of $\varepsilon$. Again, the newly computed values agree very closely with the values taken from the literature.

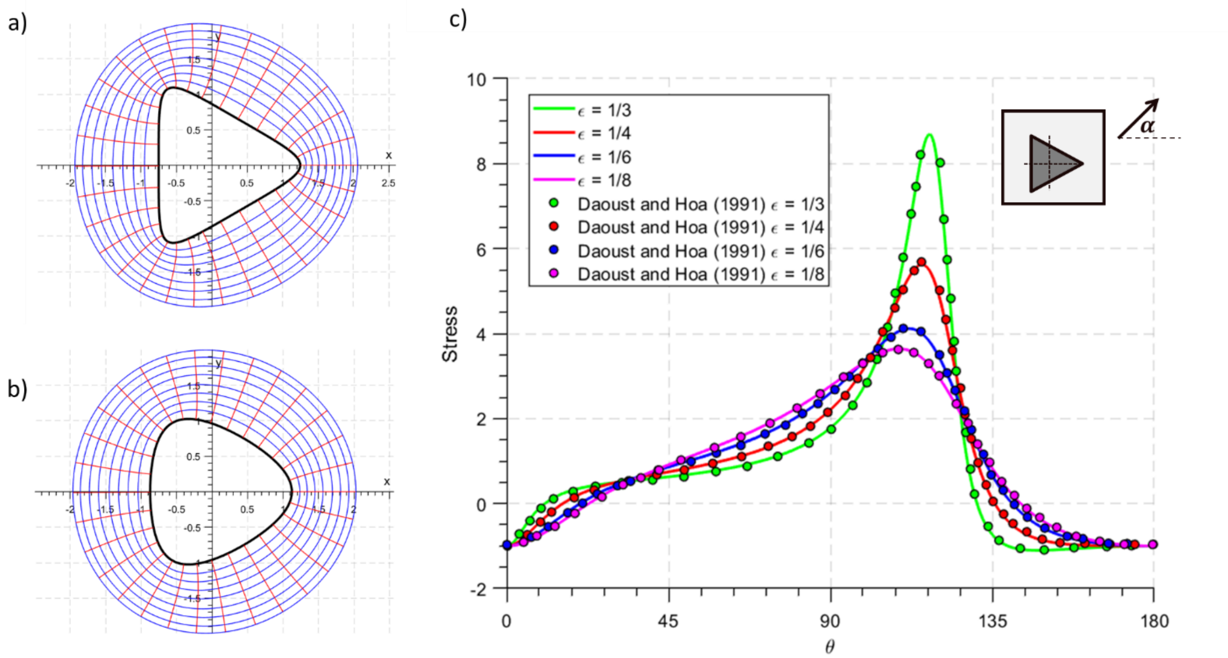


Figure 29. Quasi-triangular holes described by Eq. (157), for (a) $\varepsilon = 1/4$ and (b) $\varepsilon = 1/8$. (c) Normalised hoop stress around the hole, in an isotropic material, when the far-field stress is aligned with the $x$-axis, for various values of $\varepsilon$. The solid curves are the predictions of the present method; the dots are taken from Daoust & Hoa (1991).

Daoust & Hoa (1991) also considered an anisotropic plate described by the following roots of the characteristic equation: $\mu_1 = 2.3992i$ and $\mu_2 = 0.6757i$. The tangential stress along the hole is shown in Figure 30, for the case $\varepsilon = 1/3$, and far-field stress aligned with the $x$-axis. The agreement is again very good.

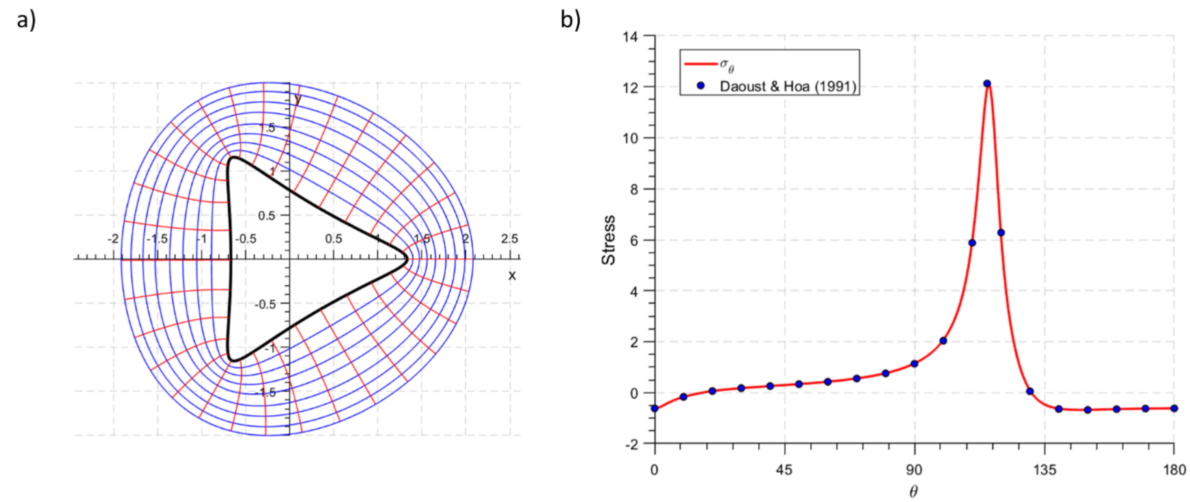


Figure 30. Quasi-triangular hole described by Eq. (157), for $\varepsilon = 1/3$, in an anisotropic material (see text for details), when the far-field stress is aligned with the $x$-axis. The solid curves are the values obtained by the present method; the dots are taken from Daoust & Hoa (1991).

### *5.5.3. Ovaloid hole*

Greenspan (1944) presented an analytical solution for an "ovaloid" hole in an infinite isotropic plate subjected to far-field uniaxial tension. He defined the ovaloid as a square hole with semi-circles appended at each of two opposing ends, and described its contour by the following equation:

$$x = 2.063\cos\theta - 0.079\cos 3\theta\,,\quad y = 1.108\sin\theta + 0.079\sin 3\theta \tag{158}$$

Lekhnitskii (1968) also addressed this problem, but used a slightly different equation for the hole that he described as "ovaloid", which explains the slightly different stresses obtained by these two authors. Greenspan showed that when the far-field stress is parallel to the $x$-axis, the hoop stress is given by

$$\sigma_\theta = \sigma_x^\infty \left[ \frac{4.915 - 7.133 \cos 2\theta}{3.723 - 2.316 \cos 2\theta + \cos 4\theta} \right] \tag{159}$$

and when the far-field stress is parallel to the $y$-axis, the hoop stress is given by

$$\sigma_\theta = \sigma_y^\infty \left[ \frac{1.079 + 7.517 \cos 2\theta}{3.723 - 2.316 \cos 2\theta + \cos 4\theta} \right] \tag{160}$$

In the present study, the conformal mapping constants of the ovaloid defined in Eq. (158) are found to be $m_0 = 1.5818$, $m_1 = 0.0029$, $m_2 = 0.4768$, $m_3 = -0.0003$, $m_4 = -0.0771$ and $m_5 = -0.0003$. The hoop stresses for the two loading cases, according to the analytic solution of Greenspan (1944) and the present method, are shown in Figure 31. Again, the agreement is very good.

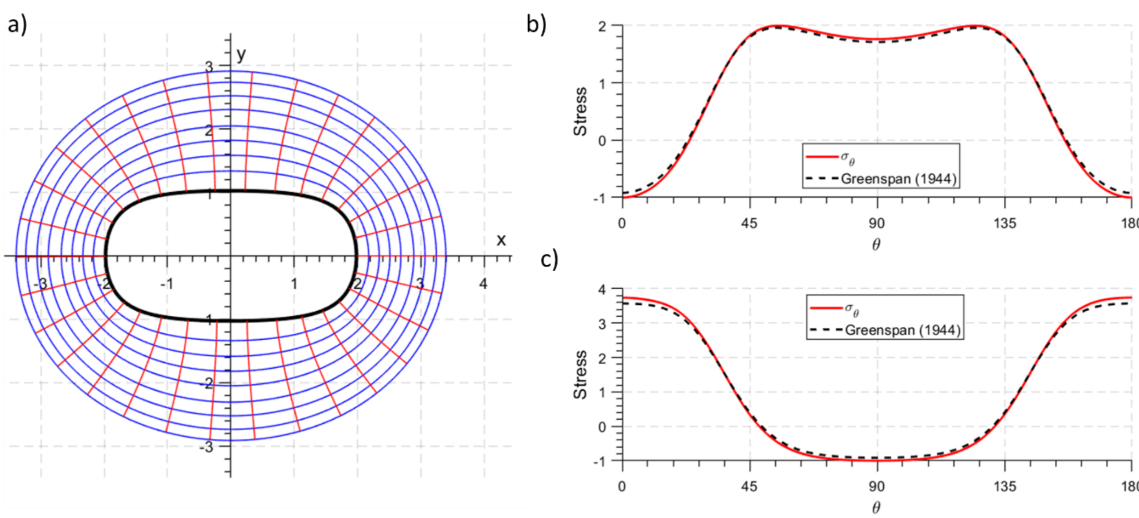


Figure 31. (a) Ovaloid hole described by Eq. (158). Normalised hoop stresses when the far-field stress aligned with the $x$-axis (b), and with the $y$-axis (c). Solid curves are the predictions of the present method, and dashed curves are expressions (159) and (160) derived by Greenspan (1944).

### *5.5.4. Square hole*

Stresses around a square hole in an infinite plate subjected to far-field stress have been studied by many authors, including Greenspan (1944), Lekhnitskii (1968), Savin (1961). Savin modelled a square hole using two terms of the Schwarz-Christoffel mapping:

$$x = \cos\theta - \frac{1}{6}\cos 3\theta, \quad y = -\sin\theta - \frac{1}{6}\sin 3\theta \tag{161}$$

and showed that the tangential stress around this hole is given by

$$\sigma_\theta = \frac{8\sigma^\infty}{5 + 4\cos 4\theta}\left(\frac{3}{8} - \frac{9}{7}\cos 2\alpha \cos 2\theta - \frac{3}{5}\sin 2\alpha \sin 2\theta\right) \tag{162}$$

where again $\alpha$ denotes the angle of rotation from the $x$-axis to the line of action of the far-field stress.

Using Melentiev's method, the conformal mapping constants of this quasi-square defined by Eq. (161) are found to be $m_0 = 0.9975$, $m_1 = 0.0012$, $m_2 = 0$, $m_3 = -0.0011$, $m_4 = -0.1629$, $m_5 = -0.0009$, $m_6 = -0.0002$ and $m_7 = -0.0001$. The hoop stresses for the two loading cases of $\alpha = 0°$ and $\alpha = 45°$, are shown in Figure 32, according to the analytic solution of Savin (1961) and the present method.

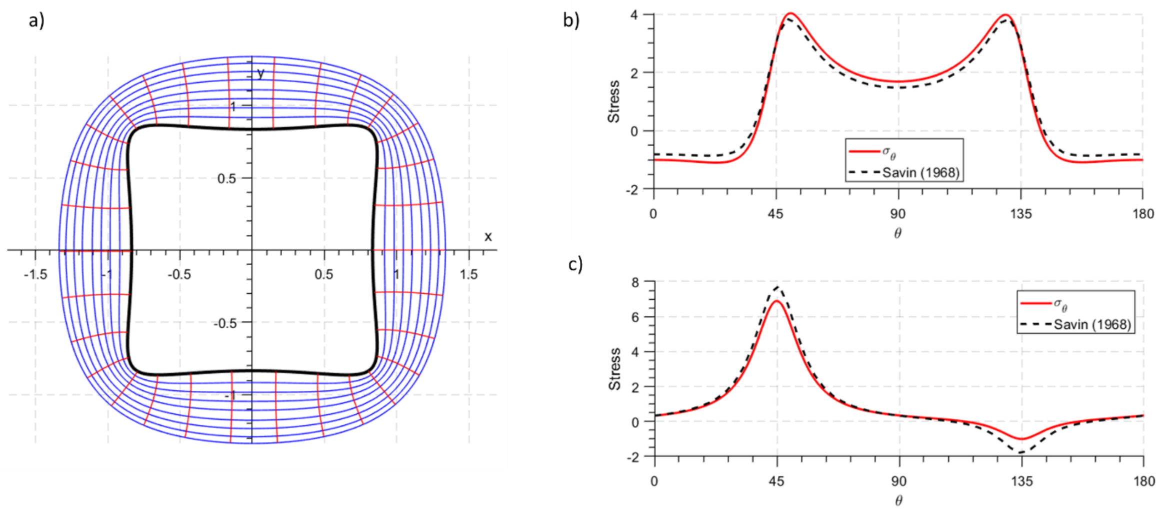


Figure 32. Stress around a quasi-square hole (a) in isotropic medium, when the external load is (b) aligned with the $x$-axis, and (c) rotated by 45° from the $x$-axis. The solid curves are the predictions of the present method, and the dashed curves are from the analytical solution derived by Savin (1961).

Ukadgaonker & Rao (2000) considered terms up to $\xi^{-19}$ in their conformal mapping, in order to obtain a closer approximation to an actual square. The non-zero coefficients in their mapping function were (in the present notation) $m_0 = 1$, $m_4 = 1/6$, $m_8 = 1/56$, $m_{12} = 1/176$, $m_{16} = 1/384$ and $m_{20} = 7/4864$. They considered an anisotropic material whose characteristic roots were $\mu_1 = 3.6404i$ and $\mu_2 = 0.2747i$. For the cases of far-field loading oriented at angles of $\alpha = 0°$, 45°, and 60°, the hoop stresses are shown in Figure 33, where they are compared with the values obtained by the present method. The agreement is very good, and the present method is able to capture the high-stress concentration at the corners.

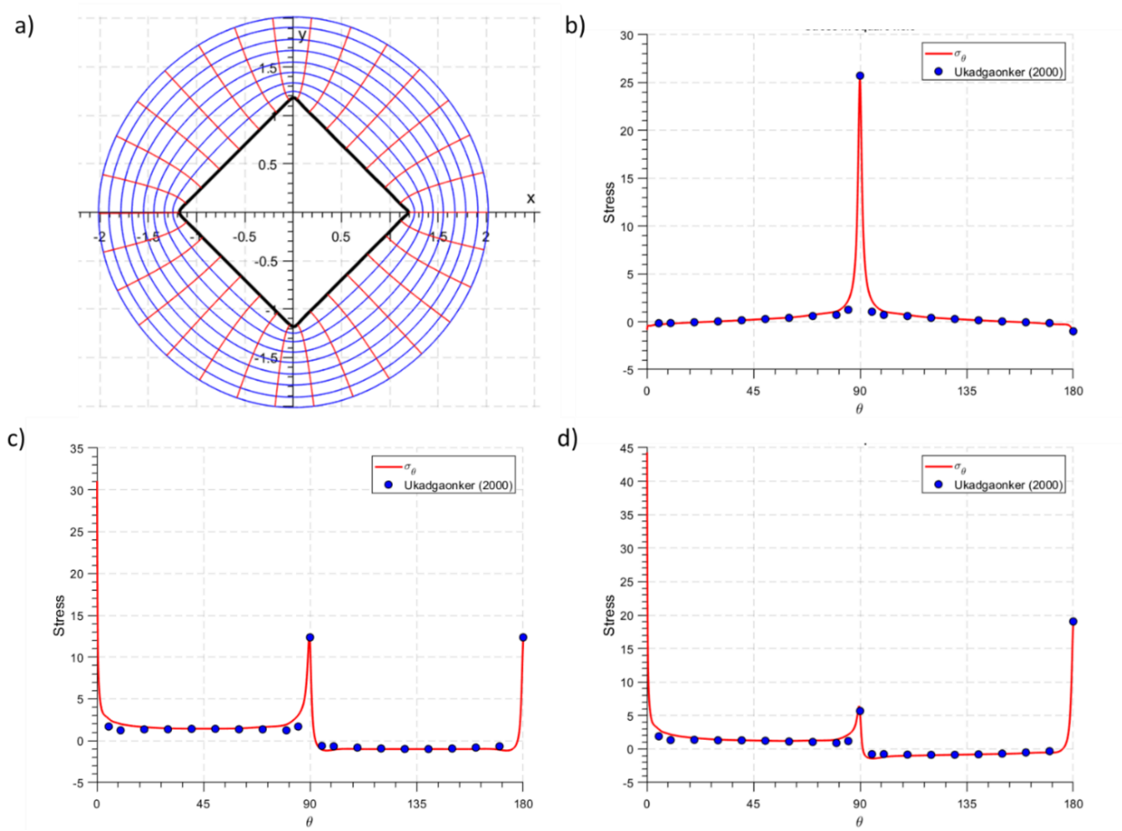


Figure 33. Hoop stress around a square hole, for far-field loadings at angles of $\alpha = 0°$, 45°, and 60°, in an anisotropic medium whose characteristic roots are $\mu_1 = 3.6404i$ and $\mu_2 = 0.2747i$. The solid curves are the predictions of the present method, and the points are from Ukadgaonker & Rao (2000).

Ukadgaonker & Rao (2000) also considered more complicated shapes, such as the distorted quasi-square with truncated corners shown in Figure 34. For the same anisotropic material as considered in the previous problem, with characteristic roots of $\mu_1 = 3.6404i$ and $\mu_2 = 0.2747i$, the hoop stresses are shown in Figure 34, for the case of loading along the $x$-axis, *i.e.*, $\alpha = 0°$. The agreement between their results and those obtained by the present method is reasonably close.

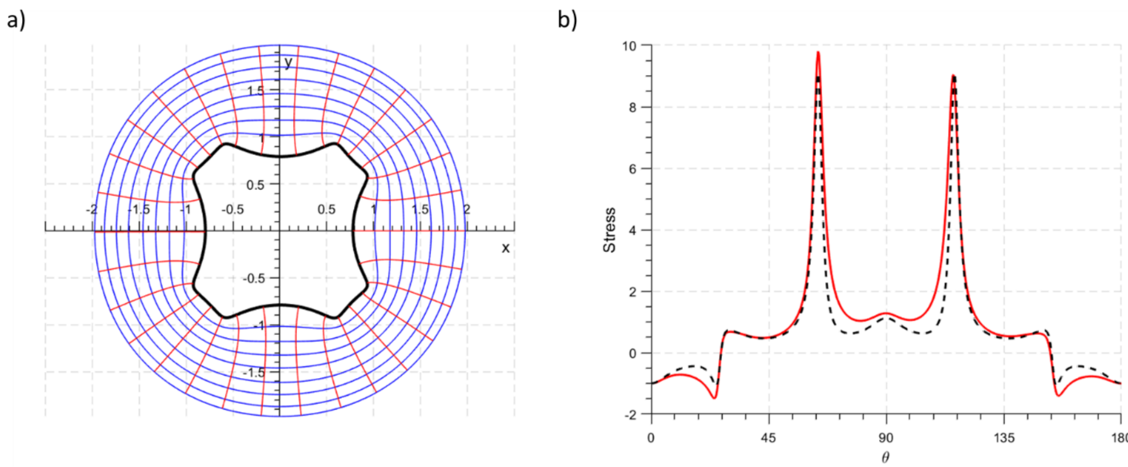


Figure 34. (a) A distorted quasi-square with truncated corners. (b) Normalised hoop stress around the hole, for a far-field loading oriented in the $x$-direction, in an anisotropic medium whose characteristic roots are $\mu_1 = 3.6404i$ and $\mu_2 = 0.2747i$. Solid curves are the predictions of the present method; dashed curves are from Ukadgaonker & Rao (2000).

### *5.5.5. Stress around a non-symmetrical and irregularly shaped hole*

The previous examples all involved holes having some degree of symmetry, and shapes that were in some sense reasonably "simple", such as quasi-polygons. However, this unified methodology that can compute the stresses around an arbitrarily-shaped hole will perhaps find its greatest usefulness for holes that have very irregularly and rough shapes.

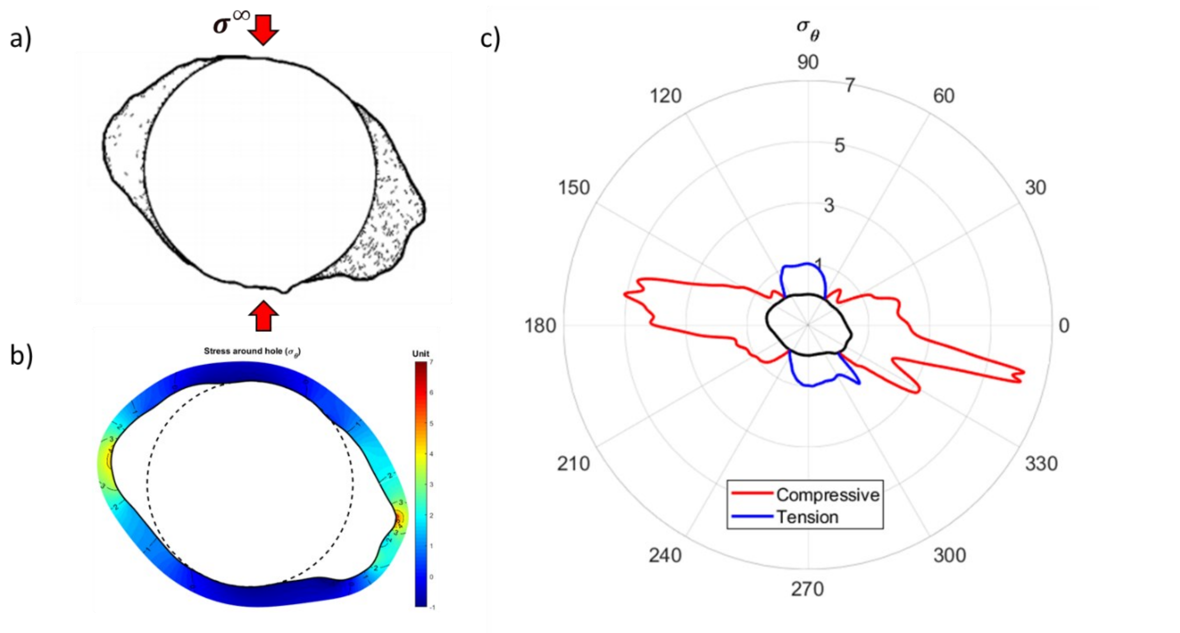


Figure 35. (a) Wellbore breakout in an isotropic medium, after Zoback *et al*. (1985), and (b and c) the tangential stress around the hole, under uniaxial far-field compression.

One source of such shapes are subsurface boreholes, which are initially drilled as circular holes, but then often suffer from "breakouts", in which small regions of rock at the borehole wall break off (and fall into the borehole, to be swept away by the drilling fluid) due to local failure, leading to a non-circular shape. The remaining rock can be treated as elastic as per the assumption of the proposed method, and the method developed in this paper can be used to compute the new stresses, to check if an equilibrium shape has been reached. Pre-drilling wellbore stability analysis is often carried out by assuming a circular wellbore and with the aid of a downhole caliper tool, and it is known that actual wellbores rarely have the shape of an ideal circle. It is of great interest for drilling practice to understand the stability of a wellbore by identifying the region around the wellbore wall that has a high-stress concentration.

### 5.5.6. *Validity of solution away from the hole contour in isotropic and anisotropic medium*

Although the method used to determine the mapping functions was different, the method used here to determine the complex potentials is very close to that used by Ukadgaonker & Rao (2000). Their method was criticised by Lu *et al*. (2015), who claimed that the potentials $\phi_0(\xi)$ and $\psi_0(\xi)$ thus derived will be analytical functions on the hole contour, but will *not* be analytical in the region exterior to the contour; see Lu *et al*. (2015) for the details of their argument. They concluded that although the computed stresses will be correct on the hole boundary, the stresses away from the boundary "should not be correct", although no evidence was given of this assertion. For isotropic material, to verify the validity of the stresses computed by the present methodology at points in the body that are not situated along the hole contour, comparison can be made to the stresses that were computed numerically by Maugis (1992) who proposed a solution valid for an elliptical cavity.

Maugis (1992) proposed a closed-form solution to compute the stress components around an elliptical cavity in isotropic medium. Along the $x$-axis the equation for $\sigma_x$ and $\sigma_y$ are (Eqs.2.123 – 2.126 in Maugis (1992)):

$$(a^2-b^2)\left(\frac{\sigma_x}{\sigma^\infty}\right)_{y=0} = -a^2 + \frac{a|x|}{(x^2-a^2+b^2)^{\frac{1}{2}}}\left[a - \frac{b^2(a-b)}{x^2-a^2+b^2}\right] \tag{163}$$

$$(a^2-b^2)\left(\frac{\sigma_y}{\sigma^\infty}\right)_{y=0} = b^2 + \frac{a|x|}{(x^2-a^2+b^2)^{1/2}}\left[a - 2b + \frac{b^2(a-b)}{x^2-a^2+b^2}\right] \tag{164}$$

and along the $y$-axis:

$$(a^2-b^2)\left(\frac{\sigma_x}{\sigma^\infty}\right)_{x=0} = -a^2 + \frac{a|y|}{(y^2+a^2-b^2)^{1/2}}\left[a + \frac{a^2(a-b)}{y^2+a^2-b^2}\right] \tag{165}$$

$$(a^2-b^2)\left(\frac{\sigma_y}{\sigma^\infty}\right)_{x=0} = b^2 + \frac{a|y|}{(y^2-a^2+b^2)^{1/2}}\left[a - 2b - \frac{a^2(a-b)}{y^2+a^2-b^2}\right] \tag{166}$$

The major and minor axes of the ellipse are denoted by $a$ and $b$. Figure 36 to Figure 39 show the stress components up to $3a$ from the hole boundary of an ellipse with $b/a = [0.2, 0.3, 0.5, 0.7]$. The stress component calculated using Maugis' closed-form solution is shown as the black-square in each plot. The $\sigma_x$ and $\sigma_y$ stress components along the $x$ and $y$-axes under uniaxial loading $\sigma^\infty$ parallel with the $y$-axis in Figure 36 to Figure 39 is calculated up to $3a$ from the hole boundary of an ellipse with $b/a = [0.2, 0.3, 0.5, 0.7]$. At the hole boundary, the analytical solution of the stress concentration factor (SCF) is

$$\left(\frac{\sigma_y}{\sigma^\infty}\right)_{y=0} = 1 + 2\left(\frac{a}{b}\right) \tag{167}$$

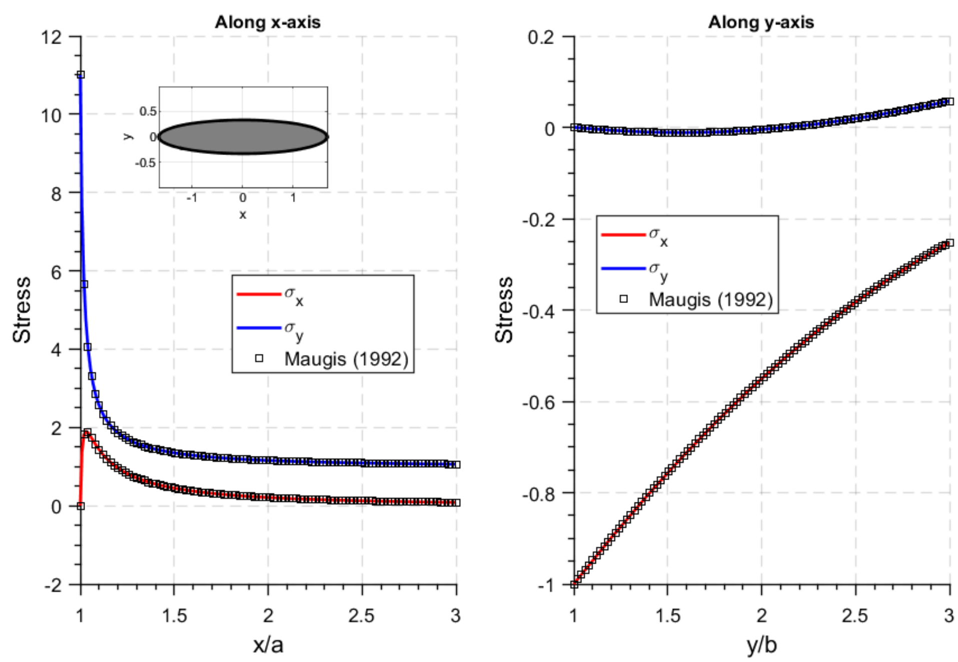


Figure 36. Stress around elliptical cavity with $b/a = 0.2$. The exact analytical solution of the higher stress according to Eq. (167) is $\sigma_y^{max} = 11$ at the tip of the long axis.

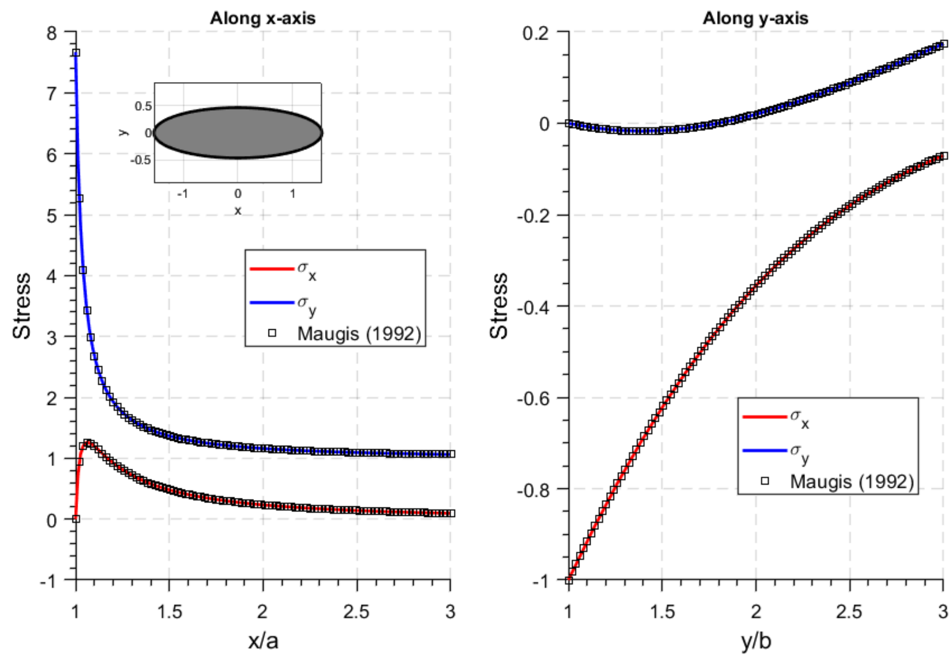


Figure 37. Stress around elliptical cavity with $b/a = 0.3$. The exact analytical solution of the higher stress according to Eq. (167) is $\sigma_y^{max} = 7.67$ at the tip of the long axis.

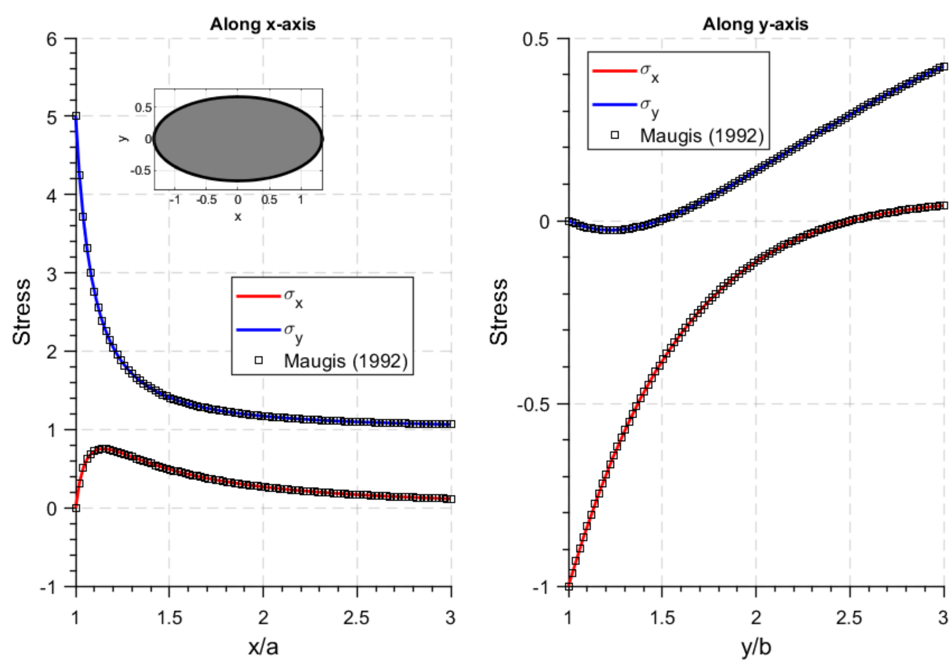


Figure 38. Stress around elliptical cavity with $b/a = 0.5$. The exact analytical solution of the higher stress according to Eq. (167) is $\sigma_y^{max} = 5$ at the tip of the long axis.

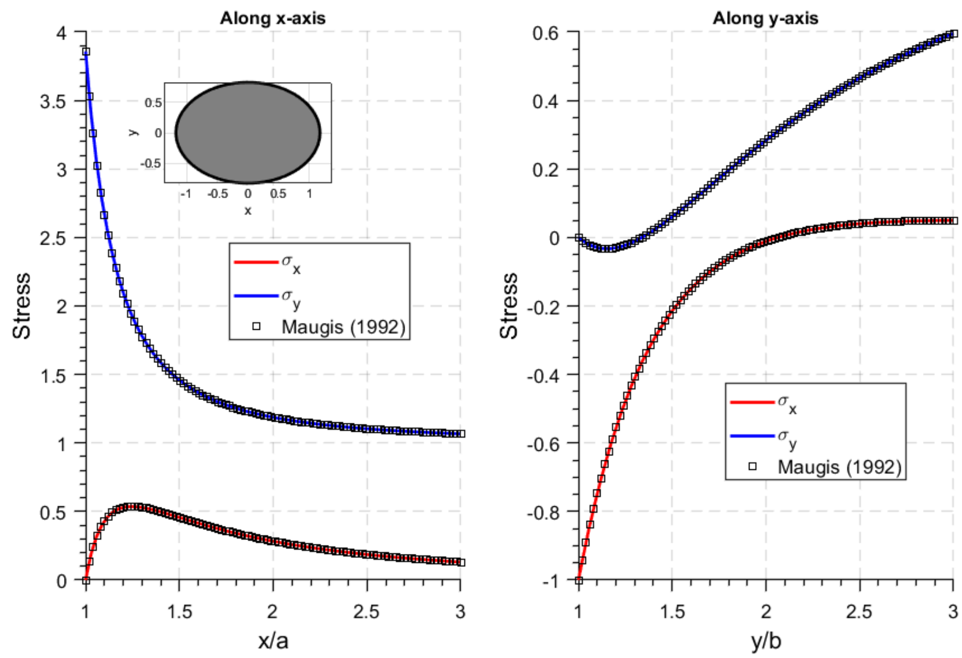


Figure 39. Stress around elliptical cavity with $b/a = 0.7$. The exact analytical solution of the higher stress according to Eq. (167) is $\sigma_y^{max} = 3.88$ at the tip of the long axis.

For anisotropic material, to verify the validity of the stresses computed by the present methodology at points in the body that are not situated along the hole contour, comparison can be made to the stresses that were computed numerically by Lu *et al*. (2015), using commercial finite element software, around a "Reuleaux triangle" hole in an orthotropic material; see Figures 10 to 12 in Lu *et al*. (2015), and Figure 40 to Figure 41 in here. This is one of the few, if not the only, examples available in the literature in which the stresses have been plotted along one of the co-ordinate axes, moving away from a non-circular hole in an anisotropic material. In this example, the elastic anisotropy was characterised by $\mu_1 = 1.3733i$ and $\mu_2 = 0.9242i$, and the far-field stress state was taken to be $\sigma_{xx}^{\infty} = 10$ MPa, $\sigma_{yy}^{\infty} = 15$ MPa, and $\sigma_{xy}^{\infty} = 0$ MPa.

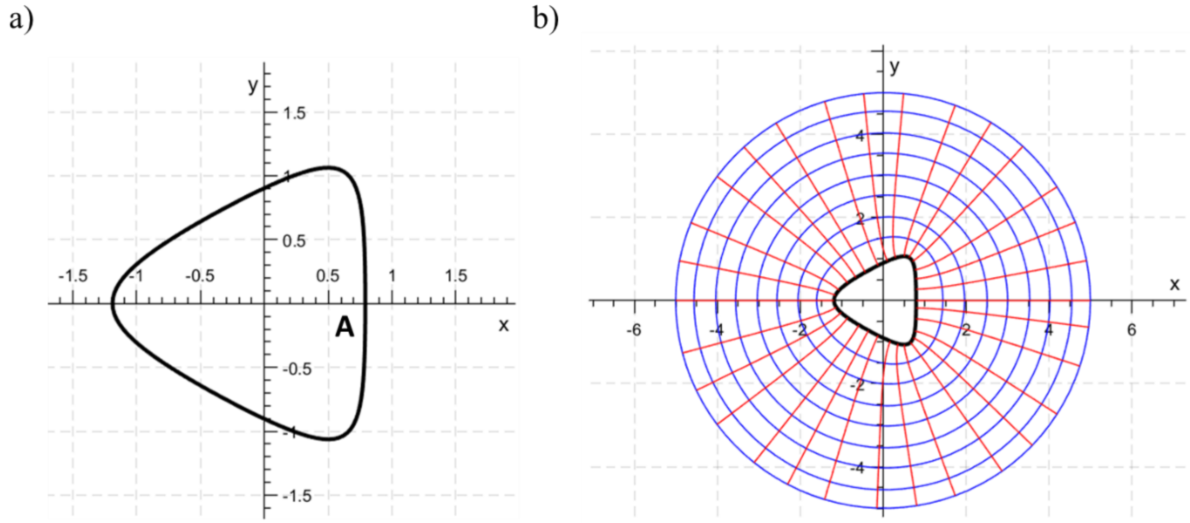


Figure 40. (a) The Reuleaux triangle shape, and (b) the conformal mapping of the hole.

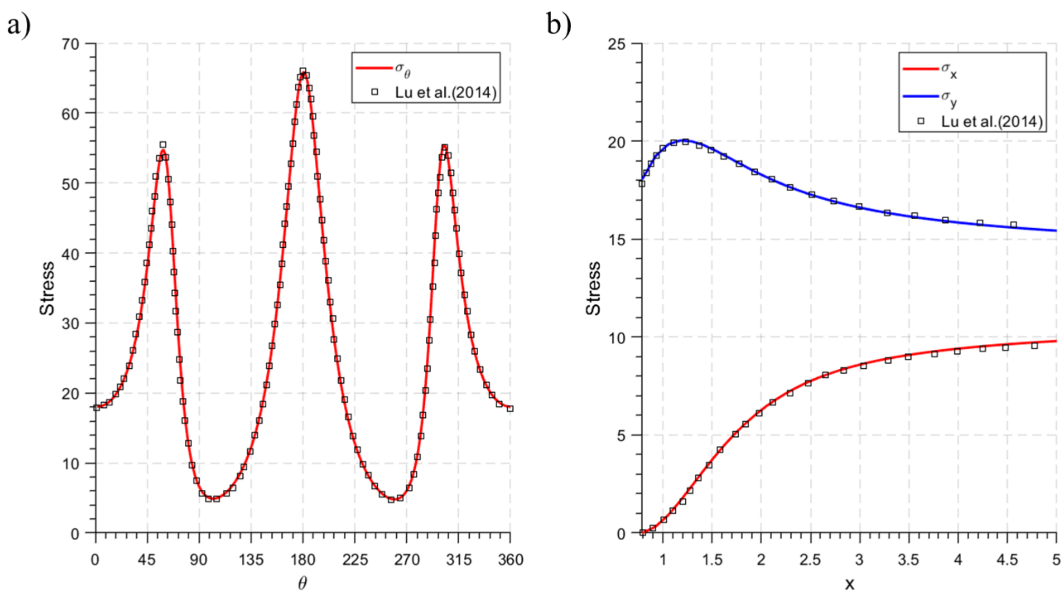


Figure 41. (a) The hoop stresses around the Reuleaux triangular hole boundary shown in Figure 40, and (b) the two normal stresses along the $x$-axis. The symbols are the values computed in Lu *et al*. (2015) using finite elements; the curves show the stresses computed by the present method.

The hoop stresses along the hole boundary that have been computed using the proposed method are compared in Figure 41a against those computed numerically in Lu *et al*. (2015). The agreement is excellent. The stress components $\sigma_{xx}$ and $\sigma_{yy}$, along the $x$-axis, are plotted in Figure 41b. Again, the agreement between the present method and the numerical calculations of Lu *et al*. (2015) is excellent. Furthermore, it should be noted that the stresses computed by the present methodology converge smoothly to the correct far-field stresses at distances of roughly five "hole diameters" from the hole boundary, proving that the present methodology does not become inaccurate away from the hole.

# Chapter 6 Breakout modeling and near-wellbore stress profiling

This chapter presents the implementation of the method proposed in Chapter 5 for two purposes. The first objective is to model the wellbore breakout development around a wellbore. Comparison with a numerical modelling and experimental test by Herrick & Haimson (1994) has been carried out to validate the successive breakout modelling process. However, the ultimate goal of the modelling is to assess whether or not there is a correlation between breakout geometry and *in situ* stress and if it is possible to infer the magnitude of the *in situ* stress from breakout geometry.

The second objective of this chapter is to leverage the value of ultrasonic imaging tools to obtain near-wellbore stress components. The exercise allows the effect of the cross-sectional hole geometry to be investigated and its impact on the near-wellbore stress to be examined. For this purpose, actual ultrasonic data have been used in which a total of 180 data points were obtained at each depth from the ultrasonic borehole imaging data; this will give a 2° azimuthal resolution of wellbore circumference that can sufficiently capture any local irregularities that may exist around the wellbore wall. The successive breakout modelling and *in situ* stress estimation from breakout geometry will be first discussed in the subsequent section followed by the near-wellbore stress profiling using ultrasonic data.

## 6.1. Semi-Analytical Method for Modelling Wellbore Breakout Development

This section discusses the episodic development of a stable breakout, and ultimately attempts to find a relationship between *in situ* stress and breakout geometry. Although the process discuss here reflects an evolution of a successive process, this cannot be associated with an actual time scale clock. The change in each successive process is only related to the change in the hole cross-sectional shape from circular to non-circular. As the modelling of the breakout development requires a method that allows the stress components to be computed around non-circular holes and irregular hole geometries, the semi-analytical solution procedure developed Chapter 5 is used. With this method, it is possible to track the development of the breakout and examine the stability of the breakout geometry at each episode and, hence, its development can be tracked. Finally, the relationship between the Mogi-Coulomb failure function and breakout geometry is established as an alternative method for the estimation of minimum *in situ* stress.

Borehole breakout, defined as a diametrically opposed elongation along a preferred direction of an initially circular wellbore resulting from stress-induced rock failure, has been studied for more than three decades. This phenomenon is often encountered in mine tunnels and petroleum wellbores, in areas of high *in situ* stress. Observations of breakout were reported by Leeman in 1964 at a gold mine in South Africa, and also by Carr in 1974 who observed consistency between the breakout orientation with the least *in situ* stress in Yucca Flat, Nevada (Haimson, 2007). Later, Bell & Gough (1979) also observed a strong correlation between breakout orientation and the direction of the minimum horizontal stress in Alberta, Canada. To substantiate their observation, Gough & Bell (1982) proposed a breakout model using the Mohr-Coulomb failure criterion and the Kirsch equations. Since then, numerous researchers have verified that the concentrated stress around the wellbore is responsible for the development of the breakout, and that the orientation of the breakout is parallel to the least principal stress direction. This phenomenon has attracted practitioners and researchers to try to use breakout geometry as a tool to estimate *in situ* stress orientation and magnitude, due to the abundant availability of such inexpensive datasets.

Extensive efforts have been made to verify the relation between breakout formations with *in situ* stress and whether, in an inverse manner, *in situ* stress can be inferred from the breakout geometry. For instance, Plumb & Hickman (1985) concluded that the direction of the minimum principal stress can be inferred from the elongation detected by the dipmeter and borehole televiewer. Independently, Zoback *et al*. (1985) also used an ultrasonic borehole televiewer and concluded that the failure around the wellbore is strongly controlled by the magnitude and orientation of the *in situ* stress field. Plumb (1990) later concluded that breakout may be used to infer the relative magnitude and orientation of the near-wellbore stress. Similarly, Mastin (1988) studied the rotation of breakout orientation in deviated wellbores, which depends on the relative magnitude of the near-wellbore stress. At the *Underground Research Laboratory* (URL) in Canada, Read *et al*. (1995) observed non-symmetrical breakouts in a borehole that was not aligned with the principal axis. In conjunction with numerical modelling and microseismic monitoring, they concluded that the asymmetric breakout appearance is caused by the influence of the antiplane shear stress. By integrating the results that they obtained from hydraulic fracturing, borehole televiewer, and numerical modeling, Kim *et al.* (2017) proposed an integrated method to estimate the *in situ* stress. The breakout dimension from their numerical model for a particular horizontal stress ratio and rock property was compared with the observation from borehole televiewer to determine the most appropriate *in situ* stress.

Several attempts have also been made to understand the mechanism of breakout formation through laboratory experiments. Lee & Haimson (1993) used cubical specimens of Lac du Bonnet granite to investigate the micro-mechanism of a ‘dog-eared’ shaped breakout. They observed a progressive detachment of thin long flakes due to extensile cracking in two zones aligned with the minimum principal stress direction. A comprehensive review of breakout micromechanisms in a variety of rock types, *e.g.* granites, limestones, and sandstones, was given by Haimson (2007). He concluded that, depending on the rock type, the microcracks leading to breakout could fail in tensile or shear openings, extending inter- or intra-granularly producing a dog-eared shape of breakout; except for a high porosity quartz-rich sandstone which develops a fracture-like breakout due to grain debonding and compaction along with the least principal stress.

Several researchers have also attempted to model breakout development using numerical and analytical modelling. The first breakout model was proposed by Gough & Bell (1982), based on the hypothesis that shear fractures occur at the points of the highest tangential stress. They adopted the Mohr-Coulomb failure criterion to predict the successive two conjugate shear fractures tangent to the borehole wall. Their model, however, is independent of the *in situ* stress magnitude and only depends on the friction angle of the rocks. The model was later improved by Zoback *et al*. (1985) by calculating the stress around the borehole using the Kirsch equations, and assessing the zone within which shear fractures occur, according to the Mohr-Coulomb failure criterion. Although their work was an improvement from that of Gough & Bell (1982), by accounting for the stress, their predicted breakout geometry is rather shallow and flat-bottomed; it seems that they were only calculated the *initial* breakout geometry.

Ever since, numerous researchers have proposed numerical models for a successive breakout initiation, growth, and stabilization. A comprehensive review of the mechanism and experimental and modelling results of breakouts was provided by Germanovich & Dyskin (2000). To capture the episodic breakout development, it is necessary to compute the stress state to assess their stability at each episode. Such studies have been carried out by Zheng *et al*. (1989), who used the boundary element method to model the progressive spalling of thin slabs near the hole wall by extensile splitting; see also Ewy *et al*. (1987) and Zheng *et al*. (1988). Herrick & Haimson (1994) compared breakout geometries obtained from prismatic specimens of Alabama limestone under a true-triaxial stress state with numerical simulations considering the scaling effect due to the hole size. Their numerical model is used to simulate a vertically drilled borehole under constant *in situ* stress based on the plane strain linear elastic boundary element method. The extent of the breakout zone at each step is obtained by comparing the stress around the wellbore with the Mohr-Coulomb failure criterion. Herrick & Haimson (1994) experimental result is used in the present paper for verification purposes. Du & Kemeny (1993) considered heterogeneous and discontinuous rocks with a random distribution of microcracks to simulate the breakout formation as a result of the interaction and coalescence of the microcracks in Westerly granite. Considering the strength anisotropy of the rocks, Duan & Kwok (2016) studied the effect of anisotropy on the initiation, propagation, and pattern of borehole breakout in shale using discrete element modelling. Sahara *et al*. (2017) modelled the evolution and stabilization of borehole breakouts using continuum damage mechanics (CDM) by considering the changes of the elastic moduli as a result of the failure around the hole.

Zhang *et al*. (2018) numerically modelled the successive spalling leading to a stable breakout, and then inverted the knowledge of the final geometry to obtain the *in situ* stress. They concluded that the *in situ* stress can be effectively obtained from breakout geometry. Later, Zhang *et al*. (2019) also investigated the potential misinterpretation of breakdown pressure from hydraulic fracturing in a borehole with breakout, and concluded that the difference with that of a perfectly circular wellbore could be as large as 82%. Using finite-element method, Tan *et al*. (2019) developed a workflow, which they referred to as *Failure Geometry Stabilization* (FGS), to simulate the drilling and breakout development, progression, and stabilization of shale rocks. The method was validated using polyaxial block tests on Wellington shale and Pierre II shale. Although numerical models such as finite-element and boundary-element have been implemented extensively for such a problem, analytical solutions can provide the advantage to allow for a parametric investigation. Recently, Gerolymatou (2019) proposed a method to analytically model breakout evolution in isotropic materials using conformal mapping. The same method was then used by Gerolymatou & Petalas (2020) to estimate the magnitude of in situ stress based on the width and depth of brittle borehole breakouts. In the same spirit, this research is focused on the implementation of the semi-analytical procedure laid out in Chapter 5 to model breakout development.

#### *6.1.1. Comparison with measurements of Herrick and Haimson (1994)*

To model the successive formation of the breakout, it is necessary for the stress components to be computed as the boundary evolves at each episode. In the following examples, the initial hole is assumed to be a circle in a linearly elastic, homogeneous and isotropic infinite plate. The plate is subjected to three unequal far-field *in situ* stresses (Figure 42a).

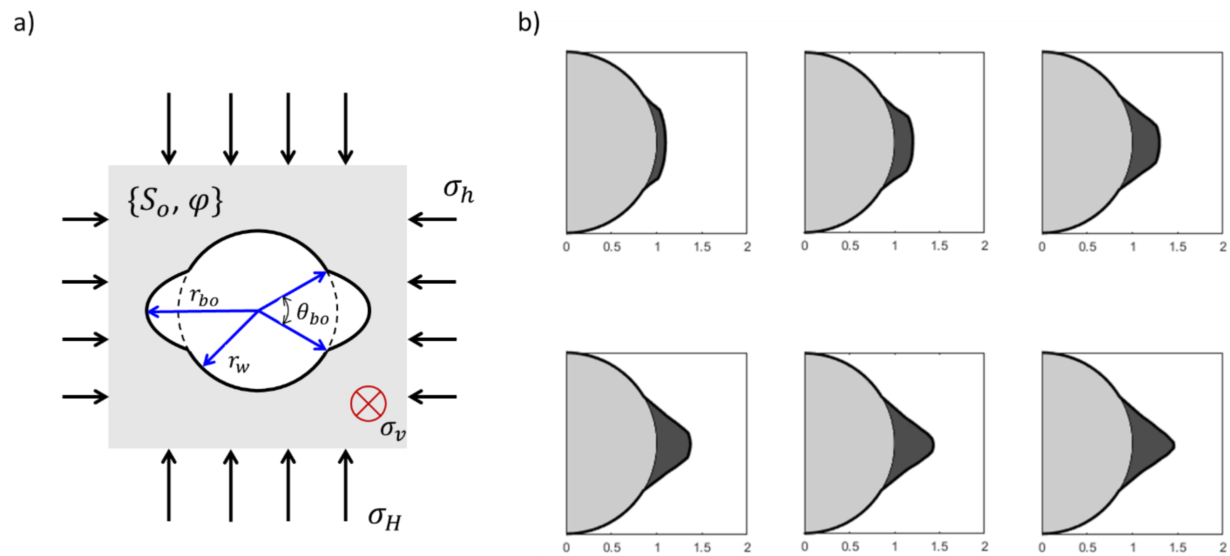


Figure 42. (a) Problem definition and (b) the episodic breakout development of rock with $UCS = 16{,}800$ psi and $\varphi = 20°$ under a far-field stress state of $\{\sigma_v; \sigma_H; \sigma_h\} = \{4{,}100;\ 8{,}500;\ 3{,}050\}$ psi.

To initiate the simulation, the stress components around the circular wellbore are calculated using Eqs. (147) to (149). The *in situ* stresses $\{\sigma_v; \sigma_H; \sigma_h\}$ are applied instantaneously, *i.e.* their magnitude is not ramped up during the simulation. In this work, the value of the *in situ* stresses are chosen according to the work of Haimson & Herrick (1994). The rock strength parameter is kept constant throughout the simulation; unlike in Herrick & Haimson (1994) who applied a scaling factor in their cohesion as the breakout progresses. The stress components, *i.e.* the tangential stress, radial stress, and axial stress calculated at each point around the wellbore, are then inserted into the failure criteria, *e.g.*, Mohr-Coulomb or Mogi-Coulomb, to examine the stability of the rock. The zone within which the stress state satisfies the failure criterion is then removed, and the new outline of the cross-sectional shape is captured. The number of layers to be removed at each iteration was arbitrarily chosen to be 1/50 of the wellbore radius. By changing the element size by a factor of 0.5 of the original size (1/50), will alter the result by less than 5% from the original size. In the same way, Zheng *et al.* (1989) arbitrarily chose the radial thickness of their model to be 1/15 of the wellbore radius and found out that the difference with the original thickness is not more than 1/15, *i.e.* approximately 6.7%, of wellbore radius after changing the thickness of the segment by a factor of 0.5. An iterative Melentiev conformal mapping procedure is then performed to determine the appropriate conformal mapping coefficients for the new shape, after which the stress is again computed. This procedure is repeated until incremental breakout depth is insignificant as compared with the preceding step; which, in this work, is assumed to be $10^{-5}$. At this point, the breakout is said to be at its stable state. The procedure is illustrated in Figure 43.

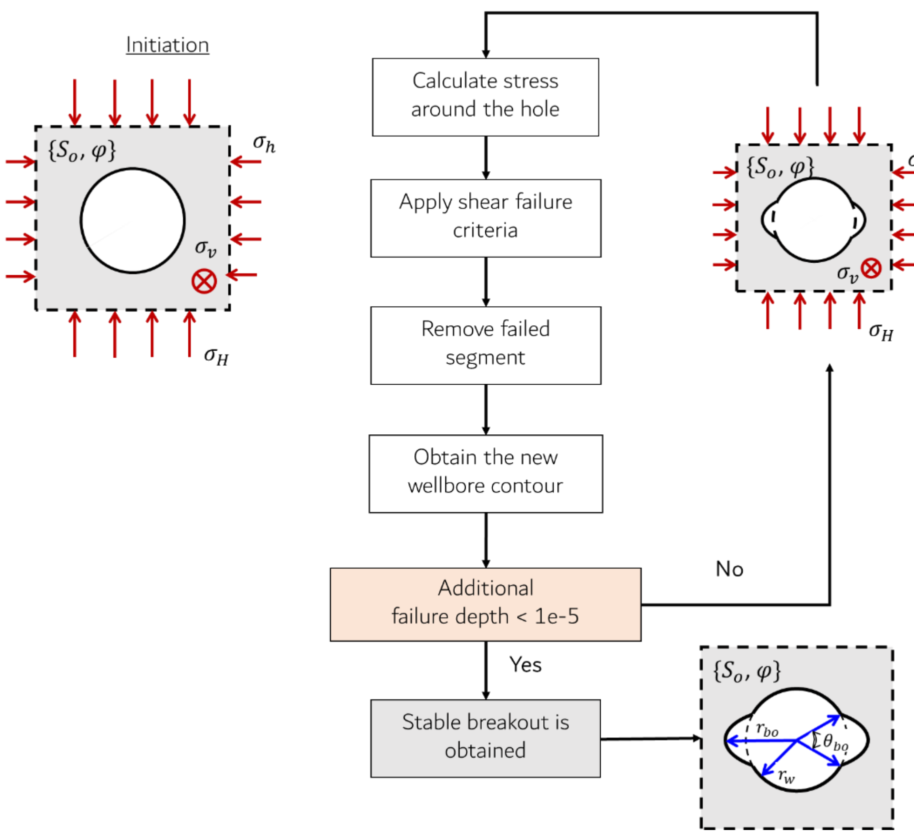


Figure 43. Modelling of episodic development of borehole breakouts.

At each step, the geometry of the forming breakout, *i.e.* the width of the breakouts ($\theta_{bo}$) and the tip of the breakouts ($r_{bo}$), are captured, as shown in Figure 42b. The relationship between the final breakout geometry and the *in situ* stress can then be examined.

The parameters used in the modelling are taken from Herrick & Haimson (1994), who conducted a breakout initiation experiment on Alabama limestone under true-triaxial stress; comparison with their experimental results will also be presented here. (Note that the stresses reported by Herrick & Haimson (1994) were given in MPa, and will be converted into psi in the present work.) The compressive strength of the Alabama limestone was 16,800 psi (after taking into account the scale effect of the hole) with a friction angle of 18° (±2°). The vertical stress ($\sigma_v$) was 1,015 psi higher than the minimum horizontal stress ($\sigma_h$). The experimental result of Herrick & Haimson (1994) resembling the "cusp" or "dog-eared" shaped of the breakout geometry, as shown in Figure 44a, was created under a stress state of $\sigma_h$ = 4,100 psi and $\sigma_H$ = 12,050 psi.

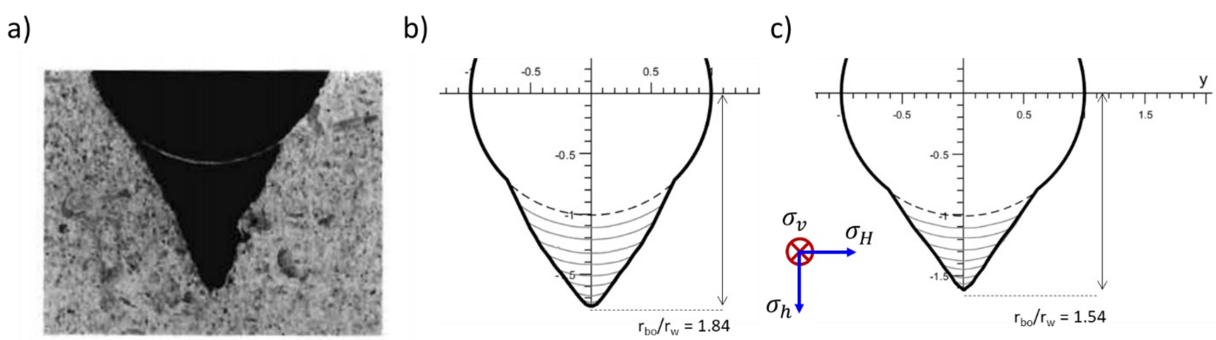


Figure 44. (a) The experimental breakout shape observed by Herrick & Haimson (1994); the modelled breakout geometry using the (b) Mohr-Coulomb and (c) Mogi-Coulomb failure criteria, respectively.

The final breakout shape obtained using the present semi-analytical method is shown in Figure 44b, when the Mohr-Coulomb failure criterion is considered. The breakout tip extends deep into the formation to a stable position at $r_{bo}/r_w = 1.84$ , with a breakout width of $\theta_{bo} = 88°$. If the Mogi-Coulomb failure criterion is used, the final breakout geometry is relatively narrower and shallower; with $r_{bo}/r_w = 1.54$ and $\theta_{bo} = 76°$, as shown in Figure 44c. The strengthening effect introduced by the intermediate principal stress in the Mogi-Coulomb failure criterion is responsible for the less severe breakout geometry. In Figure 44, the final breakout geometry of the laboratory experiment and numerical modelling are deep and sharp, with a pointed edge that resembles a "cusp" or "dog-eared" shaped. The azimuth of the breakout propagation is also parallel to the direction of the least principal stress.

### *6.1.2. Evolution of wellbore shape and the stress around the hole*

Several authors, such as Zheng *et al*. (1989), Zoback *et al*. (1985), (2003) and Herrick & Haimson (1994), observed that the width of the breakout remains constant throughout its initiation, progression, and stabilization. The breakout width aperture of each growth episode is relatively smaller than that of the preceding steps, leading to an overall sharp, pointed-end breakout (Figures 43b and 43c). Shown in Figure 45 is the evolution of the near-wellbore stress during breakout development of the same rock under a stress state of $\{\sigma_v; \sigma_H; \sigma_h\} = \{4{,}060;\ 7{,}500;\ 3{,}045\}$ psi. This stress state represents one possible scenario that one may encounter in a real situation. Shown in Figure 45 is the normalised major principal stress $(\sigma_1/\sigma_v)$ around the failed zone increases as the breakout develops. A detailed examination suggests that, as the breakout tip sharpens and deepens, the stress concentration becomes more localized around the tip, with increasing magnitude. In the case considered here, the major principal stress is more than ten-times the vertical stress $(\sigma_v)$ near the tip of the final breakout geometry. The stress state at the tip does satisfy failure criterion, however, the size of the failed region is now so insignificant that the process is considered to have converged.

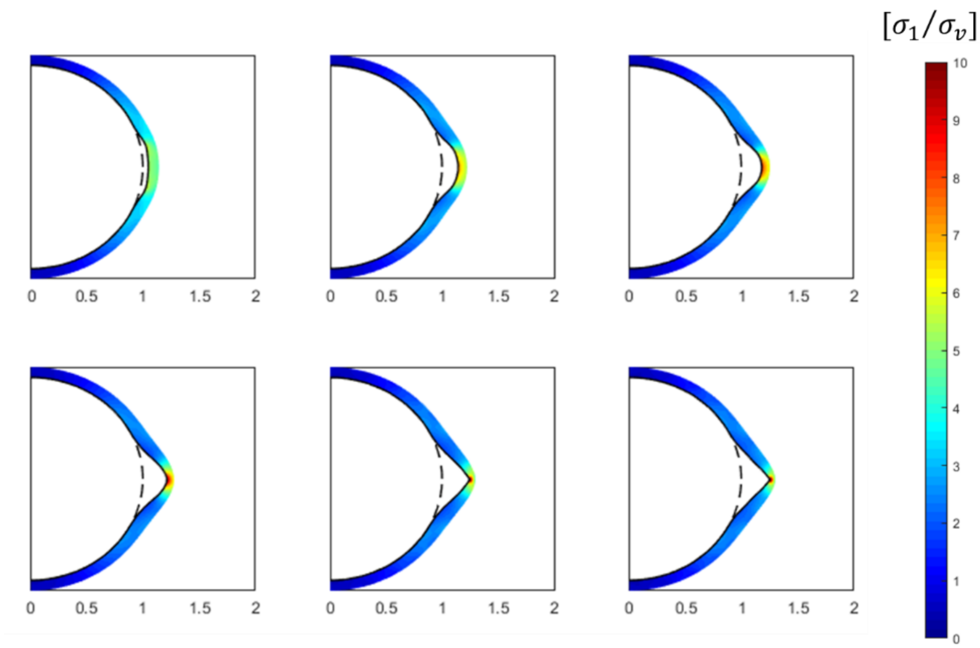


Figure 45. An episodic breakout development showing the major principal stress around the breakout, normalised by the vertical *in situ* stress ($\sigma_v$). The far-field stress state is $\{\sigma_v; \sigma_H; \sigma_h\} = \{4{,}060;\ 7{,}500;\ 3{,}045\}$ psi.

Moreover, there is a strong indication that the stress relaxation around the flank of the breakout, particularly near the intersection of the failing zone with the circular hole boundary, is responsible for the relatively constant breakout width throughout the process. As shown in Figure 46, at the flank of the breakout during this intermediate breakout formation, particularly near the intersection of the initial hole with the boundary of the breakouts, the stress becomes less compressive. Around the tip of the progressing breakout, the major principal stress magnitude is about seven-times of the applied vertical *in situ* stress ($\sigma_v$), whereas, around the relaxation zone, the magnitude is only about 2.5-times of the applied *in situ* vertical stress and it is enclosed by zones of relatively higher stress. Consequently, the reduction of the stress concentration causes the Mohr circle to shrink and, hence, move away from the failure line, which leads to a more stable structure around the flank. The point indicated by the black circle in Figure 46 corresponds to the purple Mohr circle in the inset at the top right of the figure. The direct consequences of these phenomena are: (1) although the shear failure propensity near the tip of the breakout increases, the affected area becomes smaller, and (2) the stress relaxation around the flank improves the stability of the structure in that the high strain energy gets localised into a smaller region near the tip, which is responsible for the relatively constant width as the breakout develops. This observation is consistent with the observations of Zheng *et al*. (1989), who concluded that breakout will not widen, but instead deepens into the formation.

It is now obvious that breakout development has a strong dependence on the stress state around the hole. Therefore, it is tempting to investigate their relations with the magnitude of the *in situ* stress. In practice, estimating the magnitude of the minimum horizontal stress ($\sigma_h$) can be achieved from a mini-fracturing test or extended leak-off test (see, for example, White *et al*. (2002) and Addis *et al*. (1998)) and the task is arguably more straightforward than estimating the magnitude of the maximum horizontal stress ($\sigma_H$). Many efforts have been directed towards finding the relationship between maximum horizontal stress and breakout geometry, particularly its width.

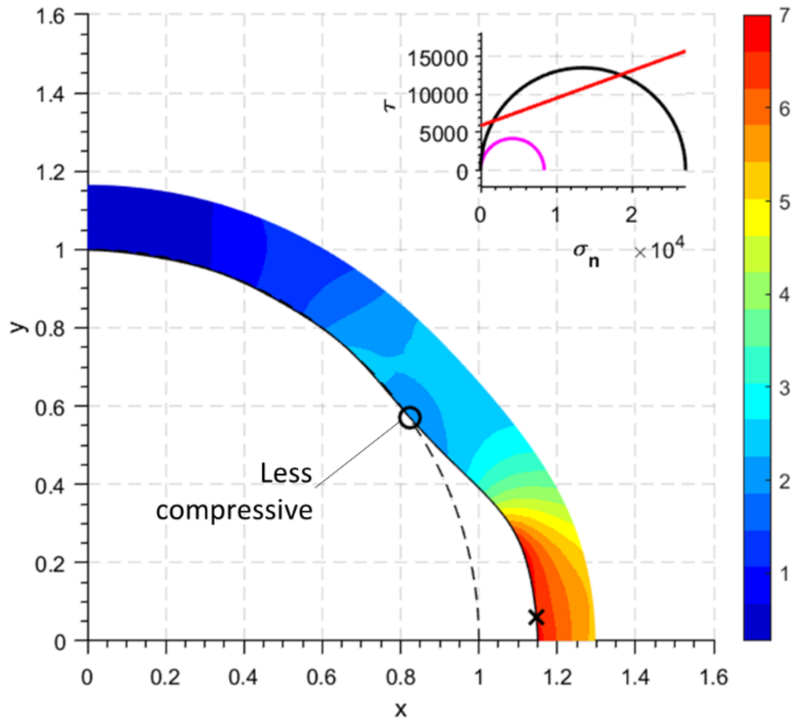


Figure 46. The major principal stress ($\sigma_1$) around the breakout normalised by the vertical *in situ* stress ($\sigma_v$). The black-circle indicate the stress relaxation at the flank of the breakout as it progresses. The figure is a snapshot of a progressing breakout development.

### 6.1.3. *Correlation between in situ stress and breakout geometry*

Simulations were also conducted for three different values of the minimum horizontal stress: $\sigma_h = \{3{,}045;\ 4{,}060;\ 5075\}$ psi, in each case assuming the same rock strength properties. The vertical stress ($\sigma_v$) was set at 1,015 psi higher than the minimum horizontal stress ($\sigma_h$), while the maximum horizontal stress ($\sigma_H$) was varied to cover a wide range of stresses leading to borehole breakout for the given rock properties. The correlation between the breakout width ($\theta_{bo}$) and depth ($r_{bo}$) is shown in Figure 47 for two different failure criteria. The experimental results of Herrick & Haimson (1994) are also shown as the black squares and grey triangles, respectively, in the same figure.

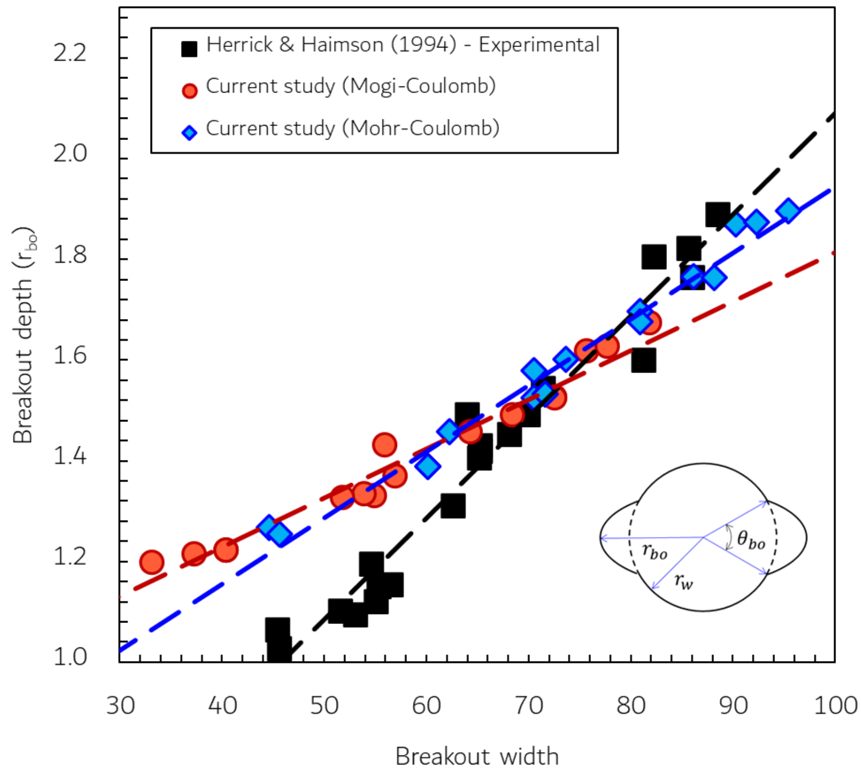


Figure 47. The correlation between the breakout width ($\theta_{bo}$) and breakout depth ($r_{bo}$). The experimental results of Herrick & Haimson (1994) are shown as the black squares.

As shown in Figure 47, the model predicts the correct trend but not quite the right slope compared with the experimental results of Herrick & Haimson (1994). It is important to note that in their numerical modeling, Herrick and Haimsom (1994) used a rock strength scaling factor for each episode of the breakout progression to mimic the experimental data. It is, therefore, reasonable that their numerical result produced a shallower breakout for the same width. Figure 47 is useful for a consistency check of the method proposed in this research. A more interesting plot for *in situ* stress estimation is to see the relation between breakout geometry and *in situ* stress. For the case considered here, the correlation of maximum horizontal stress with breakout depth and width from the numerical simulation is encouraging, as shown in Figures 48a and 48b, respectively. As seen, however, the experimental data are more scattered than the numerical simulations. The slightly scattered result in the numerical simulation is inevitable and related to the conformal mapping procedure that involves numerical calculations to approximate the actual shape of the hole boundary.

The following exercise can be done to check the consistency of the experimental data and the numerical simulations. Consider the left-most point from Herrick & Haimson (1994) experimental data in Figure 48a. This data point coressponds to breakout depth ($r_{bo}$) of 1.2 with an actual maximum horizontal stress ($\sigma_H$) of 7240 psi. If this data point is fitted to the best-fit trendline of the actual experimental data (black line), the estimated maximum horizontal stress ($\sigma_H$) is 8654 psi; this estimation corresponds to an error of 16%. Much of this error in inherently due to variability of the samples or other factors related to the experiment itself. If the same data point is now fitted to the Mohr-Coulomb (blue) and Mogi-Coulomb (red) trendlines, the estimated values are 6635 psi (9.1% error) and 8430 psi (14.1% error), respectively. This individual exercise will be repeated for all data points as such their overall RMS error can be estimated. Although it is understood that the RMS error of the actual trendline (black line) will be less than when the Mohr-Coulomb and Mogi-Coulomb trendlines are used, the comparison among them will somehow reflect the accuracy and consistency of the method. The RMS error of the entire experimental data with respect to the actual best-fit trendline in Figure 48a is 1058.5 psi, whilst the RMS error for the Mohr-Coulomb and Mogi-Coulomb are 1939 psi and 1480 psi, respectively. Thus, lower RMS error is produced by the Mogi-Coulomb trendline; as one can also visually see from Figure 48a.

The same exercise can also be done for breakout width as shown in Figure 48b. The RMS error for the entire dataset based on the actual trendline (black) is 1068 psi. The Mohr-Coulomb and Mogi-Coulomb trendlines will give a RMS error of 1264 psi and 1605 psi, respectively. Thus, for the case of breakout width, it seems that Mohr-Coulomb produces less error than Mogi-Coulomb. Now, it is tempting and seems logical to then expect that a much better estimation, *i.e.* less RMS error, can be obtained if one use the average values of the predicted stress using breakout depth and breakout width. For each data points, if one then takes the average value of the predicted maximum horizontal stress from breakout width and breakout depth, then the RMS error of the actual trendline is 1053 psi. The RMS errors of the Mohr-Coulomb and Mogi-Coulomb trendlines using this hybrid method are 1536 psi and 1362 psi, respectively.

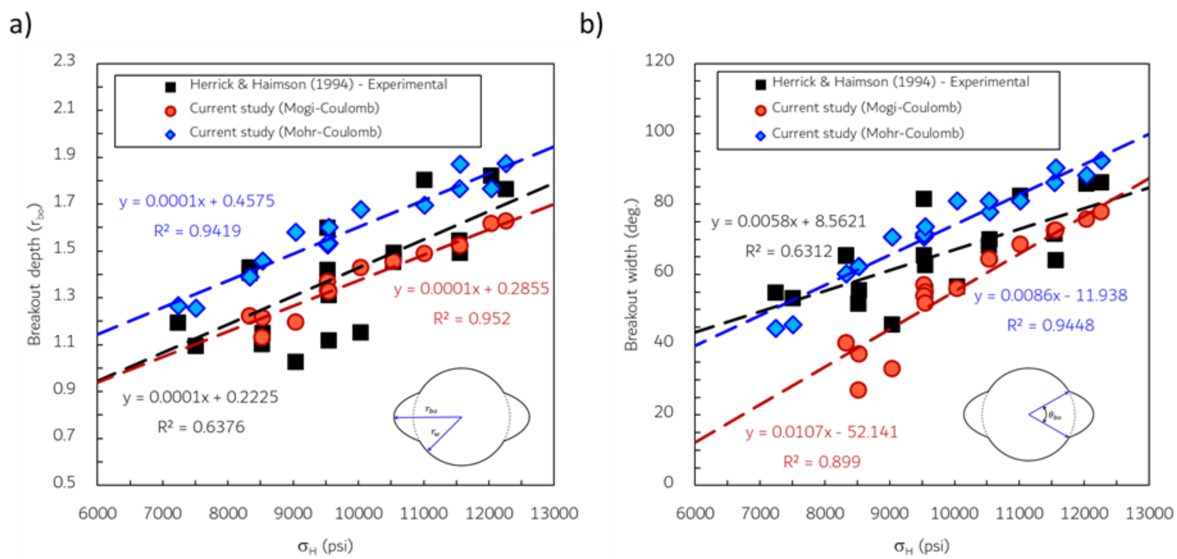


Figure 48. The relationship between maximum horizontal stress and (a) the breakout depth ($r_{bo}$) and (b) the breakout width ($\theta_{bo}$) for all minimum horizontal stress variations. The experimental results from Herrick & Haimson (1994) are also shown, as black squares.

Now, using the same dataset as in Figure 48, if the same results are grouped according to the three levels of minimum horizontal stress ($\sigma_h$) considered here, a better relationship between breakout width and depth with maximum horizontal stress is obtained (Figure 49). It is reasonable to conclude that, because the laboratory experiment was also conducted under a true-triaxial stress state, the experimental data lie closer to that of the Mogi-Coulomb simulation. According to the Mogi-Coulomb failure criterion given in Eq. (15), the critical limit at which shear failure occurs depends on the octahedral shear stress ($\tau_{oct}$) and the effective mean stress ($\sigma_{m,2}$). As seen in Figure 49, it is challenging to isolate solely the influence of the maximum horizontal stress from other factors responsible for the breakout generation.

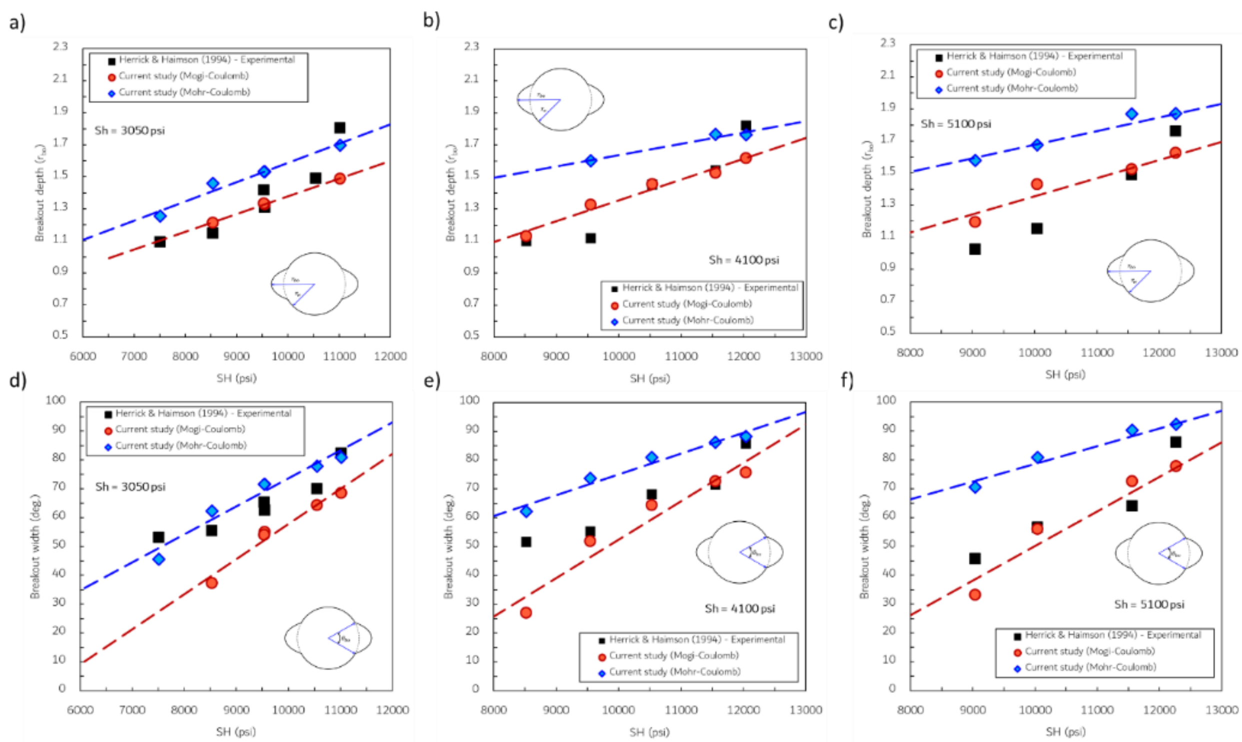


Figure 49. Correlation between the maximum horizontal stress ($\sigma_H$) with (a-b-c) breakout depth ($r_{bo}$) and (d-e-f) breakout width ($\theta_{bo}$), at several minimum horizontal stress magnitudes.

### 6.1.4. *In situ stress estimation based on breakout geometry*

Perhaps the most important question to ask at this stage is whether or not the breakout geometry can be used to infer the magnitude of the *in situ* stress. By rearranging Eq. (15), the critical limit at which shear failure occurs can be represented by the Mogi-Coulomb failure function ($F_{\mathrm{MgC}}$):

$$F_{\mathrm{MgC}} \geq \tau_{oct} - a - b\sigma_{m,2} \tag{168}$$

in which the *in situ* stress and the rock strength properties are embodied within the Mogi-Coulomb failure function ($F_{\mathrm{MgC}}$). The correlation between the Mogi-Coulomb failure function with breakout depth ($r_{bo}$) and with breakout width ($\theta_{bo}$), at several minimum horizontal stress ($\sigma_h$) magnitudes, indicates better correlations (Figure 50). Unlike their correlation with the maximum horizontal stress (Figure 48), the trendlines of the experimental data from Herrick and Haimson (1994) and simulation are now more obvious, *i.e.*, the $R^2$ of the trendline improves.

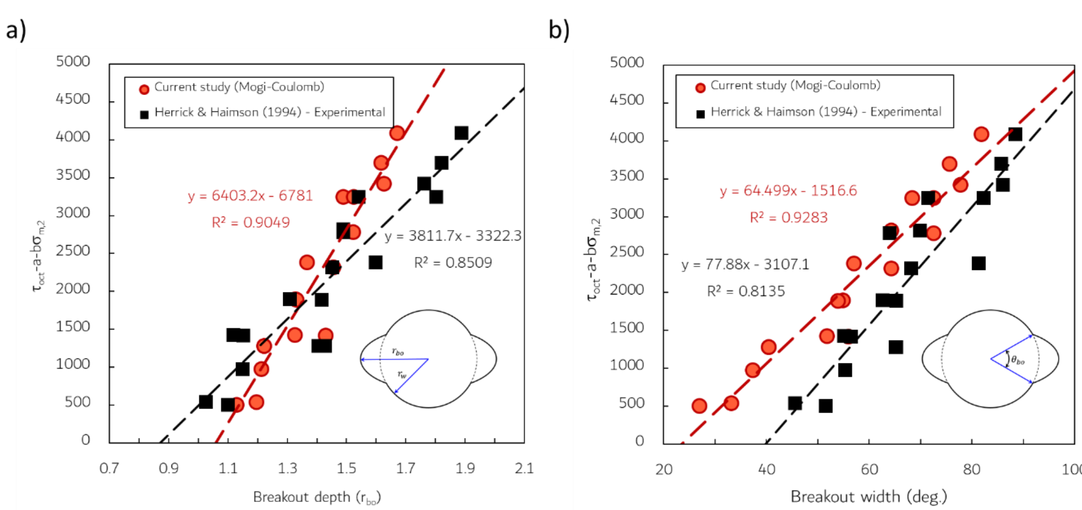


Figure 50. Relationship between the failure function ($F_s$) of Mogi-Coulomb criterion with (a) breakout depth ($r_{bo}$) and (b) breakout width ($\theta_{bo}$).

Similarly, if the Mohr-Coulomb failure criterion is used, then the failure function describing the onset of shear failure ($F_{\mathrm{MC}}$) can be obtained by rearranging Eq. (12), as follows:

$$F_{\mathrm{MC}} \geq \tau - S_o - \mu\sigma_n \tag{169}$$

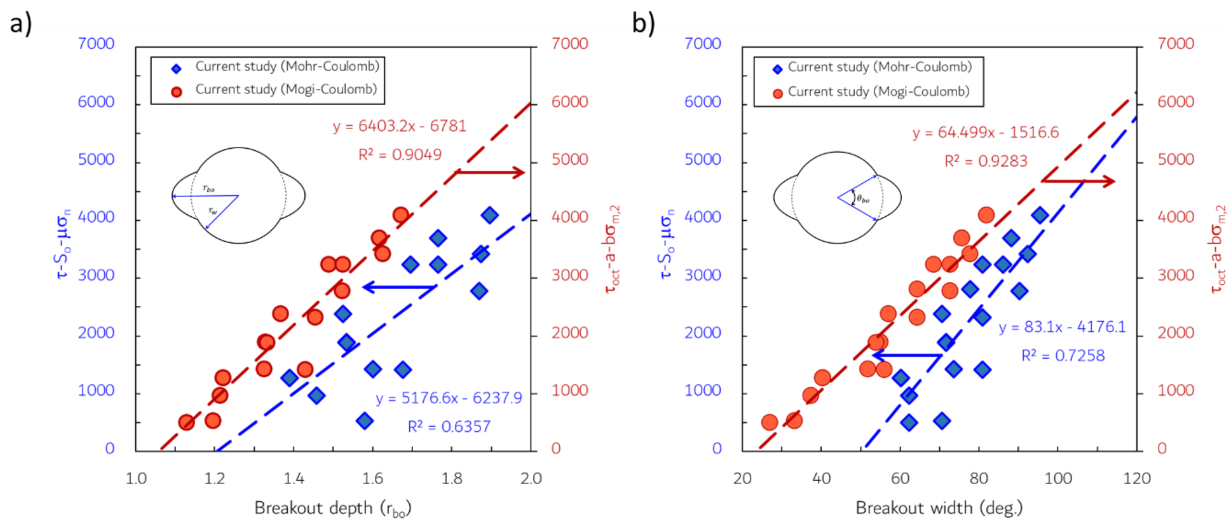


Figure 51. Relation between the Mogi-Coulomb failure function (red) and the Mohr-Coulomb failure function (blue) with (a) breakout depth ($r_{bo}$) and (b) breakout width ($\theta_{bo}$). The Mogi-Coulomb and Mohr-Coulomb functions correspond to the right and left axis, respectively.

From Figure 51, it is reasonable, at this point, to conclude that the Mogi-Coulomb failure function ($F_{\mathrm{MgC}}$) is better than Mohr-Coulomb in describing the relationship between breakout geometry and *in situ* stress. Although the correlation with the maximum horizontal stress is only implicit, in that the mathematical relation is somewhat "hidden" within the complicated failure functions formulation, it is conceivable that its magnitude can be estimated if the magnitude of the vertical stress ($\sigma_v$), the minimum horizontal stress ($\sigma_h$), and the Coulomb strength parameters ($S_o$ and $\mu$) are known. In other words, if the relationship between breakout geometry and the failure function is known, and if the magnitude of the $\sigma_v$ and $\sigma_h$ are also known, then for a given rock strength, the maximum *in situ* stress ($\sigma_H$) can be inferred.

Now, considering the Mogi-Coulomb failure function, to quantitatively examine the applicability of breakout geometry to infer *in situ* stress for a given breakout width or depth, Eq. (168) can be expanded by utilising the definition of $\sigma_{m,2}$ and $\tau_{oct}$. Following the expansion of $\sigma_{m,2}$ and $\tau_{oct}$ in terms of principal stresses in Eq. (168), *i.e.* $\sigma_{m,2} = \frac{1}{2}(\sigma_1 + \sigma_3)$ and $\tau_{oct} = \frac{1}{3}\sqrt{(\sigma_1 - \sigma_2)^2 + (\sigma_2 - \sigma_3)^2 + (\sigma_1 - \sigma_3)^2}$, and after some algebraic manipulation, the following quadratic polynomial can be obtained:

$$\sigma_1^2\left(\frac{9}{4}b^2 - 2\right) + \sigma_1\left(2\sigma_2 + 9ab + 9F_{\mathrm{MgC}}b\right) + \left(9F_{\mathrm{MgC}}^2 + 18F_{\mathrm{MgC}}a + 9a^2 - 2\sigma_2^2\right) = 0 \qquad (170)$$

In the equation shown above, the constants $a$ and $b$ are taken from Eq. (17), and $F_{\mathrm{MgC}}$ is also known from the trendline in Figure 51. For a vertical wellbore, $\sigma_2 = \sigma_z$ and in the case considered here $\sigma_3 = 0$, hence, the only unknown is $\sigma_1$, which is the tangential stress ($\sigma_\theta$) at the wellbore wall.

An exercise for a consistency check of the method is shown in Table 6 in which the breakout geometry obtained from the simulation in this study is used to infer the value of $\sigma_H$. The RMSE and the percentage difference between the applied (actual) and predicted $\sigma_H$ is calculated using the following formula:

$$\mathrm{RMSE} = \sqrt{\sum_{i=1}^{N}\frac{(\sigma_{H_{prediction},i} - \sigma_{H,i})^2}{N}} \qquad (171)$$

$$\Delta = \frac{\sigma_{H_{prediction}} - \sigma_H}{\sigma_H}$$

and the results are given in Table 6. If the breakout width is used to estimate the maximum *in situ* stress ($\sigma_H$), then the overall prediction will have an RMSE of 327.5 psi. The predictability of the method to infer the actual maximum *in situ* stress ($\sigma_H$) is also shown in Figure 51. The scattered observed in Figure 51 is merely due to the numerical procedure involves in the proposed method. In actual situations, other factors such as uncertainty of the *in situ* stress and heterogeneity of the rocks may also influence the predictability of the method. It is also important to note that the case considered here is for a vertical wellbore. In the case of a wellbore whose long axis is not coincident with one of the principal *in situ* stresses, then the relationship between the near-wellbore stress and the *in situ* stress will be more complex.

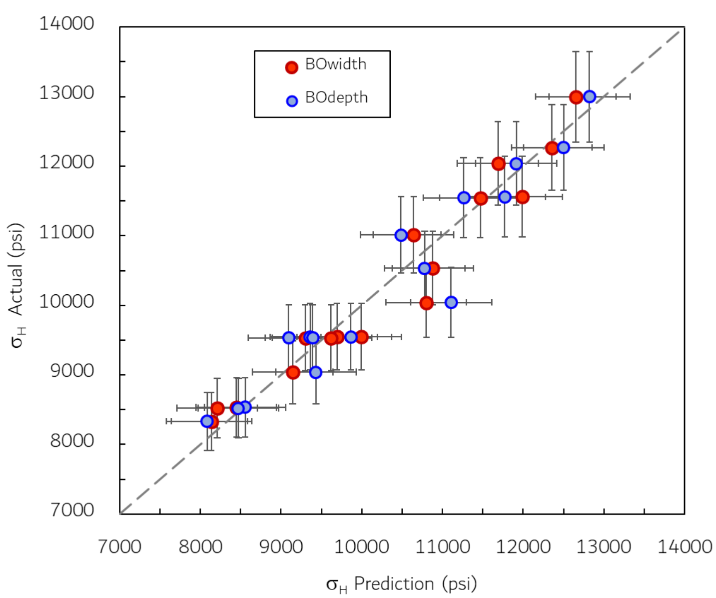


Figure 52. Comparison between actual and predicted maximum *in situ* stress ($\sigma_H$). The red and blue dots represent the result obtained from breakout width and depth, respectively. An error bar of $\pm$5% is shown for each point.

Table 6. Calculation of maximum *in situ* stress ($\sigma_H$) from breakout geometry based on the Mogi-Coulomb failure criteria.

| $\sigma_h$ (psi) | $\sigma_H$ (psi) | Breakout width ($\theta_{bo}$) | Breakout depth ($r_{bo}$) | $a$ (-) | $b$ (-) | $\sigma_H$ prediction (psi) (Estimated using) | | | |
|---|---|---|---|---|---|---|---|---|---|
| | | | | | | Breakout width ($\theta_{bo}$) | Δ | Breakout depth ($r_{bo}$) | Δ |
| 2030 | 8334 | 40 | 1.22 | 5209.4 | 0.32 | 8137 | -2.4% | 8083 | -3.0% |
| 2030 | 9534 | 57 | 1.37 | 5209.4 | 0.32 | 9300 | -2.5% | 9097 | -4.6% |
| 3045 | 8534 | 37 | 1.21 | 5209.4 | 0.32 | 8448 | -1.0% | 8556 | 0.3% |
| 3045 | 9547 | 55 | 1.33 | 5209.4 | 0.32 | 9694 | 1.5% | 9361 | -1.9% |
| 3045 | 9534 | 54 | 1.33 | 5209.4 | 0.32 | 9621 | 0.9% | 9390 | -1.5% |
| 3045 | 11014 | 68 | 1.49 | 5209.4 | 0.32 | 10642 | -3.4% | 10485 | -4.8% |
| 4060 | 8521 | 27 | 1.13 | 5209.4 | 0.32 | 8210 | -3.6% | 8472 | -0.6% |
| 4060 | 9547 | 52 | 1.33 | 5209.4 | 0.32 | 9996 | 4.7% | 9866 | 3.3% |
| 4060 | 10534 | 64 | 1.46 | 5209.4 | 0.32 | 10880 | 3.3% | 10779 | 2.3% |
| 4060 | 11547 | 73 | 1.52 | 5209.4 | 0.32 | 11467 | -0.7% | 11263 | -2.5% |
| 4060 | 12040 | 76 | 1.62 | 5209.4 | 0.32 | 11687 | -2.9% | 11914 | -1.0% |
| 5075 | 9041 | 33 | 1.20 | 5209.4 | 0.32 | 9146 | 1.2% | 9433 | 4.3% |
| 5075 | 10041 | 56 | 1.43 | 5209.4 | 0.32 | 10800 | 7.6% | 11107 | 10.% |
| 5075 | 11560 | 73 | 1.52 | 5209.4 | 0.32 | 11986 | 3.7% | 11772 | 1.8% |
| 5075 | 12267 | 78 | 1.63 | 5209.4 | 0.32 | 12355 | 0.7% | 12500 | 1.9% |
| 5075 | 13000 | 82 | 1.67 | 5209.4 | 0.32 | 12650 | -2.7% | 12821 | -1.4% |
| | | | | | | RMSE = 327.5 psi | | RMSE = 377 psi | |

Despite the fact that the results are encouraging, it is important to note that all of the simulations discussed above are based on the assumption of a constant *in situ* stress, but ignore other factors that might also influence the geometry of breakouts, such as drill pipe, erosion, *etc*. Unlike in the laboratory, the subsurface is more dynamic, and having a fully-controlled downhole condition will be challenging, if not impossible. It has been seen that the stress state around the hole greatly influences the final breakout geometry. The latest downhole imaging technology, for instance by means of ultrasonic waves or resistivity impedance, enables practitioners to capture the detailed wellbore features, including wellbore elongation and enlargement. The final breakout geometry tested under controlled parameters in the laboratory seems to be very ideal, and is rarely observed in actual downhole conditions. The actual hole geometry can be extremely irregular (see for example the breakout shapes presented by Plumb & Hickman (1985), Zoback *et al*. (1985), and Huber *et al*. (1997)) and an ideal cusp or dog-eared shaped breakout is extremely rare. Fluctuations of wellbore pressure, as well as thermal and chemical factors, will perturb the stress state near the wellbore wall and, hence, will influence the final breakout geometry (see for example Valley *et al*. (2018) and Moore *et al*. (2012)). Therefore, the breakout that is used for estimating the *in situ* stress is only that produced by the stress-induced phenomena, *e.g.* one must exclude hole enlargement due to drill-string vibration or erosion.

## 6.2. Near-wellbore stress profiling using ultrasonic imaging tools

Borehole imaging plays a central role in reservoir description and characterisation. Modern borehole imaging tools provide a high-resolution image of the wellbore wall through optical technologies, electrical resistivity or acoustic reflectivity (Prensky, 1999). Acoustic-based borehole imaging tools consist of a rotating piezoelectric transducer that operates at ultrasonic frequency. The transducer measures the traveltime and amplitude of the acoustic pulse reflected off the borehole wall. The acoustic traveltime is affected by the density of the borehole fluid and used to reconstruct the borehole image and geometry. The ultrasonic borehole imaging tool can provide 360° coverage of open hole wellbores filled with either water-based or oil-based drilling mud.

Ultrasonic borehole data allows practitioners to detect the presence of fractures and other geological features, and conduct analysis of wellbore stability phenomena such as breakout and drilling-induced fractures. Ultrasonic borehole imaging technology has also been used by many researchers to infer the least principal stress direction, such as Bagdeli *et al*. (2019), Huber *et al*. (1997), Maxwell (2014), McLellan & Cormier (1996), Plumb (1990), Plumb & Hickman (1985), Schmitt *et al*. (2012), Valley *et al*. (2018), Willson *et al*. (2007), Zoback *et al*. (2003), (1985). Zhang *et al*. (2019) investigated the potential misinterpretation of breakdown pressure from hydraulic fracturing in a borehole with breakout and concluded that the difference with that of a perfectly-circular wellbore could be as large as 82%.

In this research, another potential utilisation of ultrasonic data to obtain the in-plane near-wellbore stress around the wellbore circumference is investigated. In addition to the standard geomechanical properties such as the *in situ* stress and the rock mechanical properties, the benefit of an ultrasonic data can be further leveraged: (1) to provide accurate near-wellbore stress computation without making any assumption regarding the wellbore geometry and (2) to serve as an input for various post-drill wellbore operations such as hydraulic fracturing, cementing, and perforation where a detailed knowledge about the near-wellbore stress is crucial. It is anticipated that the results could potentially improve various designs that require the knowledge of near-wellbore stress. As detailed in Chapter 5, in which a semi-analytical method is proposed to compute the in-plane stress for irregularly-shaped holes, the utilisation of the ultrasonic borehole data does not require any extra processing apart from exporting the wellbore radius produced by the tools. It is envisaged that any downhole measurement tools can also be used if the wellbore geometry can be reconstructed.

A dataset from the *Western Australian Petroleum and Geothermal Information Management System* (WAPIMS) can be used to substantiate the value of the proposed method. The WAPIMS provides released data and all public information arising out of petroleum exploration activities within Western Australia's State jurisdiction (onshore and State territorial waters) together with Commonwealth offshore activities released prior to 1 January 2012. The complete dataset can be accessed through https://wapims.dmp.wa.gov.au/WAPIMS.

A total of 180 data points were obtained at each depth from the ultrasonic borehole imaging data. This will give a 2° azimuthal resolution of wellbore circumference that can sufficiently capture any local irregularities that may exist around the wellbore wall. At each depth, an iterative procedure of conformal mapping is performed to obtain the most appropriate mapping constants $m_k = \alpha_k + i\beta_k$. The in-plane stress can then be obtained. The process is repeated for each depth. The amount of computation time for each depth with 180 data points is less than a second, which, in this work was run using a laptop DELL Inspiron 5459 Intel i5-6200U with 8GB RAM.

To demonstrate the impact of wellbore geometry on the in-plane stress computation, the following assumption is made regarding the *in situ* stress around the wellbore: the vertical *in situ* stress ($\sigma_v$) is assumed to be 10,000 psi with 7000 and 9000 psi for minimum ($\sigma_h$) and maximum ($\sigma_H$) horizontal stresses, respectively. The azimuth of the minimum horizontal stress is parallel to the North. (It is worth noting that a proper geomechanical analysis should be conducted to obtain the *in situ* stress state in the area, which in this exercise was not conducted.)

The actual hole geometry shown in Figure 53 shows substantial hole enlargement. The average hole radius over this section is approximately 5 inch with a maximum radius up to 6 inches in comparison to the actual bit size of 8.5 inches (4.25-inch radius). The area of the hole enlargement is nearly 40% larger than that of a circular wellbore. Hence, any stress computation that assumes a circular wellbore, *e.g.* using the Kirsch equation, would be erroneous.

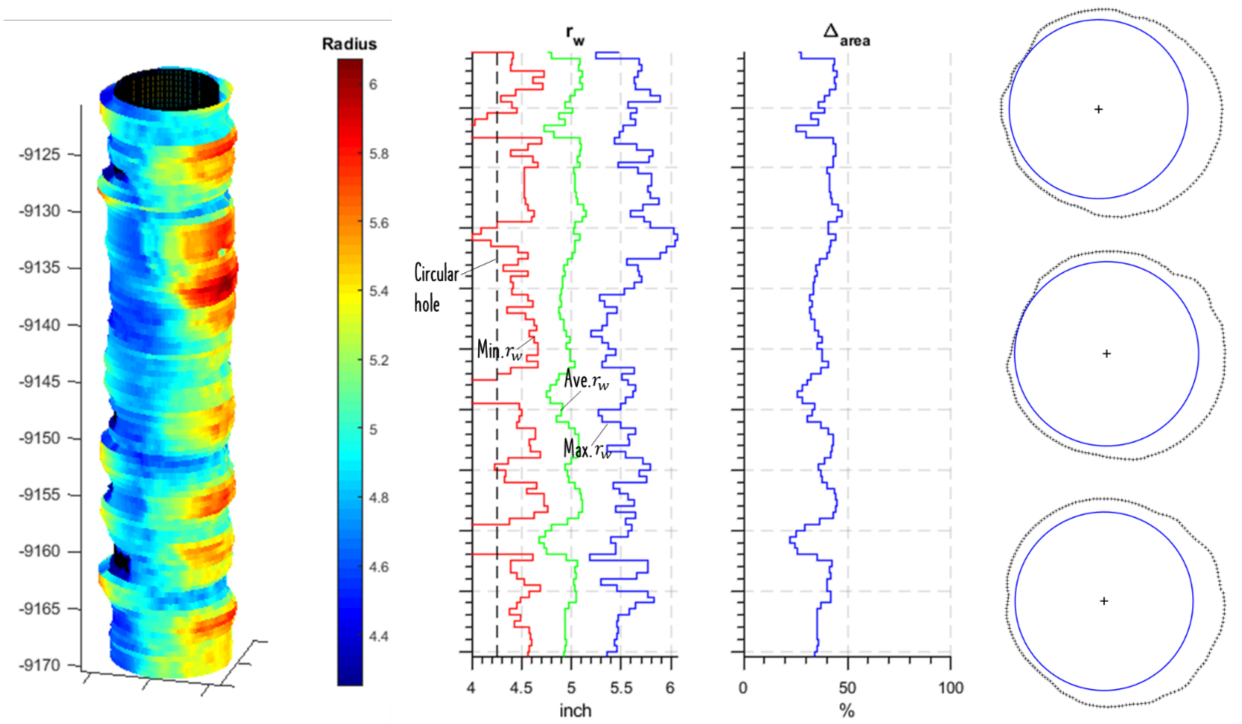


Figure 53. The actual wellbore geometry reconstructed from the ultrasonic imaging tools. The irregularities of the wellbore is illustrated by hole geometry at three depth points shown on the right.

Three depth points have been taken for further stress computation. The hole shape at these depths is completely irregular. The conformal mapping of the first hole shape is shown in Figure 54 in which the external region of hole in *z*-plane is conformally mapped into the region outside of the unit circle in the $\xi$-plane. The tangential stress ($\sigma_\theta$) around the three holes indicates that the stress concentration is not only controlled by the *in situ* stress but also the geometry of the hole. This example emphasizes the importance of incorporating the actual geometry, wherever possible, in computing the in-plane stress.

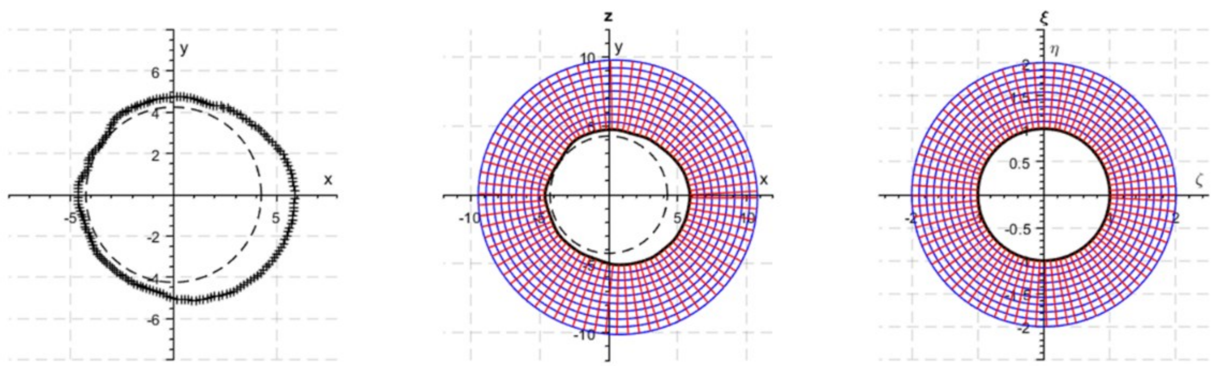

Figure 54. The actual hole showing 180 data points around the circumference and the conformal mapping from the $z$-plane into $\xi$-plane.

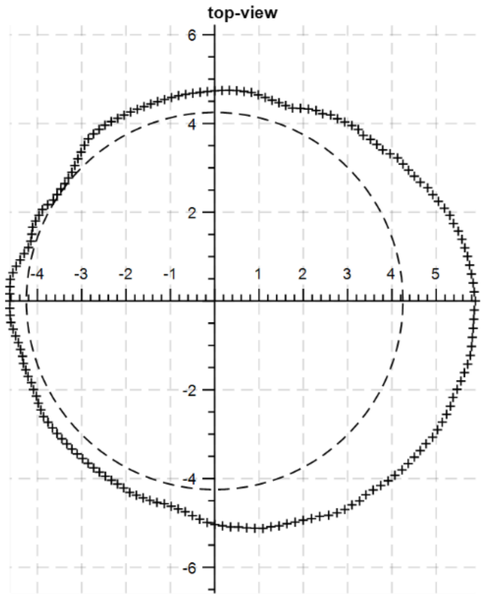


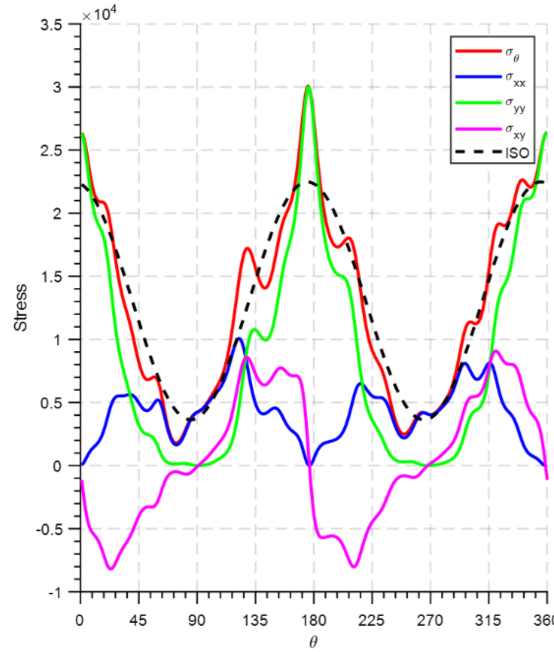


Figure 55. The near-wellbore stress components at the wellbore wall of the first hole geometry. The black-dash curve shows the tangential stress ($\sigma_\theta$) computed using the Kirsch equation assuming a circular hole; which should be compared with the red curve.

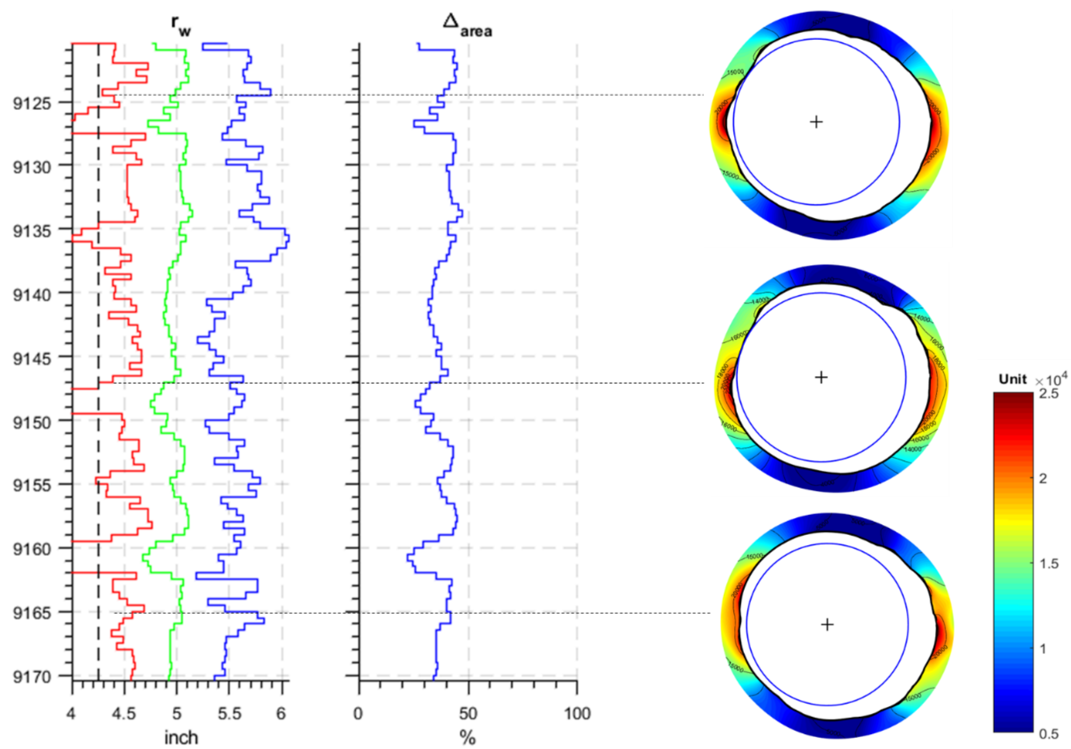


Figure 56. The tangential stress ($\sigma_\theta$) around the holes indicates that the stress concentration is not only controlled by the *in situ* stress but also the geometry of the hole.

To further investigate the significance of the hole geometry on the near-wellbore stress, the stress will be computed along 100 ft of open hole section using the actual wellbore geometry. The unwrapped profile of the hole geometry is shown in the second track of Figure 57, which consist of 18,000 data points, *i.e.* 100 ft of open hole with 180 data points at each depth. Notice that a severe hole enlargement is observed near the bottom of the wellbore with a maximum radius of 6.0 inch and an average of 4.7 inches, in comparison with the original 4.25 inch of the drill bit radius. Over this section of the wellbore, the inclination is around 40° towards N 280° E. A similar process of finding appropriate conformal mapping coefficients was deployed and repeated at each depth.

To obtain the near-wellbore stress over this section, the processing time is approximately 120 seconds using only a DELL Inspiron 5459 Intel i5-6200U laptop with 8GB RAM.

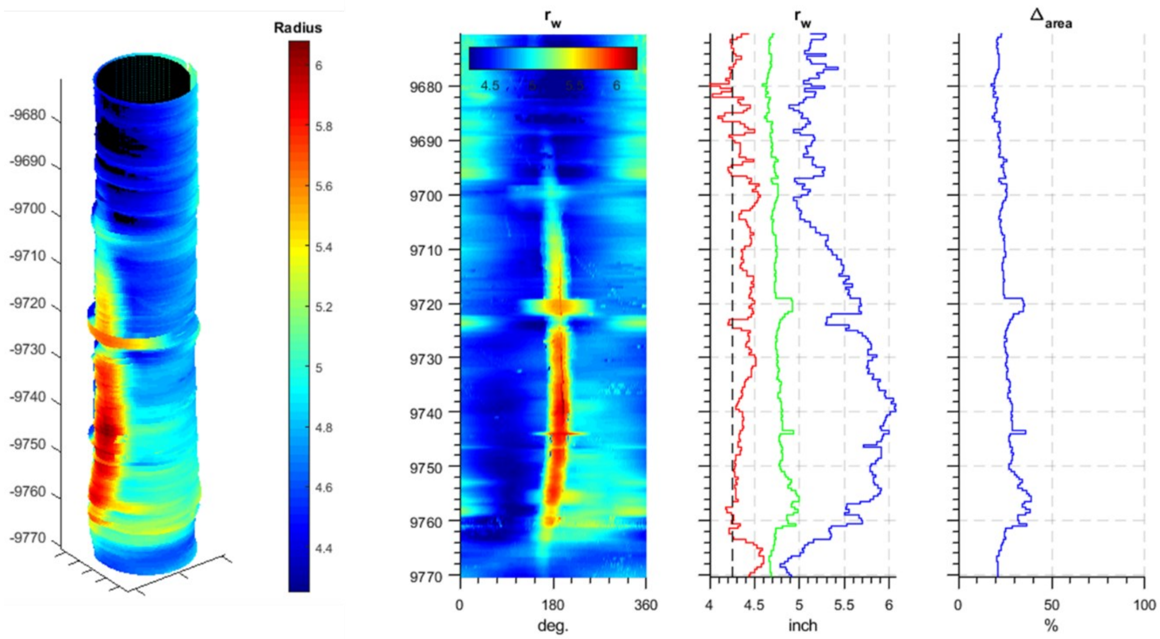


Figure 57. Hole geometry from the ultrasonic data around an inclined section of the wellbore. The case is assuming an isotropic rock with *in situ* stress condition $\{\sigma_v;\ \sigma_H; \sigma_h\} = \{10{,}000; 9000; 7000\}$.

The tangential stress around the wellbore corresponds not only with the relative orientation of the *in situ* stress, but also the cross-sectional geometry of the wellbore throughout the open hole section (Figure 58). Detailed analyses on the tangential stress around the wellbore indicates that the percentage difference of the maximum tangential stress may reach up to 50% with that of the Kirsch equation (Figure 59). This is mainly due to the influence of the hole geometry which cannot be captured if one uses the Kirsch equation. Similarly, the difference of the minimum tangential stress is also substantial, *i.e.* approximately 25% with a maximum of 50% over a certain interval.

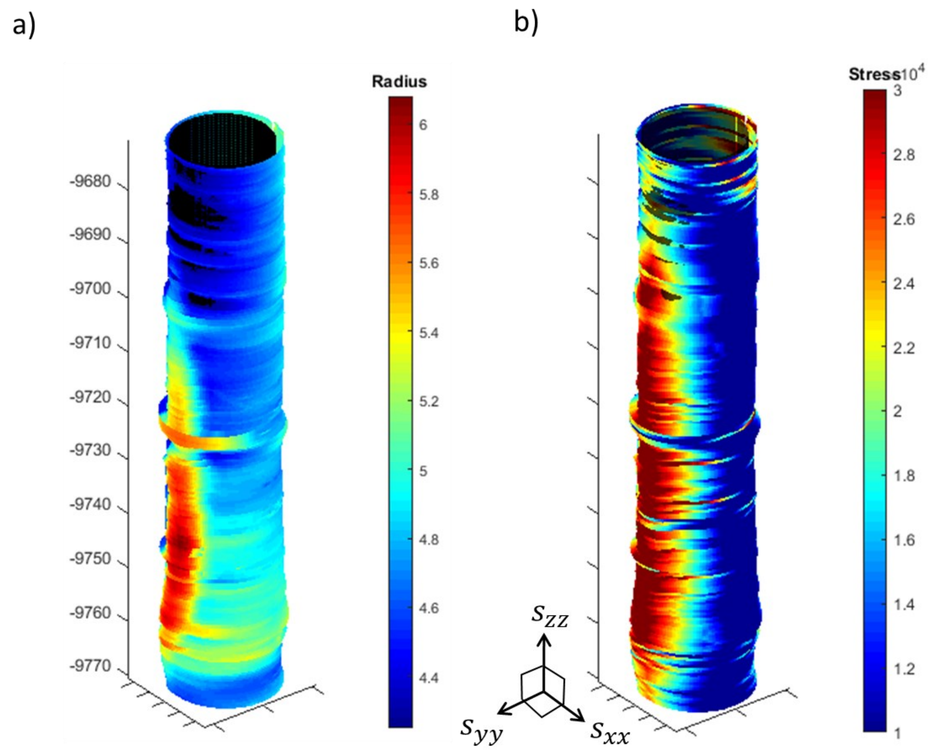


Figure 58. (a) The actual wellbore geometry from the ultrasonic data and (b) the computed tangential stress ($\sigma_\theta$). The case is assuming an isotropic rock with *in situ* stress condition $\{\sigma_v;\ \sigma_H; \sigma_h\} = \{10{,}000; 9000; 7000\}$.

In practice, many post-drill wellbore operations will require detailed knowledge about the near-wellbore stress such as sidewall coring, perforation, hydraulic fracturing and completion design. Although the influence of the near-wellbore stress may be insignificant as compared to the size of the created fractures, which may reach hundreds of feet, having an upfront and accurate analysis is still essential during the design stage of the operation. It is then crucial to consider the actual wellbore geometry in computing the near-wellbore stress if data availability permits, *e.g.* through ultrasonic data as shown in Figure 58 or other data sources that allow the reconstruction of the actual wellbore cross-section.

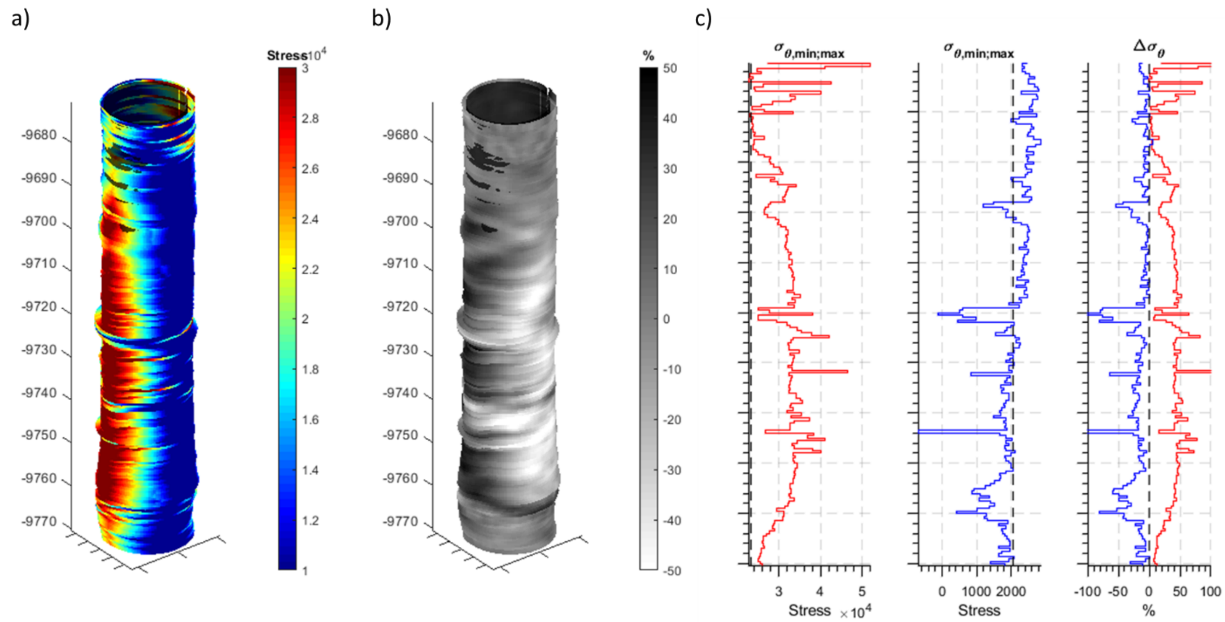


Figure 59. (a) The computed tangential stress ($\sigma_\theta$) and (b) the percentage difference of $\sigma_\theta$ with that of the Kirsch equation showing the effect of the wellbore geometry. (c) The maximum and minimum tangential stress at each depth and the percentage difference with the Kirsch equation. The case is assuming an isotropic rock with *in situ* stress condition $\{\sigma_v;\ \sigma_H; \sigma_h\} = \{10{,}000; 9000; 7000\}$.

# Chapter 7 Summary and Recommendations

## 7.1. Summary

Some reservoir rocks, notably shales, are intrinsically anisotropic, and their physical properties, such as strength and deformability, will depend on the orientation of the rock with respect to the principal stresses. For the case of anisotropic wellbore stability modelling, variations of the near-wellbore stress with rock elastic anisotropy, the far-field stress state, and the relative orientation of the wellbore to the bedding plane, are important aspects in examining the stability of the wellbore which should be included in any analyses.

To comprehensively examine the dependency of the rock anisotropic behaviour and the wellbore instability propensity, the three-dimensional stress components at the wellbore wall were calculated using the Lekhnitskii-Amadei solution. With regards to the effect of elastic anisotropy, it was found that a higher degree of rock elastic anisotropy appears to induce higher stress concentration. The difference with that of the isotropic case could reach 25% for the highest degree of anisotropy assumed in the case considered in this research. The findings emphasize not only that considering intermediate stress is of great importance, but more importantly, neglecting elastic anisotropy would also affect the breakout pressure attributed to the reduction of the tangential stress and axial stress by approximately 5% and 35%, respectively.

Moreover, the use of Mogi-Coulomb criterion allows the onset of the intact rock shear failure to be predicted accounting for all three principal stresses. It is demonstrated that the inclusion of the intermediate stress embedded in the Mogi-Coulomb criterion is responsible for reducing the breakout limit. By incorporating the anisotropic strength behaviour using the Jaeger plane of weakness concept, it has been shown that the influence of weak bedding planes diminishes when the relative angle between the wellbore axis and the bedding normal is low. In practical engineering design, this suggests that wells drilled sub-parallel through a fracture or fault are less stable than those drilled at an oblique angle. In the case considered in this research, the risk posed by the weak bedding plane might be masked by the isotropic assumption. Thus, it is of paramount importance to have a more robust modelling approach to improve the drilling design, for instance, by way of optimizing the mud weight design and obtaining a more favourable drilling direction considering the strength anisotropy of the rocks. The wellbore stability model developed in this work can account for both effects, *i.e.* the intact rock failure governed by either Mohr-Coulomb or Mogi-Coulomb failure criteria and also the plane of weakness governed by the Jaeger plane of weakness concept.

The second objective of the research is concerned with the stress calculation around an arbitrary hole of given contour in isotropic or anisotropic media. In this research, a new semi-analytical method has also been presented in which the stress distribution around an arbitrary cross-sectional hole is calculated by coupling the graphical conformal mapping of Melentiev, with the complex stress potential method of Kolosov-Muskhelishvili. A new representation of the stress potentials has been proposed which depends on the conformal mapping constants obtained using Melentiev's iterative procedure. The method allows the calculation of the in-plane stress components around an arbitrary hole for any given contour shape, in isotropic or anisotropic media. Validation against several known results has been carried out for a wide range of hole shapes and anisotropic materials, including non-symmetrical and irregular shape such as wellbore breakouts. The methodology has also been shown to yield accurate stresses away from the hole boundary. The method, therefore, provides a unified and accurate approach for studying the effect of hole geometry on the stress distribution around holes in isotropic or anisotropic materials, and should be particularly useful for irregularly-shaped holes that are not symmetrical or quasi-polygonal. In this research, the method has been used for two purposes: (1) to model the breakout development and then infer the magnitude of the *in situ* maximum horizontal stress; and (2) to compute the near-wellbore stress using ultrasonic imaging tool.

In the breakout development modelling, the semi-analytical method allows the geometry stabilization and the stress evolution throughout the process to be tracked. The simulation performed in the current study produced a cusp or dog-eared shaped breakout, as observed by several researchers. The orientation of the breakout propagation is consistent with the direction of the least principal stress. It is observed that the stress at the flank of the breakout, particularly near the intersection of the initial hole with the boundary of the breakouts, becomes less compressive as the breakout progresses. This stress relaxation around the flank improves the stability of the surrounding rock, and hence is responsible for the relatively constant width as the breakout deepens. Moreover, although the shear failure propensity near the tip of the breakout increases, the affected area becomes smaller as the breakout tip sharpens and deepens; the stress concentration becomes more localized around the tip with increasing magnitude.

Perhaps the most important question to ask is whether or not the breakout geometry can be used to infer the magnitude of the *in situ* stress. For this purpose, it is found that the correlation between breakout geometry with *in situ* stress can be improved if plotted against the failure function of the Mogi-Coulomb failure criterion. This implies that, although the correlation is only implicit with the maximum horizontal stress, its magnitude can be estimated if the magnitude of the vertical stress, the minimum horizontal stress, and the Coulomb strength parameters, are known.

The proposed method has also been used to compute the near-wellbore stress around an actual wellbore geometry utilising ultrasonic data. It provides an accurate near-wellbore stress profile without making any assumption regarding the wellbore geometry and could serve as an input for various post-drill wellbore operations such as hydraulic fracturing, cementing and perforation, where a detailed knowledge about the near-wellbore stress is crucial.

## 7.2. Recommendations

The presence of anisotropy will increase the complexity of the computation and modelling, although many practioners realise that the near-wellbore stress can be substantially different than that of isotropic rocks as shown in Chapter 3 and Chapter 4. In addition to that, solutions presented in this research requires additional datasets to characterize the elastic and strength properties of the rocks, *i.e.* the vertical and horizontal elastic property, and also the strength of the weak bedding plane. A comprehensive report of the technique to obtain such dataset in the laboratory was presented by Ambrose (2014) who extensively conducted rock mechanics testing on Vaca Muerta shale and Bossier shale. Given possible practical applications of the methods, it is recommended to implement the method on actual field data, so that, its consistency with the actual drilling events can be validated.

In practical wellbore stability analysis, solutions presented in this research would be more beneficial if one can obtain the continuous profile of the elastic properties from downhole measurements such as acoustic logging tools. One possible source of data is the dipole sonic tool, from which the tangential and lateral elastic properties can be obtained, *e.g.* see for instance Walsh *et al*. (2008) and Chesnokov *et al*. (2010), or that of Prioul *et al*. (2016) who used drill cuttings to determine the anisotropic elastic properties. However, while the acoustic logging data can provide the continuous value of the elastic property, obtaining the continuous profile of the rock strength anisotropy is even more challenging. Most of the methods currently available to estimate the rock strength are based on an empirical equation that is only adequate for a certain type of rocks, see for example Khaksar *et al*. (2009). The ultimate value of the analysis can be achieved if a continuous profile of the stability curve can be constructed, instead of just a single depth analysis as presented in this research. Such development would improve the design and analysis of completion, perforation, hydraulic fracturing, or even wellbore stability evaluation while realtime data are acquired during drilling. In other words, further research that can estimate the continuous profile of the anisotropic strength of the rocks will enhance the applicability of the method—for instance, by developing a method to find a direct correlation between anisotropic elastic properties with anisotropic strength of a particular rock.

In Chapter 5, a new semi-analytical method to compute the in-plane stress around an arbitrarily-shaped hole has been presented. The proposed method allows the in-plane stress to be computed efficiently without any prior knowledge about the hole shape, hence, it is suitable for examining the near-wellbore stress after the excavation process; as long as the cross-sectional geometry of the hole can be reconstructed. The method presented in this research used ultrasonic data to reconstruct the cross-sectional geometry of the wellbore. However, it is known that ultrasonic data is rarely acquired and, hence, it would be interesting to investigate if the wellbore geometry can still be reconstructed using any standard downhole logging tool; such as a six-arms mechanical caliper. Development of such algorithms will open up tremendous potential for future applications of the methods.

Moreover, the current method is limited for computing the in-plane stress component. This makes the application of the method for wellbore stability analysis limited to a vertical wellbore, *i.e.* if one assumes that the vertical stress is one of the principal stresses, or any wellbore whose direction coincides with one of the principal stresses. For wellbore stability analysis, the magnitude of the principal stress is necessary which, in the case of inclined wellbores, can only be obtained if the anti-plane shear stress on the wellbore face can be computed, see for instance Eq. (76). This is still not possible in the present method due to the plane assumption. Further development is necessary to generalise the formulation as such the anti-plane shear stress can be computed for such irregular cross-sectional hole shape.

# References


Aadnoy, B. S., & Chenevert, M. E. (1987). Stability of Highly Inclined Boreholes (includes associated papers 18596 and 18736). *SPE Drilling Engineering*, 2(04), 364-374.

Aadnoy, B. S. (1988). Modeling of the Stability of Highly Inclined Boreholes in Anisotropic Rock Formations (includes associated papers 19213 and 19886). *SPE Drilling Engineering*, 3(03), 259–268.

Aadnoy, B. S., & Ong, S. (2003). Introduction to special issue on Borehole Stability. *Journal of Petroleum Science and Engineering*, 38(3–4), 79–82.

Aadnoy, B. S., Hareland, G., Kustamsi, A., de Freitas, T., & Hayes, J. (2009). Borehole Failure Related to Bedding Plane. *43rd U.S. Rock Mechanics Symposium & 4th U.S. - Canada Rock Mechanics Symposium,* 28 June-1 July, Asheville, North Carolina, Paper ARMA-09-106.

Addis, M. A., Hanssen, T. H., Yassir, N., Willoughby, D. R., & Enever, J. (1998). Comparison of leak-off test and extended leak-off test data for stress estimation. In *Proceedings of the SPE/ISRM Rock Mechanics in Petroleum Engineering Conference*. Paper SPE-47235-MS.

Al-Ajmi, A. M., & Zimmerman, R. W. (2005). Relation between the Mogi and the Coulomb failure criteria. *International Journal of Rock Mechanics and Mining Sciences*, 42(3), 431–439.

Al-Ajmi, A. M., & Zimmerman, R. W. (2006). Stability analysis of vertical boreholes using the Mogi-Coulomb failure criterion. *International Journal of Rock Mechanics and Mining Sciences*, 43(8), 1200–1211.

Al-Ajmi, A. M. (2006). *Wellbore Stability analysis Based on A New True-Triaxial Failure Criterion*. PhD Thesis, KTH.

Amadei, B. (1983). *Rock Anisotropy and the Theory of Stress Measurements*. Berlin: Springer-Verlag, 1983.

Ambrose, J. (2014). *Failure of Anisotropic Shales under Triaxial Stress Conditions*. PhD Thesis, Imperial College London.

Ambrose, J., & Zimmerman, R. W. (2015). Failure of anisotropic shales under triaxial compression and extension. *13th ISRM International Congress of Rock Mechanics*, 10-13 May 2015, Montreal, Canada. Paper ISRM-13CONGRESS-2015-344.

Ambrose, J., Zimmerman, R. W., & Suarez-Rivera, R. (2014). Failure of shales under triaxial compressive stress. *48th U.S. Rock Mechanics Symposium*, 1-4 June 2014, Minneapolis. Paper ARMA 14-7506.

Aslannezhad, M., Khaksar manshad, A., & Jalalifar, H. (2016). Determination of a safe mud window and analysis of wellbore stability to minimize drilling challenges and non-productive time. *Journal of Petroleum Exploration and Production Technology*, 6(3), 493–503.

Bagdeli, M., Manshad, A. K., Shadizadeh, S. R., Ali, J. A., Gholami, R., Keshavarz, A., & Iglauer, S. (2019). Natural fracture characterization and wellbore stability analysis of a highly fractured southwestern Iranian oilfield. *International Journal of Rock Mechanics and Mining Sciences*, 123, 104101.

Bell, J. S., & Gough, D. I. (1979). Northeast-southwest compressive stress in Alberta evidence from oil wells. *Earth and Planetary Science Letters*, 45(2), 475–482.

Bol, G. M., Wong, S. W., Davidson, C. J., & Woodland, D. C. (1994). Borehole Stability in Shales. *SPE Drilling & Completion*, 9(02), 87-94.

Bradley, W. B. (1979). Failure of inclined boreholes. *Journal of Energy Resources Technology, Transactions of the ASME*, 101(4), 232–239.

Caicedo, H. U., Pribadi, M. A., Bahuguna, S., Wijnands, F. M., & Setiawan, N. B. (2010). Geomechanics, ECD Management and RSS to Manage Drilling Challenges in a Mature Field. *SPE Oil and Gas India Conference and Exhibition*, 20-22 January, 2010, Mumbai. Paper SPE 129158.

Capone, G., Bucari, G., Bahuguna, S., & Setiawan, N. B. (2011). Real-time geomechanics optimizes drilling 4 deep water wells in Kutei and Tarakan basin - Offshore East Kalimantan. *Society of Petroleum Engineers - SPE Asia Pacific Oil and Gas Conference and Exhibition 2011*. Paper SPE 147914-ms.

Chardac, O., Murray, D., Carnegie, A., & Marsden, J. R. (2005). A proposed data acquisition program for successful geomechanics projects. In *SPE Middle East Oil and Gas Show and Conference, MEOS, Proceedings* (pp. 297–312). Paper SPE 93182-ms.

Cheatham, J. B. (1984). Wellbore Stability. *Journal of Petroleum Technology*, 36(06), 889–896.

Chesnokov, E., Bayuk, I. O., & Ammerman, M. (2010). Determination of shale stiffness tensor from standard logs. *Geophysical Prospecting*, 58(6), 1063–1082.

Colmenares, L. B., & Zoback, M. D. (2002). A statistical evaluation of intact rock failure criteria constrained by polyaxial test data for five different rocks. *International Journal of Rock Mechanics and Mining Sciences*, 39(6), 695–729.

Daoust, J., & Hoa, S. V. (1991). An analytical solution for anisotropic plates containing triangular holes. *Composite Structures*, 19(2), 107–130.

Driscoll, T. A., & Trefethen, L. N. (2002). Schwarz-Christoffel Mapping. In *Cambridge Monographs on Applied and Computational Mathematics* (Vol. 8). Cambridge University Press, Cambridge.

Du, W., & Kemeny, J. M. (1993). Modeling borehole breakout by mixed mode crack growth, interaction, and coalescence. *34th U.S. Symposium on Rock Mechanics (USRMS)*, Madison, Wisconsin. Paper ARMA-93-0649.

Duan, K., & Kwok, C. Y. (2016). Evolution of stress-induced borehole breakout in inherently anisotropic rock: Insights from discrete element modeling. Journal of *Geophysical Research: Solid Earth*, 121(4), 2361–2381.

England, A. H. (2003). *Complex Variable Methods*. Dover, Mineola, NY.

Ewy, R. T., Kemeny, J. M., Zheng, Z., & Cook, N. G. W. (1987). Generation and analysis of stable excavation shapes under high rock stresses. *6th ISRM Congress*, Montreal, Canada. Paper ISRM-1987-162.

Exadaktylos, G. E., Liolios, P. A., & Stavropoulou, M. C. (2003). A semi-analytical elastic stress-displacement solution for notched circular openings in rocks. *International Journal of Solids and Structures*, 40(5), 1165–1187.

Exadaktylos, G. E., & Stavropoulou, M. C. (2002). A closed-form elastic solution for stresses and displacements around tunnels. *International Journal of Rock Mechanics and Mining Sciences*, 39(7), 905–916.

Fairhurst, C. (1968). Methods of determining *in situ* rock stresses at great depths: Tech. In *Rep. TRI-68, Mo. River Div. Corps of Eng., Omaha, Nebr*. Missouri River Division, US Army, Corps of Engineers.

Gaede, O., Karpfinger, F., Jocker, J., & Prioul, R. (2012). Comparison between analytical and 3D finite element solutions for borehole stresses in anisotropic elastic rock. *International Journal of Rock Mechanics and Mining Sciences*, *51*, 53–63.

Gala, D. M., York, P., Pritchard, D. M., Rosenberg, S. M., Dodson, J. K., & Utama, B. (2010). Drilling Hazard Mitigation Technologies Key in Eliminating Non-Productive Time in Challenging Wells. In *SPE Oil and Gas India Conference and Exhibition*, 20-22 January, Mumbai, India. Paper SPE-129030-MS.

Gazaniol, D., Forsans, T., Boisson, M. J. F., & Piau, J. M. (1995). Wellbore failure mechanisms in shales: prediction and prevention. *Journal of Petroleum Technology*, *47*(7), 589–595.

Gercek, H. (1997). An elastic solution for stresses around tunnels with conventional shapes. *International Journal of Rock Mechanics and Mining Sciences & Geomechanics Abstracts*, *34*(3–4), 708.

Gercek, H. (1991). Stresses around tunnels with arched roof. *7th ISRM Congress*, 1297–1299. International Society for Rock Mechanics

Germanovich, L. N., & Dyskin, A. V. (2000). Fracture mechanisms and instability of openings in compression. *International Journal of Rock Mechanics and Mining Sciences*, *37*(1–2), 263–284.

Gerolymatou, E. (2019). A novel tool for simulating brittle borehole breakouts. *Computers and Geotechnics*, 107, 80-88.

Gerolymatou, E., & Petalas, A. (2020). In Situ Stress Assessment Based on Width and Depth of Brittle Borehole Breakouts. In *Recent Developments of Soil Mechanics and Geotechnics in Theory and Practice* (pp. 297-319). Springer, Cham.

Gough, D. I., & Bell, J. S. (1982). Stress orientations from borehole wall fractures with examples from Colorado, east Texas, and northern Canada. *Canadian Journal of Earth Sciences*, *19*(7), 1358–1370.

Greenspan, M. (1944). Effect of a Small Hole on the Stresses in a Uniformly Loaded Plate. *Quarterly of Applied Mathematics*, *2*(1), 60–71.

Gupta, D., & Zaman, M. (1999). Stability of boreholes in a geologic medium including the effects of anisotropy. *Applied Mathematics and Mechanics (English Edition)*, *20*(8), 837–866.

Haimson, B. (2007). Micromechanisms of borehole instability leading to breakouts in rocks. *International Journal of Rock Mechanics and Mining Sciences*, *44*(2), 157–173.

Hamid, O., Khan, K., Rahim, Z., Omair, A., Ahmed, S., & Ahmed, M. (2016). Reducing Drilling Operational Risk and Non-Productive Time Using Real-Time Geomechanics Surveillance. In *International Petroleum Technology Conference*, 14-16 November 2016, Bangkok. Paper IPTC-18793.

Herrick, C. G., & Haimson, B. C. (1994). Modeling of episodic failure leading to borehole breakouts in Alabama limestone. Paper presented at the 1st North American Rock Mechanics Symposium, Austin, Texas. Paper ARMA-1994-0217.

Hiramatsu, Y., & Oka, Y. (1968). Determination of the stress in rock unaffected by boreholes or drifts, from measured strains or deformations. *International Journal of Rock Mechanics and Mining Sciences*, *5*(4), 337–353.

Hoyer, C. (2009). Are we really listening? *Journal of Petroleum Technology*, *61*(7), 18–20.

Huber, K., Fuchs, K., Palmer, J., Roth, F., Khakhaev, B. N., Van-Kin, L. E., Pevzner, L. A., Hickman, S., Moos, D., Zoback, M. D., & Schmitt, D. (1997). Analysis of borehole televiewer measurements in the Vorotilov drillhole, Russia - First results. *Tectonophysics*, *275*(1–3), 261–272.

Jaeger, J. C. (1960). Shear Failure of Anistropic Rocks. *Geological Magazine*, *97*(1), 65–72.

Jaeger, J. C., Cook, N. G. W., & Zimmerman, R. W. (2007). *Fundamentals of rock mechanics*. 4th ed. 2007, Wiley-Blackwell, Oxford.

Kanfar, M. F., Chen, Z., & Rahman, S. S. (2015a). Effect of material anisotropy on time-dependent wellbore stability. *International Journal of Rock Mechanics and Mining Sciences*, *78*, 36–45.

Kanfar, M. F., Chen, Z., & Rahman, S. S. (2015b). Risk-controlled wellbore stability analysis in anisotropic formations. *Journal of Petroleum Science and Engineering*, *134*, 214–222.

Kantorovich, L. V, & Krylov, V. I. (1958). *Approximate Methods of Higher Analysis*. Noordhoff, Groningen.

Khaksar, A., Taylor, P. G., Fang, Z., Kayes, T., Salazar, A., & Rahman, K. (2009). Rock strength from core and logs: Where we stand and ways to go. In *Society of Petroleum Engineers - EUROPEC/EAGE Conference and Exhibition 2009*. Paper SPE 121972-MS.

Kim, H., Xie, L., Min, KB., Bae, S., & Stephansson, O (2017). Integrated In Situ Stress Estimation by Hydraulic Fracturing, Borehole Observations and Numerical Analysis at the EXP-1 Borehole in Pohang, Korea. *Rock Mech Rock Eng,* 50, 3141–3155.

Kirsch, E. G. (1898). Die Theorie der Elastizität und die Bedürfnisse der Festigkeitslehre. *Zeitschrift Des Vereines Deutscher Ingenieure*, *42*, 797–807.

Kolosov, G. V. (1909). *On the Application of the Theory of Functions of a Complex Variable to a Plane Problem in the Mathematical Theory of Elasticity*. PhD. Diss., Dorpat University (in Russian), 1909.

Lee, H., Ong, S. H., Azeemuddin, M., & Goodman, H. (2012). A wellbore stability model for formations with anisotropic rock strengths. *Journal of Petroleum Science and Engineering*, *96–97*, 109–119.

Lee, M., & Haimson, B. C. (1993). Laboratory study of borehole breakouts in Lac du Bonnet granite: a case of extensile failure mechanism. *International Journal of Rock Mechanics and Mining Sciences And*, *30*(7), 1039–1045.

Lekhnitskii, S. G. (1963). *Theory of Elasticity of an Anistropic Elastic Body*. Holden-Day, San Francisco.

Lekhnitskii, S. G. (1968). *Anisotropic Plates*. Gordon and Breach, New York.

Li, Q., Yousefzadeh, A., & Aguilera, R. (2015). Anisotropic wellbore stability model for naturally fractured and foliated formations with multi-weakness plane failure. *Society of Petroleum Engineers - SPE/CSUR Unconventional Resources Conference*. Paper SPE-175896.

Lu, A., Zhang, N., Zhang, X., Lu, D., & Li, W. (2015). Analytic Method of Stress Analysis for an Orthotropic Rock Mass with an Arbitrary-Shaped Tunnel. *International Journal of Geomechanics*, 15(4): 04014068.

Lu, Y. H., Chen, M., Jin, Y., Chen, G., Lin, B. T., Liang, C., & Ji, J. X. (2015). Anisotropic wellbore stability model for transversely isotropic formation and its application in drilling through shale formation. In *Society of Petroleum Engineers - SPE Asia Pacific Unconventional Resources Conference and Exhibition*. Paper SPE-176922.

Mastin, L. (1988). Effect of borehole deviation on breakout orientations. *Journal of Geophysical Research*, *93*(B8), 9187–9195.

Maugis, D. (1992). Stresses and displacements around cracks and elliptical cavities: Exact solutions. *Engineering Fracture Mechanics*, 43(2), 217–255.

Maxwell, S. (2014). Microseismic Imaging of Hydraulic Fracturing. In *Microseismic Imaging of Hydraulic Fracturing*.

McLellan, P. J. (1996). Assessing the risk of wellbore instability in horizontal and inclined wells. *Journal of Canadian Petroleum Technology*, *35*(5), 21–32.

McLellan, P. J., & Cormier, K. (1996). Borehole instability in fissile, dipping shales, Northeastern British Columbia. In *SPE Proceedings - Gas Technology Symposium* (pp. 535–547). Paper SPE 35634-ms.

Melentiev, P. V. (1937). *Several New Methods and Devices for Approximate Computations*. Moscow-Leningrad.

Mitchell, L. H. (1966). Stress-Concentration Factors at a Doubly-Symmetric Hole. *Aeronautical Quarterly*, *17*(2), 177–186.

Moazzeni, A., Nabaei, M., Shahbazi, K., & Shadravan, A. (2010). Mechanical earth modeling improves drilling efficiency and reduces Non-Productive Time (NPT). In *SPE Deep Gas Conference and Exhibition*, 24-26 January, 2010, Bahrain. Paper SPE 131718.

Mogi, K. (1967). Effect of the intermediate principal stress on rock failure. *Journal of Geophysical Research*, *72*(20), 5117–5131.

Moore, J. C., Chang, C., Mcneill, L., Thu, M. K., Yamada, Y., & Huftile, G. (2012). Growth of borehole breakouts with time after drilling: Implications for state of stress, NanTroSEIZE transect, SW Japan. *Geochemistry, Geophysics, Geosystems*, *12*(4).

Muskhelishvili, N. I. (1953). *Some Basic Problems of the Mathematical Theory of Elasticity*. Nordhoff, Groningen.

Naidu, N. A., Hinaai, Q., Ismaili, I., Smit, J., Youssef, H., Hendra, S., & Kumar, R. (2016). Successful drilling to completion of a highly stressed depleted tight gas sandstone reservoir based on geomechanical study. In *Society of Petroleum Engineers - Abu Dhabi International Petroleum Exhibition and Conference 2016*. Paper SPE 183380.

Narayanasamy, R., Barr, D., & Milne, A. (2010). Wellbore-instability predictions within the cretaceous mudstones, Clair field, West of shetlands. In *SPE Offshore Europe Oil and Gas Conference and Exhibition*. Paper SPE-124464-MS.

Okland, D., & Cook, J. M. (1998). Bedding-related borehole instability in high-angle wells. In *SPE/ISRM Rock Mechanics in Petroleum Engineering Conference, 8-10 July 1998*. Trondheim, Norway. Paper SPE/ISRM 47285.

Ong, S. H., Power, W. L., Sitio, A., & Tanjung, E. (2015). Geomechanics improves drilling operations and reduces non-productive times (NPT) in Kilo Field, Offshore Northwest Java. In *Society of Petroleum Engineers - SPE/IATMI Asia Pacific Oil and Gas Conference and Exhibition, APOGCE 2015*. Paper SPE 176445.

Ong, S. H., & Roegiers, J. C. (1993a). Horizontal wellbore collapse in an anisotropic formation. *Production Operations Symposium*, 877–889.

Ong, S. H., & Roegiers, J. C. (1993b). Influence of anisotropies in borehole stability. *International Journal of Rock Mechanics and Mining Sciences And*, *30*(7), 1069–1075.

Ong, S. H., & Roegiers, J. C. (1995). Fracture initiation from inclined wellbores in anisotropic formations. *Journal of Petroleum Technology*, 48(7), 612-619.

Plumb, R. A. (1990). Fracture patterns associated with incipient wellbore breakouts. In *ISRM International Symposium*, Pau, France. Paper ISRM-1989-098.

Plumb, R. A., & Hickman, S. H. (1985). Stress-Induced Borehole Elongation: a Comparison Between the Four-Arm Dipmeter and the Borehole Televiewer in the Auburn Geothermal Well. *Journal of Geophysical Research*, *90*(B7), 5513–5521.

Prensky, S. E. (1999). Advances in borehole imaging technology and applications. *Geological Society Special Publication*, *159*(1), 1–43.

Prioul, R., Frydman, M., & Caniggia, J. (2016). Estimating anisotropic mechanical properties and stress based on measurements on cuttings for completion quality: Methodology and case study in Vaca Muerta. In *Society of Petroleum Engineers - SPE Argentina Exploration and Production of Unconventional Resources Symposium*. Paper SPE 180969-ms.

Read, R. S., Martin, C. D., & Dzik, E. J. (1995). Asymmetric borehole breakouts at the URL. In *35th U.S. Symposium on Rock Mechanics, USRMS 1995*. Paper ARMA-95-0879.

Sadd, M. H. (2014). *Elasticity: Theory, Applications, and Numerics*. Elsevier Science.

Sahara, D. P., Schoenball, M., Gerolymatou, E., & Kohl, T. (2017). Analysis of borehole breakout development using continuum damage mechanics. *International Journal of Rock Mechanics and Mining Sciences*, *97*, 134–143.

Savin, G. N. (1961). *Stress concentration around holes*. Pergamon Press.

Schmitt, D. R., Currie, C. A., & Zhang, L. (2012). Crustal stress determination from boreholes and rock cores: Fundamental principles. *Tectonophysics*, *580*, 1–26.

Setiawan, N. B., & Zimmerman, R. W. (2020). A Unified Methodology for Computing the Stresses around an Arbitrarily-Shaped Hole in Isotropic or Anisotropic Materials. *International Journal of Solids and Structures*, *199*, 131–143.

Shi, X., Yang, X., Meng, Y., & Li, G. (2016). An Anisotropic Strength Model for Layered Rocks Considering Planes of Weakness. *Rock Mechanics and Rock Engineering*, *49*(9), 3783–3792.

Simha, K. R. Y., & Mohapatra, S. S. (1998). Stress concentration around irregular holes using complex variable method. *Sadhana - Academy Proceedings in Engineering Sciences*, *23*(4), 393–412.

Sobey, A. J. (1964). The estimation of stresses around unreinforced holes in infinite elastic sheets. *Aeronautical Research Council Reports and Memoranda, Ministry of Aviation, HM Stationery Office*.

Suárez-Rivera, R., Green, S. J., McLennan, J., & Bai, M. (2006). Effect of layered heterogeneity on fracture initiation in tight gas shales. In *Proceedings - SPE Annual Technical Conference and Exhibition*. Paper SPE-103327-MS.

Tan, C. P., Teng, G. E., Kamaruddin, N. M. F., Musa, I. H., Maung, M. M. T., Mohamad-Hussein, A., Ni, Q., & Minton, J. (2019). Novel wellbore failure geometry evolution and stabilization model for shale formations. In *53rd U.S. Rock Mechanics/Geomechanics Symposium* (p. 10). Paper ARMA-2019-0389.

Tien, Y. M., & Kuo, M. C. (2001). A failure criterion for transversely isotropic rocks. *International Journal of Rock Mechanics and Mining Sciences*, *38*(3), 399–412.

Ukadgaonker, V. G., & Rao, D. K. N. (2000). A general solution for stresses around holes in symmetric laminates under inplane loading. *Composite Structures*, *49*(3), 339–354.

Valley, B., Azzola, J., Schmittbuhl, J., & Genter, A. (2018). Temporal borehole breakout evolution and its impact on stress estimation. In *52nd U.S. Rock Mechanics/Geomechanics Symposium* (p. 8). Paper ARMA-2018-806.

van Oort, E., Hale, A. H., Mody, F. K., & Roy, S. (1996). Transport in shales and the design of improved water-based shale drilling fluids. *SPE Drilling and Completion*, *11*(3), 137–146.

van Cauwelaert, F. (1977). Coefficients of deformation of an anisotropic body. *Journal of the Engineering Mechanics Division*, 103(5), 823-835.

Walsh, J. J., Sinha, B. K., Plona, T. J., Miller, D. E., & Ammerman, M. (2008). Derivation of anisotropy parameters in a shale using borehole sonic data. In *The 42nd U.S. Rock Mechanics Symposium (USRMS)*. Paper SEG-2007-0323.

Wang, Z. (2002). Seismic anisotropy in sedimentary rocks, part 2: Laboratory data. *Geophysics*, *67*(5), 1423–1440.

White, A. J., Traugott, M. O., & Swarbrick, R. E. (2002). The use of leak-off tests as means of predicting minimum *in situ* stress. *Petroleum Geoscience*, *8*(2), 189–193.

Willson, S. M., Edwards, S. T., Crook, A., Bere, A., Moos, D., Peska, P., & Last, N. (2007). Assuring stability in extended-reach wells - Analyses, practices, and mitigations. In *SPE/IADC Drilling Conference, Proceedings* (Vol. 1, pp. 358–371). Paper SPE 105405-ms.

Wu, B., & Tan, C. P. (2010). Effect of shale bedding plane failure on wellbore stability - Example from analyzing stuck-pipe wells. In *44th US Rock Mechanics Symposium - 5th US/Canada Rock Mechanics Symposium*. Paper ARMA-10-350.

Xi, G. F., Labbassen, N., Al Badi, B. S., Lecoq, T. F., Al-Husseiny Afifi, H., Al-Marzooqi, A. M. M., El Mais, N., Mavromatidis, A., Ofield, W., & Rodriguez, J. (2015). Mud weight optimization to reduce non-productive-time while drilling through shale/carbonate sequence of UAE: A Case Study. In *Society of Petroleum Engineers - Abu Dhabi International Petroleum Exhibition and Conference, ADIPEC 2015*. Paper SPE 177851.

Yan, G., Karpfinger, F., Prioul, R., Tang, H., Jiang, Y., & Liu, C. (2014). Anisotropic wellbore stability model and its application for drilling through challenging shale gas wells. In *International Petroleum Technology Conference 2014*. Paper IPTC-18143-MS.

Zadvornov, D. A., Grachev, O. V., Maximov, D. A., Pekshev, D. V., Korelskiy, E. P., & Pavlov, V. A. (2016). Innovative geomechanical approach lead to successful drilling of the first highly deviated well at the kruzenshternskoe field. In *Society of Petroleum Engineers - SPE Russian Petroleum Technology Conference and Exhibition*. Paper SPE-182032-MS.

Zhang, H., Yin, S., & Aadnoy, B. S. (2018). Finite-element modeling of borehole breakouts for *in situ* stress determination. *International Journal of Geomechanics*, *18*(12), 4018174.

Zhang, H., Yin, S., & Aadnoy, B. S. (2019). Numerical investigation of the impacts of borehole breakouts on breakdown pressure. *Energies*, *12*(5), 888.

Zhang, J. (2013). Borehole stability analysis accounting for anisotropies in drilling to weak bedding planes. *International Journal of Rock Mechanics and Mining Sciences*, *60*, 160–170.

Zheng, Z., Cook, N. G. W., & Myer, L. R. (1988). Borehole breakout and stress measurements. In *29th U.S. Symposium on Rock Mechanics, USRMS 1988*. Paper ARMA-88-0471.

Zheng, Z., Kemeny, J., & Cook, N. G. W. (1989). Analysis of borehole breakouts. *Journal of Geophysical Research*, *94*(B6), 7171–7182.

Zoback, M. D., Barton, C. A., Brudy, M., Castillo, D. A., Finkbeiner, T., Grollimund, B. R., Moos, D. B., Peska, P., Ward, C. D., & Wiprut, D. J. (2003). Determination of stress orientation and magnitude in deep wells. *International Journal of Rock Mechanics and Mining Sciences*, *40*(7–8), 1049–1076.

Zoback, M. D., Moos, D., Mastin, L., & Anderson, R. N. (1985). Wellbore breakouts and *in situ* stress. *Journal of Geophysical Research*, *90*(B7), 5523–5530.